# ACOUSTIC RESONATORS FOR THE REDUCTION OF SOUND RADIATION AND TRANSMISSION

Marieke Hannink

De promotiecommissie is als volgt samengesteld:

| | |
|---|---|
| *Voorzitter en secretaris*: | |
| Prof.dr. F. Eising | Universiteit Twente |
| *Promotor*: | |
| Prof.dr.ir. A. de Boer | Universiteit Twente |
| *Assistent-promotor*: | |
| Dr.ir. Y.H. Wijnant | Universiteit Twente |
| *Leden*: | |
| Prof.dr.ir. A. Hirschberg | Technische Universiteit Eindhoven/ Universiteit Twente |
| Prof.dr.ir. H.W.M. Hoeijmakers | Universiteit Twente |
| Prof.dr. A.C. Nilsson | Kungliga Tekniska Högskolan, Stockholm |
| Prof.dr.ir. N.B. Roozen | Technische Universiteit Eindhoven/ Philips Applied Technologies |
| Ir. R.M.E.J. Spiering | Universiteit Twente |

This research was performed in the framework of the EU project FACE, contract number G4RD-CT2002-00764.

Acoustic resonators for the reduction of sound radiation and transmission
Hannink, Marieke Henriëtte Cathrien
PhD thesis, University of Twente, Enschede, The Netherlands
May 2007

ISBN 978-90-365-2490-2
Subject headings: acoustics, vibrations, resonators


Printed by Ponsen & Looijen b.v., Wageningen, The Netherlands

*Cover: photograph of a panel with tube resonators, taken by R. Loendersloot.*

# ACOUSTIC RESONATORS FOR THE REDUCTION OF SOUND RADIATION AND TRANSMISSION

PROEFSCHRIFT

ter verkrijging van
de graad van doctor aan de Universiteit Twente,
op gezag van de rector magnificus,
prof.dr. W.H.M. Zijm,
volgens besluit van het College voor Promoties
in het openbaar te verdedigen
op woensdag 16 mei 2007 om 15.00 uur

door

Marieke Henriëtte Cathrien Hannink

geboren op 2 juli 1978

te Zwolle

Dit proefschrift is goedgekeurd door de promotor

Prof.dr.ir. A. de Boer

en de assistent-promotor

Dr.ir. Y.H. Wijnant

# Summary

Noise is a frequently encountered problem in modern society. One of the environments where the presence of noise causes a deterioration in people's comfort is in aircraft cabins. For modern aircraft flying at cruise conditions, the main sound source is the turbulent boundary layer around the fuselage. Especially in the mid and high frequency range (500-2000 Hz), this source significantly contributes to the sound levels in the aircraft cabin. Passive noise reduction methods can provide a suitable solution to many noise problems in this frequency range. In the present study, a new passive noise reduction method is presented, known as tube resonators. Tube resonators are well-known for their application for sound absorption. However, in the present work, this type of resonator is applied for the reduction of sound radiation and sound transmission. The aim of this work is to investigate the applicability of this new method and to develop and validate efficient models for the prediction of sound radiation by and sound transmission through panels with tube resonators. For a proper understanding of the influences of the different phenomena, different models and experiments are presented in order of increasing complexity.

First, sound radiation and normal incidence sound transmission are studied using one-dimensional analytical models. The analyses are based on the assumption that the panels are rigid and infinitely large. For narrow tube resonators, viscothermal effects also play a role. These effects are included in the models as well. Analysis results predict that, by the application of tube resonators, large reductions of the radiated and transmitted sound power can be obtained. The centre frequency of the range in which the sound is reduced is the frequency for which a half, or odd multiples of a half, of the acoustic wavelength is equal to the resonator length. The porosity of the panel determines the frequencies for which maximum sound reduction is obtained in this range. Validation of the model for sound radiation by means of experiments in an impedance tube, shows a good agreement between model and measurements.

To study the effect of scattering by the resonator openings, a two-dimen-

sional semi-analytical model is presented, which is based on similar assumptions as the one-dimensional analytical model. It is shown that scattering causes some inlet effects, but hardly influences the radiation and transmission of sound.

Subsequently, a two-dimensional finite element model is introduced to investigate the transmission of sound through a panel with resonators mounted between two rooms. For stiff panels, the trends of the transmission loss curves are similar to those predicted by the one-dimensional analytical model. For flexible panels, it is shown that mainly the flexibility of the resonators has a large effect on the sound transmission loss.

To be able to model more complex and realistic setups, three three-dimensional numerical models are presented. To reduce computation time, all models are reduced in some way. The reductions both concern the structural part of the model and the acousto-elastic interaction. First, the Rayleigh integral method is used to calculate the sound radiated by a panel with resonators, placed in an infinite baffle. It is shown that for a rigid panel, the boundaries of the panel do not influence the radiated sound power as long as its dimensions are larger than the acoustic wavelength. Furthermore, results for a baffled, flexible panel are presented.

Next, a reduced finite element model is introduced. In this model the panel is flexible; however, in the formulation of the acousto-elastic interaction, the resonators are still assumed to be rigid. A new interface element is formulated, which both includes the acousto-elastic interaction and the acoustic behaviour of the resonators. Structural resonances of the panel appear to have a large negative effect on the sound transmission loss. However, the general trend of the transmission loss curve remains the same as predicted by the one-dimensional analytical model.

To fully examine the influence of the flexibility of the resonators, finally, a fully coupled finite element model of a small part of the panel with one resonator is introduced. It is shown that the flexibility of the structure has a large influence on the sound transmission loss.

To verify whether the assumptions and simplifications that were made in the models are valid, sound transmission loss measurements were performed on two resonator panels of different configurations: a panel with tubes and a sandwich panel perforated on one side. Both measurements show that large increases in sound transmission loss can be obtained by the application of tube resonators. However, the increases are not as large as predicted by the models. To improve the predictions of sound transmission through panels with tube resonators, more detailed, large-scale models are required.

# Samenvatting

Geluidsoverlast is een veelvuldig voorkomend probleem in de hedendaagse samenleving. Zo wordt het comfort in een vliegtuigcabine mede bepaald door de mate van geluidsoverlast. Voor moderne vliegtuigen vliegend onder kruisvluchtcondities is de turbulente grenslaag rondom de romp van het vliegtuig de voornaamste geluidsbron. Vooral in het midden- en hoogfrequente gebied (500-2000 Hz) draagt deze bron aanzienlijk bij aan het geluidsniveau in de vliegtuigcabine. Een geschikte oplossing voor veel geluidsproblemen in dit frequentiegebied is de toepassing van passieve geluidsreductiemethoden. In dit proefschrift wordt een nieuwe passieve geluidsreductiemethode gepresenteerd, de zogenaamde buisjesresonatoren. Buisjesresonatoren zijn bekend van hun toepassing voor geluidsabsorptie. Echter, in het huidige werk wordt dit soort resonatoren toegepast voor de reductie van geluidsafstraling en geluidstransmissie. Het doel van dit werk is het onderzoeken van de toepasbaarheid van deze nieuwe methode en het ontwikkelen en valideren van efficiënte modellen voor de voorspelling van geluidsafstraling en geluidstransmissie door panelen met buisjesresonatoren. Voor een goed begrip van de invloeden van de verschillende fenomenen, worden er verschillende modellen en experimenten gepresenteerd, in volgorde van toenemende complexiteit.

Allereerst worden de transmissie van loodrecht invallend geluid en geluidsafstraling bestudeerd met behulp van ééndimensionale modellen. De analyses zijn gebaseerd op de aanname dat de panelen star en oneindig groot zijn. Bij buisjesresonatoren met een kleine diameter spelen ook viscothermische effecten een rol. Deze effecten zijn eveneens meegenomen in de modellen. De resultaten van de analyses voorspellen dat door toepassing van buisjesresonatoren grote reducties van het afgestraalde en doorgelaten geluidsvermogen kunnen worden verkregen. De centerfrequentie van het frequentiegebied waarin het geluid wordt gereduceerd is de frequentie waarvoor een halve, of oneven veelvouden van een halve, akoestische golflengte gelijk is aan de lengte van de resonator. De porositeit van het paneel bepaalt de frequenties waarvoor maximale geluidsreductie wordt verkregen in dit gebied. Validatie van het model voor

geluidsafstraling door middel van experimenten in een impedantiebuis laat een goede overeenkomst zien tussen model en metingen.

Om het effect van verstrooiing door de openingen van de resonatoren te bestuderen, wordt een tweedimensionaal model gepresenteerd dat gebaseerd is op soortgelijke aannamen als het ééndimensionale model. Er wordt aangetoond dat verstrooiing inlaateffecten veroorzaakt, maar nauwelijks invloed heeft op de afstraling en transmissie van geluid.

Vervolgens wordt een tweedimensionaal eindig elementenmodel geïntroduceerd, om de transmissie van geluid door een paneel met resonatoren te onderzoeken dat is opgehangen tussen twee kamers. Voor stijve panelen zijn de trends van transmissieverliescurven ongeveer gelijk aan de trends voorspeld door het ééndimensionale analytische model. Voor flexibele panelen wordt aangetoond dat vooral de flexibiliteit van de resonatoren een groot effect heeft op het geluidstransmissieverlies.

Om complexere en realistischere opstellingen te kunnen modelleren, worden er drie driedimensionale numerieke modellen gepresenteerd. Om de rekentijd te verminderen, zijn alle modellen op een bepaalde manier gereduceerd. De reducties betreffen zowel het structurele deel van het model als de akoestoelastische interactie. Allereerst wordt de Rayleigh integraalmethode gebruikt om het geluid te berekenen dat wordt afgestraald door een paneel met resonatoren omringd door een oneindig groot, akoestisch hard oppervlak. Er wordt aangetoond dat, als de afmetingen van het paneel groter zijn dan de akoestische golflengte, de randen van een star paneel geen invloed hebben op het afgestraalde geluidsvermogen. Verder worden er ook resultaten gepresenteerd voor een flexibel paneel omringd door een oneindig groot, akoestisch hard oppervlak.

Vervolgens wordt er een gereduceerd eindig elementenmodel geïntroduceerd. In dit model is het paneel flexibel, maar in de formulering van de akoesto-elastische interactie worden de resonatoren nog steeds als star beschouwd. Een nieuw koppelelement wordt geformuleerd dat zowel de akoestoelastische interactie als het akoestische gedrag van de resonatoren bevat. Structurele resonanties van het paneel blijken een groot negatief effect te hebben op het geluidstransmissieverlies. Echter, de algemene trend van het transmissieverlies blijft gelijk aan die voorspeld door het ééndimensionale analytische model.

Om de invloed van de flexibiliteit van de resonatoren volledig te onderzoeken, wordt er tenslotte een volledig gekoppeld eindig elementenmodel van een klein gedeelte van het paneel met één resonator geïntroduceerd. Er wordt wederom aangetoond dat de flexibiliteit van de structuur een grote invloed

heeft op het geluidstransmissieverlies.

Om te controleren of de aannames en vereenvoudigingen die in de modellen zijn gemaakt, geldig zijn, zijn geluidstransmissieverliesmetingen uitgevoerd op twee resonatorpanelen van verschillende configuraties: een paneel met buisjes en een sandwichpaneel dat aan één kant geperforeerd is. Beide metingen laten zien dat door de toepassing van buisjesresonatoren grote toenames van het geluidstransmissieverlies kunnen worden verkregen. De gemeten toenames zijn echter niet zo groot als voorspeld door de modellen. Om de voorspellingen van geluidstransmissieverlies door panelen met buisjesresonatoren te verbeteren, zijn gedetailleerdere, grootschalige modellen vereist.

# Contents

# Chapter 1

# Introduction

## 1.1 Background

### Sound and noise

Sound is all around. Sometimes it is experienced as pleasant, sometimes as unpleasant. Unwanted sound is generally referred to as noise. Noise encountered in daily life can, for example, be caused by domestic appliances such as vacuum cleaners and washing machines, vehicles such as cars and aeroplanes, or screaming neighbours.

### Noise in aircraft cabins

Noise in aircraft cabins is mainly induced by the power plant (propeller and engine) and the turbulent airflow over the fuselage. For modern aircraft flying at cruise conditions, the main sound source is the turbulent boundary layer [32, 56]. Pressure fluctuations in the boundary layer excite the fuselage, which causes vibrations in the structure. The vibrations of the structure are subsequently transmitted to the air inside the aircraft cabin, leading to pressure perturbations that are usually experienced as sound. Sources of unwanted sound like this may cause a lot of discomfort to the passengers. To enhance the environmental comfort in aircraft cabins, a European project called FACE (Friendly Aircraft Cabin Environment) was initiated. Besides the reduction of aircraft interior noise, attention was also paid to issues like air quality control and the utilisation of multimedia devices. Various European aircraft companies, research institutes and universities were involved. The present work, concentrating on noise reduction, was also carried out in the framework of FACE.

### Noise reduction

Common methods of passive noise reduction are the use of porous materials such as glass wool or foam [6, 15], double wall panels with thin air layers [1], or the application of acoustic resonators. In the present work, the acoustic behaviour of one type of acoustic resonator, so-called tube resonators, is investigated. To gain some insight into the working principle of the resonators, a simple panel geometry is considered. A schematic representation of such a panel with tube resonators is shown in Figure 1.1. The tubes are closed at one end and open at the side where they are attached to the panel. Panels like this could, for example, be used as trim panels in aircraft. In the present study, the focus is mainly on the behaviour of the resonators with regard to sound radiation and sound transmission. The emphasis in this thesis is on the development and validation of analysis tools and the physical understanding of phenomena that play a role. Analyses found in the literature, state that noise generated by turbulent boundary layers significantly contributes to the mid and high frequency range of sound power levels in aircraft cabins [4, 24, 56]. Measurements by Bhat and Wilby [4] show that the highest sound power levels are found in the frequency range of 500-2000 Hz. This frequency range is also the frequency range of interest in this work.

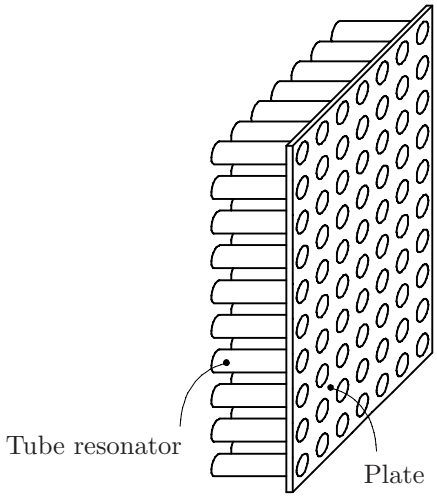


**Figure 1.1**: Part of a panel with tube resonators.

## 1.2 Sound transmission

**Reduction of sound transmission versus sound absorption**

Tube resonators are well known for their absorption applications [23]. In the case of sound absorption, sound is dissipated by mechanisms such as viscous shear and thermal conductivity. The sound that is reflected from a sound absorbing wall or panel is therefore smaller in magnitude than the incident sound, which means that the sound level in a room can be reduced (see Figure 1.2(a)).

When considering sound absorption, the panel or wall is generally assumed to be rigid and non-vibrating. Besides the reduction of the sound reflected by a non-vibrating panel, resonators also enable the reduction of sound radiated by a vibrating panel. In this thesis, the possibilities for the application of tube resonators for the latter purpose are investigated.

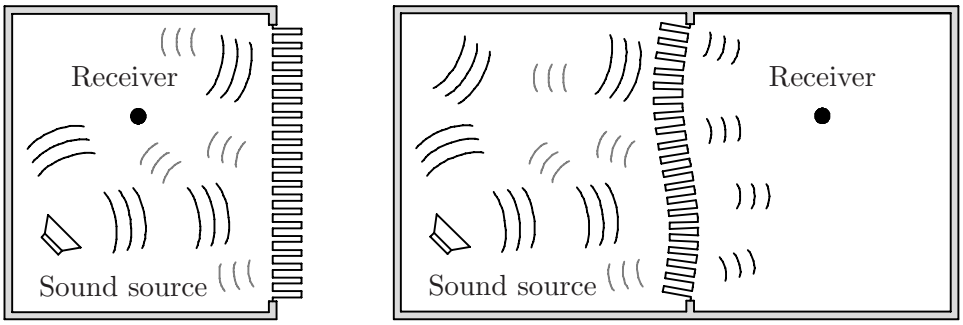


(a) Sound absorption. (b) Sound transmission.

**Figure 1.2**: Reduction of sound transmission versus sound absorption.

When a structure is vibrating, it excites the surrounding air, which causes radiation of sound. The structure can either be excited by a structural force or an acoustic sound field. To better understand the important aspects of sound insulation by means of tube resonators, most analyses in this work start by considering the general case of sound radiation. This means that the radiated sound is calculated for a panel which is assumed to vibrate with a certain given velocity distribution. Since the origin of these vibrations can either be structural or acoustic, the insights that are gained can be used for the reduction of both types of excitation. By subsequently applying acoustic excitation, the models for sound radiation are extended to models for sound transmission (see Figure 1.2(b)).

### Basic principles of sound transmission

The conventional measure for sound insulation of panels is the sound transmission loss, which is the ratio of the incident and transmitted sound powers in logarithmic form. In Figure 1.3 a typical sound transmission loss curve of an isotropic panel without resonators is shown. In this figure, the following regions can be distinguished:

- Below the first eigenfrequency $f_e$ of the system, the sound transmission loss is primarily determined by the stiffness and decreases with frequency at 6 dB per doubling of frequency.

- At the first eigenfrequency $f_e$, the transmission of sound is large and, consequently, the transmission loss passes through a minimum. The depth of the dip is mainly determined by the damping in the system [6].

- Above the first eigenfrequency $f_e$, the sound transmission loss is primarily determined by the mass per unit area of the panel. In this frequency range, the sound transmission loss is described by the so-called mass law, which implies that transmission loss increases with 6 dB per doubling of frequency and 6 dB per doubling of mass per unit area. The sound transmission loss also depends on the angle of the incident sound wave. In the mass law region, the transmission loss decreases with increasing angle of incidence.

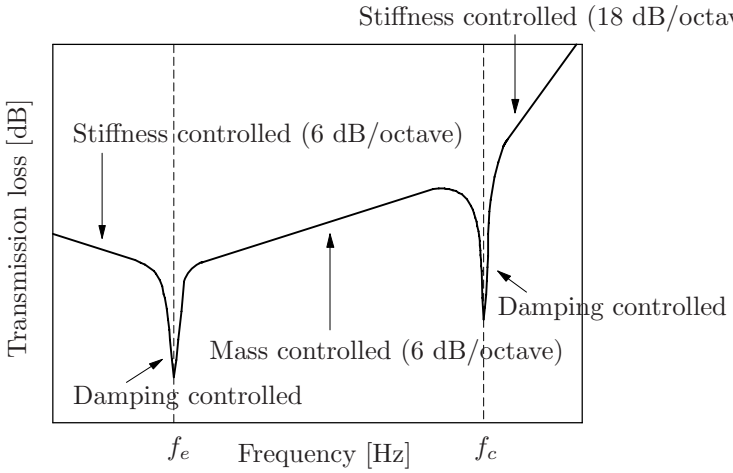


**Figure 1.3**: Typical sound transmission loss curve of an isotropic panel without resonators (frequency on logarithmic scale).

- At higher frequencies, above the so-called critical frequency $f_c$, coincidence occurs. Coincidence occurs if the bending wavelength of the panel is equal to the projected wavelength of the obliquely incident sound wave (see also Section 5.3.3). In this case, there is a very good coupling of energy from the incident wave to the bending wave, which makes the panel radiate sound efficiently to the other side [34]. The panel acts as if it is transparent to incident sound waves and the sound waves are freely transmitted [5]. This causes a dip in the transmission loss curve. The depth of the coincidence dip depends on the damping of the panel.

  The extent of the mass law region depends on the ratio of mass and stiffness of the panel. Generally, the mass law is only accurate up to half the critical frequency [6].

- At very high frequencies, the sound transmission loss increases again, being stiffness controlled. The increase in transmission loss is in the order of 18 dB per doubling of frequency [20].

In the present work, the focus is primarily on the frequency range in which panels behave according to the mass law. It is obvious that the sound insulating properties of a panel in this range can be improved by increasing the mass of the panel. However, in practice it is often desired to design structures of minimum weight. Generally, the challenge is therefore to reduce the transmission of sound without increasing the mass of the construction. To assess the performance of the tube resonators, in this thesis, a comparison is accordingly made with panels of the same mass without resonators.

## 1.3 Noise reduction with tube resonators

### Tube resonators for sound absorption

The working principle of tube resonators for sound absorption is based on the resonance of air inside the resonators. Inside the resonators, resonance occurs when a quarter, and odd multiples of a quarter, of the acoustic wavelength[1] are equal to the resonator length. At these frequencies, maximum sound absorption takes place. Tube resonators are therefore also called quarter-wave resonators. Another important condition, for more broadband sound absorption, is the presence of viscothermal effects. These effects are mainly determined by the frequency and the radius of the resonators. An example of a

[1] The acoustic wavelength $\lambda$ is defined as $\lambda = c_0/f$, where $c_0$ is the speed of sound and $f$ is the frequency.

typical sound absorption curve of a wall or panel with quarter-wave resonators is shown in Figure 1.4(a)[2]. The absorption characteristics of such a panel can be optimised by tuning three parameters. As mentioned before, the resonator length determines the main frequencies at which sound is absorbed, and the resonator radius and the porosity[3] of the panel determine the height and the width of the absorption peaks. One of the disadvantages of quarter-wave resonators is that, generally, sound is only absorbed in a small frequency band around the resonance frequencies of the air inside the resonators. For broadband sound absorption, coupled tubes [18], resonators with different lengths and radii [31, 54], or very narrow tubes and high porosities can be used.

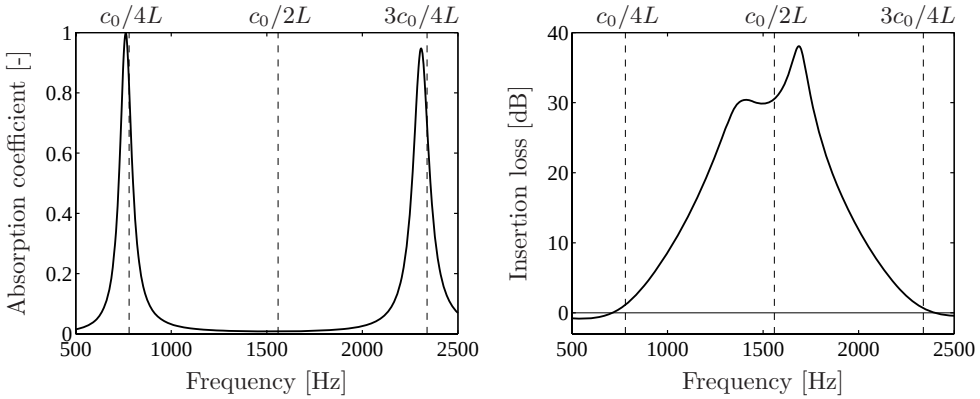


(a) Absorption coefficient ($\Omega = 0.04$). (b) Insertion loss ($\Omega = 0.5$).

**Figure 1.4**: Sound absorption and sound radiation characteristics of a panel with resonators of length $L = 0.11$ m and radius $R = 2.5 \cdot 10^{-3}$ m.

### Tube resonators for the reduction of sound radiation

The working principle of tube resonators for the reduction of sound radiation is different than for sound absorption. In the case of sound radiation, the reduction is only partly achieved by resonance of the air inside the resonators and viscothermal effects play a much less important role. The centre frequency of the frequency range in which the sound is reduced is now the frequency for which a half, or odd multiples of a half, of the acoustic wavelength is equal to

[2]The calculations were made using a one-dimensional analytical model, including viscothermal effects.

[3]The porosity of the panel is defined as the ratio of the sum of the cross-sectional areas of the resonators and the total area of the panel.

the resonator length. The frequencies for which sound reduction is maximal are not only related to the length of the resonators, but also depend on the porosity of the panel.

The basic principle of sound reduction is based on local minimisation of the volume velocity of small partitions of the panel; a method that is also used in active acoustic control [38, 47]. If the volume velocities of the sound at the surface of the panel and at the entrance of the resonators are equal in magnitude but opposite in phase, they cancel out each other and no sound is radiated from the panel. Ross and Burdisso [43] applied a similar, mechanical principle for passive noise reduction by means of so-called weak radiating cells. The major drawback of their concept is that, besides large reductions of radiated sound, also large amplifications occur due to resonances of the mechanical system. A schematic representation of the weak radiating cell and the tube resonator is shown in Figure 1.5.

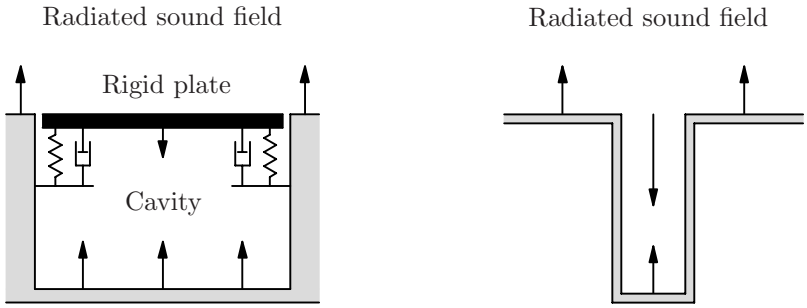


(a) Weak radiating cell. (b) Tube resonator.

**Figure 1.5**: Weak radiating cell versus tube resonator.

An example of a typical insertion loss curve for a rigid, vibrating panel with tube resonators is shown in Figure 1.4(b)[4]. The insertion loss is defined as the difference in radiated sound power between a panel with resonators and a panel without resonators. Both curves in Figure 1.4 are calculated for resonators with the same geometry. It is seen that the frequency range in which the radiated sound is reduced is broader than for sound absorption. The sound reducing properties of the structure can again be optimised by tuning the length and the radius of the resonators, and the porosity of the panel. Also, resonators of different lengths and radii can be used.

[4]The calculations were made using a one-dimensional analytical model, including viscothermal effects.

## 1.4 Problem definition

The aim of this study is to develop and validate efficient models for the prediction of sound radiation by and sound transmission through panels with tube resonators. The models are used to investigate the possibilities for the application of tube resonators for sound insulation[5].

## 1.5 Outline

For a proper understanding of the influences of the different phenomena, the models and experiments in this thesis are presented in order of increasing complexity.

In Chapter 2, the behaviour of panels with tube resonators is studied using different one-dimensional analytical models. The panels are assumed to be rigid and infinitely large. Because of the simplicity of the models, more insight is gained into the working principle of the resonators. Both sound radiation and normal incidence sound transmission are considered. For narrow tube resonators, viscothermal effects also play a role. These effects are included in the models as well. The model for sound radiation is validated by means of experiments in an impedance tube.

In Chapter 3, two two-dimensional models are presented. First, a two-dimensional semi-analytical model is presented to study the effect of scattering by the resonator openings. The panels are again assumed to be rigid and infinitely large. Both sound radiation and normal incidence sound transmission are considered. Second, a two-dimensional finite element model is presented to investigate the transmission of sound through a panel with resonators mounted between two rooms. In this model, the influences of the flexibility and the boundedness of the panel, as well as the randomness of the incident sound are taken into account.

In Chapter 4, three three-dimensional models are presented. First, the Rayleigh integral method is used to calculate the sound radiated by a panel with resonators, placed in an infinite baffle. With this model, the influence of the boundaries of the panel is studied. Subsequently, a reduced finite element model is presented. In the structural model, the panel is flexible; however, in the formulation of the acousto-elastic interaction, the resonators are still assumed to be rigid. To fully examine the influence of the flexibility of the resonators, finally, a fully coupled finite element model of a small part of a flexible panel with one resonator is introduced.

[5]This concept, as schematically shown in Figure 1.5(b), has been patented [55].

To verify whether the assumptions and simplifications that were made in the models are valid, sound transmission loss measurements were performed on two resonator panels of different configurations. The experiments, the results and the validation of the models are presented in Chapter 5.

Finally, in Chapter 6, conclusions are drawn and recommendations are made for further research. Table 1.1 shows an overview of the analysis methods and the cases that are presented in this thesis.

| | | Method | Sound radiation/ transmission | Rigid/ flexible panel | Unbounded/ bounded panel | Incident sound |
|---|---|---|---|---|---|---|
| Chapter 2 | 1D | Analytical[a] | Radiation, transmission[b] | Rigid | Unbounded | Normal |
| | 1D | Experimental | Radiation | Rigid, flexible | Unbounded | - |
| Chapter 3 | 2D | Semi-analytical | Radiation, transmission | Rigid | Unbounded | Normal |
| | 2D | Finite element method | Transmission | Flexible | Bounded | Random |
| Chapter 4 | 3D | Rayleigh integral method | Radiation | Rigid, flexible[c] | Bounded | - |
| | 3D | Finite element method | Transmission | Flexible[c] | Bounded | Normal |
| | 3D | Finite element method | Radiation, transmission | Flexible | Unbounded | Normal |
| Chapter 5 | 3D | Experimental | Transmission[b] | Flexible | Bounded | Diffuse |

**Table 1.1**: Overview of presented analysis methods and cases studied in this thesis.

[a]This method also includes viscothermal effects.
[b]Panels with tubes as well as sandwich panel configurations are considered.
[c]The flexibility of the resonators was not taken into account in the formulation of the acousto-elastic interaction.

# Chapter 2

# One-dimensional modelling and experimental validation

## 2.1 Introduction

In this chapter, different one-dimensional analytical models are described to study the radiation of sound by and the transmission of sound through panels with tube resonators. The advantage of these models is that they are relatively simple and, therefore, provide good insight into the working principle of the resonators. In the initial phase of a design, they can be used as fast analysis tools to make a rough comparison of the performance of different configurations. Moreover, they can serve as a stepping stone to the development of more sophisticated models.

Starting point for the analyses is the idealised case of an infinitely large, rigid panel with resonators. A schematic representation of the system is shown in Figure 2.1. Because of the repetitive pattern of resonators in the panel, the panel can be divided into a number of so-called characteristic areas, each area containing one resonator (see Figure 2.1). The dimensions of the characteristic areas are assumed to be small compared to the acoustic wavelength.

Now, make the assumption that the structure is vibrating with a certain uniform harmonic velocity $v_s$ in the direction perpendicular to the surface (see Figure 2.1). Since the panel is assumed to be rigid and infinitely large, the vibration only generates sound waves in that particular direction. At the boundaries of the characteristic areas, at a small distance from the panel, the fluid velocity $w$ in the direction parallel to the surface is zero (see Figure 2.1). This means that the boundaries can be regarded as symmetry planes and the sound radiated by the panel can be determined with a one-dimensional model

of only one such characteristic area.

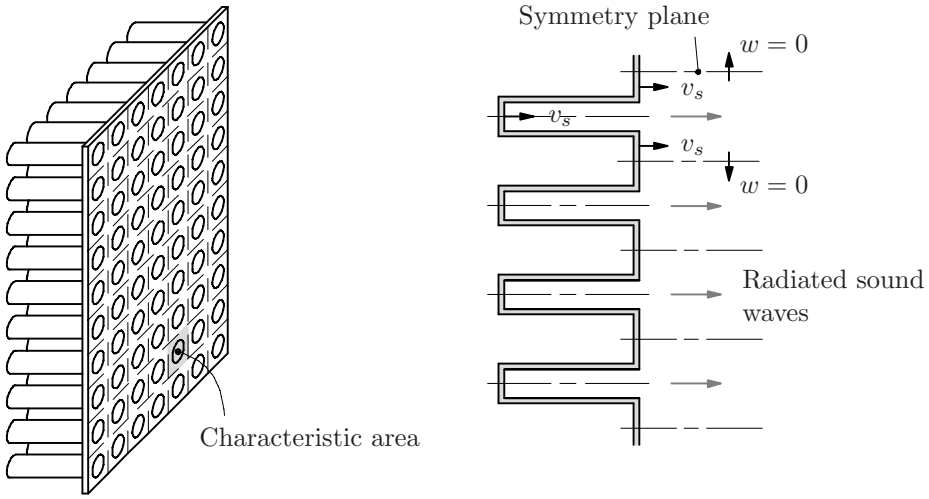


**Figure 2.1**: Part of a panel with resonators divided into characteristic areas - panel with tubes.

To model the acoustics of a panel with tube resonators, first the propagation of sound waves inside and around the axially vibrating resonators has to be known. In Section 2.2, expressions are derived for the pressures and acoustic fluid velocities in these two parts. In the first part of Section 2.3, these expressions are used to model the sound radiation by a panel with tube resonators, vibrating with a certain uniform harmonic velocity in normal direction. The vibrations can either be induced by structural or by acoustic excitation. In the second part of Section 2.3, the model for sound radiation is extended to models for normal incidence sound transmission through two different panel configurations. The vibrations of the panel are acoustically induced now. In Section 2.4, the influence of different parameters on the radiation of sound by and the transmission of sound through a panel with tube resonators is demonstrated. In Section 2.5, the model for sound radiation is validated by means of experiments in an impedance tube.

## 2.2 Viscothermal wave propagation

In this section, the propagation of sound waves inside and around the axially vibrating resonators is described. Figure 2.2 shows a schematic representation of a characteristic area with the two air volumes that are considered.

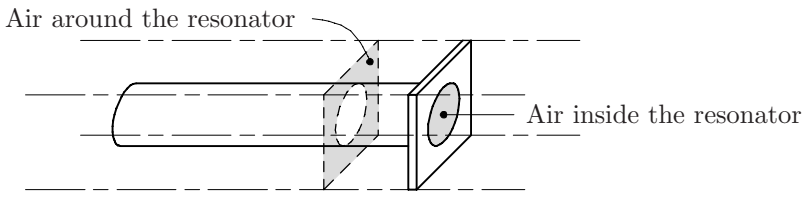


**Figure 2.2**: Different air containing parts of a characteristic area.

Usually, for wave propagation in air, only the effects of inertia and compressibility are taken into account. However, near the surface of a structure generally a so-called boundary layer is present, where viscosity and thermal conductivity also play an important role. If the dimensions of the acoustic domain perpendicular to the propagation direction are of the same order of magnitude as the boundary layer thickness, these so-called viscothermal effects cannot be neglected. The model that is used in this section takes into account both the effects of inertia and compressibility, and the effects of viscosity and thermal conductivity. This means that the solutions can also be applied for narrow tubes.

The model that is used here is the so-called low reduced frequency model, which was first introduced by Zwikker and Kosten [60]. An extensive overview of different analytical solutions for viscothermal wave propagation, presented by Tijdeman [50] and Beltman [2], shows that it is a very accurate and efficient model. In the work of Tijdeman, the solutions for the propagation of sound waves in cylindrical tubes were expressed in terms of a number of dimensionless parameters. The representation of the low reduced frequency model in terms of these dimensionless parameters is also the basis for the derivations of the acoustic variables in this section. However, because the panel and thus the resonators are vibrating here, different boundary conditions are applied.

First, the formulation of the low reduced frequency model is presented for cylindrical geometries. Next, the solutions are derived for the propagation of sound waves inside and around the resonators, respectively.

### 2.2.1 Low reduced frequency model

The basic equations governing the propagation of sound waves are the linearised Navier-Stokes equations, the equation of continuity, the equation of state for an ideal gas and the energy equation. In the absence of mean flow,

these equations can be written as [7]:

$$\rho_0 \frac{\partial \tilde{\mathbf{v}}}{\partial t} = -\nabla \tilde{p} + \left(\frac{4}{3}\mu + \mu_b\right) \nabla \left(\nabla \cdot \tilde{\mathbf{v}}\right) - \mu \nabla \times \left(\nabla \times \tilde{\mathbf{v}}\right) \tag{2.1}$$

$$\rho_0 \left(\nabla \cdot \tilde{\mathbf{v}}\right) + \frac{\partial \tilde{\rho}}{\partial t} = 0 \tag{2.2}$$

$$\tilde{p} = \tilde{\rho} R_0 \tilde{T} \tag{2.3}$$

$$\rho_0 C_p \frac{\partial \tilde{T}}{\partial t} = \lambda_T \Delta \tilde{T} + \frac{\partial \tilde{p}}{\partial t} \tag{2.4}$$

where $\tilde{\mathbf{v}}$ is the fluid velocity, $\tilde{p}$ is the pressure, $\tilde{\rho}$ is the density, $\tilde{T}$ is the temperature, $\rho_0$ is the mean density, $\mu$ is the dynamic viscosity, $\mu_b$ is the bulk viscosity, $R_0$ is the gas constant[1], $C_p$ is the specific heat at constant pressure, $\lambda_T$ is the thermal conductivity, and $t$ is time. The operator $\nabla$ is the gradient and $\Delta$ is the Laplace operator. For linear viscothermal wave propagation, the following assumptions are made: small harmonic perturbations, no mean flow, no internal heat generation, homogeneous medium, and laminar flow. For convenience, the acoustic variables are made dimensionless using the undisturbed conditions:

$$\tilde{\mathbf{v}} = \mathbf{v} e^{\mathrm{i}\omega t} \qquad = c_0 \check{\mathbf{v}} e^{\mathrm{i}\omega t} \tag{2.5}$$

$$\tilde{p} = p_0 + p e^{\mathrm{i}\omega t} \quad = p_0 \left(1 + \check{p} e^{\mathrm{i}\omega t}\right) \tag{2.6}$$

$$\tilde{\rho} = \rho_0 + \rho e^{\mathrm{i}\omega t} \quad = \rho_0 \left(1 + \check{\rho} e^{\mathrm{i}\omega t}\right) \tag{2.7}$$

$$\tilde{T} = T_0 + T e^{\mathrm{i}\omega t} \quad = T_0 \left(1 + \check{T} e^{\mathrm{i}\omega t}\right) \tag{2.8}$$

where $c_0$ is the speed of sound, $p_0$ is the mean pressure, $T_0$ is the mean temperature, i is the imaginary unit, and $\omega$ is the angular frequency[2]. Furthermore, the following dimensionless cylindrical coordinates are introduced (see Figure 2.3):

$$\xi = kx \qquad \eta = \frac{r}{l} \tag{2.9}$$

where $k = \omega / c_0$ the wave number and $l$ is the characteristic length scale. The characteristic length scale can, for example, represent the layer thickness or the tube radius. In the low reduced frequency model, some additional assumptions are made that lead to a relatively simple but accurate model. These additional assumptions are:

[1] $R_0 = C_p - C_v$, where $C_v$ is the specific heat at constant volume.

[2] In this work, only small acoustic perturbations upon the atmospheric conditions are considered. For convenience, $p$ is therefore further referred to as pressure and $\mathbf{v}$ as fluid velocity.

- the acoustic wavelength is large compared to the characteristic length scale;
- the acoustic wavelength is large compared to the boundary layer thickness.

Using these assumptions and neglecting the bulk viscosity [2], the basic equations (2.1) to (2.4), written in cylindrical coordinates, reduce to:

$$\mathrm{i}\check{v} = -\frac{1}{\gamma}\frac{\partial \check{p}}{\partial \xi} + \frac{1}{s^2}\left[\frac{\partial^2 \check{v}}{\partial \eta^2} + \frac{1}{\eta}\frac{\partial \check{v}}{\partial \eta}\right] \tag{2.10}$$

$$0 = -\frac{1}{\gamma}\frac{\partial \check{p}}{\partial \eta} \tag{2.11}$$

$$\mathrm{i}\kappa\check{\rho} = -\left[\kappa\frac{\partial \check{v}}{\partial \xi} + \frac{\partial \check{v}}{\partial \eta} + \frac{\check{v}}{\eta}\right] \tag{2.12}$$

$$\check{p} = \check{\rho} + \check{T} \tag{2.13}$$

$$\mathrm{i}\check{T} = \mathrm{i}\frac{\gamma - 1}{\gamma}\check{p} + \frac{1}{\sigma^2 s^2}\left[\frac{\partial^2 \check{T}}{\partial \eta^2} + \frac{1}{\eta}\frac{\partial \check{T}}{\partial \eta}\right] \tag{2.14}$$

where $\check{v}$ and $\check{w}$ are the dimensionless fluid velocities in axial and radial direction, respectively. Furthermore, the following dimensionless parameters are introduced:

$$\text{shear wave number} \qquad s = l\sqrt{\frac{\rho_0 \omega}{\mu}} \tag{2.15}$$

$$\text{reduced frequency} \qquad \kappa = lk \tag{2.16}$$

$$\text{square root of Prandtl number} \qquad \sigma = \sqrt{\frac{\mu C_p}{\lambda_T}} \tag{2.17}$$

$$\text{ratio of specific heats} \qquad \gamma = \frac{C_p}{C_v} \tag{2.18}$$

where $C_v$ is the specific heat at constant volume. The parameters $\sigma$ and $\gamma$ only depend on the material properties of the gas. The two most important parameters are the shear wave number and the reduced frequency. The reduced frequency $\kappa$ represents the ratio between the thickness of the air layer and the acoustic wavelength. The shear wave number $s$ is a measure for the amount of inertial effects compared to the amount of viscous effects. For large shear wave numbers the inertial effects dominate, whereas for small shear wave numbers the viscous effects are dominant. In physical terms, the shear wave number is the ratio between the thickness of the air layer and the unsteady boundary layer thickness[3]. The two additional assumptions of the low reduced

[3]The shear wave number is also called the unsteady Reynolds number.

frequency model imply that $\kappa \ll 1$ and $\kappa/s \ll 1$.

In the next sections, solutions are derived for the pressure and the fluid velocity in axial direction by solving equations (2.10) to (2.14) for different boundary conditions. From equation (2.11) it follows that the pressure is constant over the cross-section of the cylindrical geometry.

### 2.2.2 Axially vibrating cylindrical tube

The air inside the resonator is enclosed by a cylindrical tube. Since the panel vibrates, the tubes also vibrate. Tijdeman [50] presented the low reduced frequency solution for a non-vibrating cylindrical tube. In this section, the low reduced frequency model is adjusted to include the effects of the axially vibrating walls as well. The coordinate system of a cylindrical tube, vibrating harmonically in axial direction with a dimensionless velocity $\check{v}_s = v_s/c_0$, is shown in Figure 2.3. The characteristic length scale is equal to $l = R$.

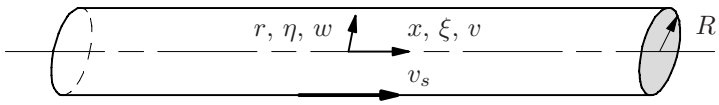


**Figure 2.3**: Axially vibrating cylindrical tube.

#### Low reduced frequency solution

The boundary conditions of the axially vibrating cylindrical tube can be formulated as follows:

$$\check{v} = \check{v}_s\,, \qquad \check{w} = 0\,, \qquad \check{T} = 0 \qquad \text{at} \quad \eta = 1 \tag{2.19}$$

$$\check{w} = 0 \qquad \text{at} \quad \eta = 0 \tag{2.20}$$

By applying these boundary conditions to equations (2.10) to (2.14), the acoustic variables are solved in the same way as presented by Tijdeman [50]. The solution for the pressure $p$ is the same as for a non-vibrating cylindrical tube[4]:

$$p(\xi) = Ae^{\Gamma\xi} + Be^{-\Gamma\xi} \tag{2.21}$$

where $A$ and $B$ are the complex amplitudes of backward and forward travelling waves, respectively, determined by the boundary conditions at the beginning

[4]Note that, for brevity, the *dimensional* solutions of the variables are written as a function of the *dimensionless* coordinates.

and the end of the tube. The propagation coefficient $\Gamma$ is defined as:

$$\Gamma = \sqrt{\frac{1}{N(s)}\frac{\gamma}{n}} \tag{2.22}$$

with:

$$N(\phi) = \frac{\mathrm{J}_2(\mathrm{i}^{3/2}\phi)}{\mathrm{J}_0(\mathrm{i}^{3/2}\phi)} \tag{2.23}$$

where $\mathrm{J}_0$ and $\mathrm{J}_2$ are the Bessel functions of the first kind of order 0 and 2, and $n$ is the polytropic coefficient, given by:

$$n = \left[1 + \frac{\gamma - 1}{\gamma} N(s\sigma)\right]^{-1} \tag{2.24}$$

The solution for the fluid velocity $v$ in axial direction can be written as:

$$v(\xi, \eta) = \frac{\mathrm{i}\Gamma}{\rho_0 c_0}\left[1 - \frac{\mathrm{J}_0(\mathrm{i}^{3/2}s\eta)}{\mathrm{J}_0(\mathrm{i}^{3/2}s)}\right]\left[Ae^{\Gamma\xi} - Be^{-\Gamma\xi}\right] + v_s\frac{\mathrm{J}_0(\mathrm{i}^{3/2}s\eta)}{\mathrm{J}_0(\mathrm{i}^{3/2}s)} \tag{2.25}$$

The first term of this equation is identical to the solution of a non-vibrating cylindrical tube. The second term in equation (2.25) accounts for the effect of the axially vibrating walls. This term only depends on the shear wave number, which means that in the present model no additional effects of heat conduction are introduced by the vibrating wall. The solutions of the other variables, $w$, $\rho$ and $T$, are the same as for a non-vibrating cylindrical tube. They can be found in the work of Tijdeman [50].

### Velocity profile

Figure 2.4 shows the influence of the shear wave number on the two terms of equation (2.25) which determine the shape of the velocity profile. The magnitude of the terms is plotted as a function of the dimensionless radius $\eta$. It is noted that the equation for the fluid velocity is complex, which means that not all points pass their equilibrium position at the same time.

As can be seen, for small values of the shear wave number, the viscous effects dominate and the velocity profile is parabolic; a so-called Poiseuille profile is approached. In this case, the magnitude of the second term approaches one and the prescribed velocity at the walls influences the velocity profile over the entire cross-section (see Figure 2.4(b)).

For large values of the shear wave number, the inertial effects dominate and a nearly flat velocity profile is obtained. The magnitude of the second

term approaches zero now, which means that the prescribed velocity at the walls hardly influences the velocity profile. Figure 2.4(a) shows that in this case the magnitude of the first term approaches one. Hence, for large values of the shear wave number, equation (2.25) converges to the solution for standard acoustic wave propagation[5]. The same holds for the pressure described by equation (2.21). In the case of standard acoustic wave propagation, $\Gamma = \mathrm{i}$ and $n = \gamma$. Under this condition, the solutions for the variables are independent of the cross-sectional shape of the tube and the conditions at the walls.

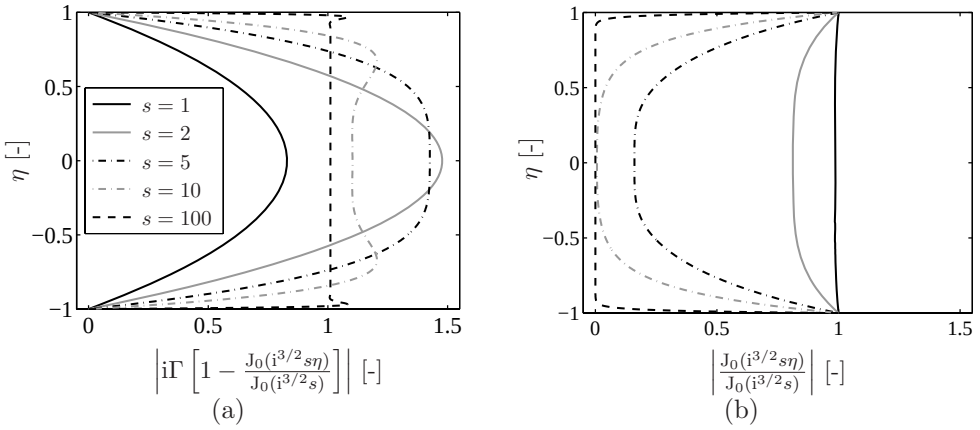


**Figure 2.4**: Magnitude of terms of equation (2.25) determining the shape of the velocity profile, plotted for different values of the shear wave number.

For the models described in Section 2.3, the axial velocity as defined by equation (2.25) is averaged over the cross-section of the tube. This leads to the following expression:

$$\bar{v}(\xi) = -\frac{\mathrm{i}\gamma}{\Gamma n}\frac{1}{\rho_0 c_0}\left[Ae^{\Gamma\xi} - Be^{-\Gamma\xi}\right] + v_s\left[\frac{\gamma}{\Gamma^2 n} + 1\right] \tag{2.26}$$

In the other sections, the bar will be omitted, so the symbol $v$ is used for the velocity in axial direction *averaged* over the cross-section.

### 2.2.3 Cylindrical layer with axially vibrating inner wall and symmetry conditions at outer boundaries

For determining the sound transmission through a panel with resonators, not only the propagation of sound waves inside the resonators has to be known,

[5]The standard acoustic solutions for the pressure and the axial velocity are obtained by solving the one-dimensional Helmholtz equation and Euler's equation, respectively. The air is assumed to be inviscid and no effects of thermal conductivity are taken into account.

but also the propagation of sound waves around the resonators. The cross-sectional shape of the air volume around a resonator is shown in Figures 2.2 and 2.5. At the circular inner boundaries, the acoustically hard walls of the resonator are vibrating harmonically in axial direction with a dimensionless velocity $\check{v}_s = v_s/c_0$. At the square outer boundaries of the characteristic area, symmetry conditions apply, i.e. the derivative of any variable in that direction is zero.

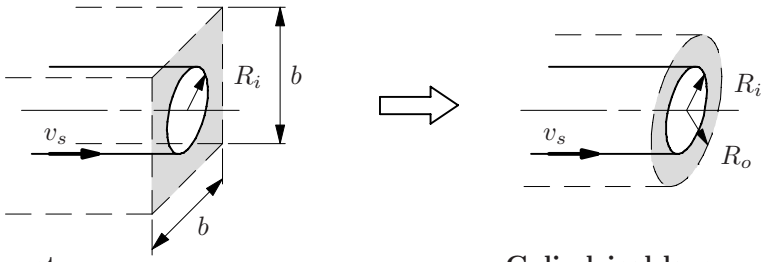


**Figure 2.5**: Approximation of the square outer boundaries of the characteristic area by a circle with an equivalent radius $R_o$.

To derive the low reduced frequency solution for this configuration, it is more convenient to have equally shaped boundaries. In Appendix A.1 it is shown that the main parameters of the low reduced frequency model for a tube with a circular and a square cross-section are nearly equal if the shear wave numbers of both geometries are the same. The square outer boundaries of the air layer are therefore approximated by a circle with an equivalent radius $R_o$ (see Figure 2.5). In this way, a cylindrical layer is obtained, for which the equations of the low reduced frequency model are more convenient to solve. The equivalent radius $R_o$ is chosen such that the shear wave number of the original geometry is the same as the shear wave number of the cylindrical layer. The definition of the shear wave number is given by equation (2.15). For a tube of arbitrary cross-sectional shape, the characteristic length scale $l$ in this expression can be defined as [42, 48]:

$$l = \frac{2S}{P} \tag{2.27}$$

where $S$ is the cross-sectional area, and $P$ is the wetted perimeter[6]. The wetted perimeter is the perimeter of the structure which is in contact with the air. For both geometries, this parameter equals the perimeter of the resonator,

[6]The characteristic length scale is defined here as twice the so-called hydraulic radius.

since only here a wall is present, and thus a viscous boundary layer. Since the wetted perimeter is the same in both cases, the cross-sectional areas also have to be equal. For a square characteristic area of width $b$, this condition leads to the following expression for the equivalent radius:

$$R_o = \frac{b}{\sqrt{\pi}} \tag{2.28}$$

### Cylindrical layer

Figure 2.6 shows the coordinate system of a cylindrical layer with an acoustically hard, axially vibrating inner wall and symmetry conditions at the outer boundaries. According to equation (2.27), the characteristic length scale $l$ can be written as:

$$l = \frac{R_o^2 - R_i^2}{R_i} \tag{2.29}$$

where $R_i$ is the inner radius of the cylindrical layer.

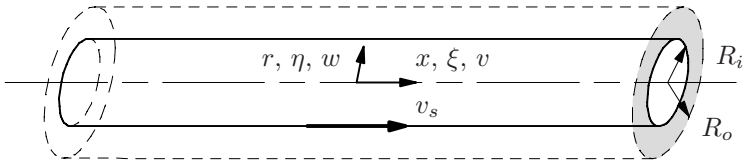


**Figure 2.6**: Cylindrical layer with axially vibrating inner wall and symmetry conditions at the outer boundaries.

### Low reduced frequency solution

With $\eta_i = R_i/l$ and $\eta_o = R_o/l$ defined as the dimensionless inner and outer radius, respectively, the boundary conditions can be formulated as follows:

$$\check{v} = \check{v}_s\,, \qquad \check{w} = 0\,, \qquad \check{T} = 0 \qquad \text{at} \quad \eta = \eta_i \tag{2.30}$$

$$\frac{\partial \check{v}}{\partial \eta} = 0\,, \qquad \check{w} = 0\,, \qquad \frac{\partial \check{T}}{\partial \eta} = 0 \qquad \text{at} \quad \eta = \eta_o \tag{2.31}$$

By applying these boundary conditions to equations (2.10) to (2.14), the acoustic variables can be solved (see Appendix A.2). The solution for the pressure $p$ is similar to that of a non-vibrating cylindrical tube:

$$p(\xi) = Ae^{\Gamma\xi} + Be^{-\Gamma\xi} \tag{2.32}$$

where the propagation coefficient $\Gamma$ is again described by equation (2.22). However, the function $N(\phi)$ in this equation is now given by:

$$N(\phi) = -1 + \frac{2}{\eta_o^2 - \eta_i^2} \frac{1}{\sqrt{\mathrm{i}}\phi} \Big\{ D_1(\phi) \Big[ \eta_o \mathrm{I}_1(\sqrt{\mathrm{i}}\phi\eta_o) - \eta_i \mathrm{I}_1(\sqrt{\mathrm{i}}\phi\eta_i) \Big] + \\ - D_2(\phi) \Big[ \eta_o \mathrm{K}_1(\sqrt{\mathrm{i}}\phi\eta_o) - \eta_i \mathrm{K}_1(\sqrt{\mathrm{i}}\phi\eta_i) \Big] \Big\} \tag{2.33}$$

where:

$$D_1(\phi) = \frac{\mathrm{K}_1(\sqrt{\mathrm{i}}\phi\eta_o)}{\mathrm{I}_0(\sqrt{\mathrm{i}}\phi\eta_i)\mathrm{K}_1(\sqrt{\mathrm{i}}\phi\eta_o) + \mathrm{K}_0(\sqrt{\mathrm{i}}\phi\eta_i)\mathrm{I}_1(\sqrt{\mathrm{i}}\phi\eta_o)} \tag{2.34a}$$

$$D_2(\phi) = \frac{\mathrm{I}_1(\sqrt{\mathrm{i}}\phi\eta_o)}{\mathrm{I}_0(\sqrt{\mathrm{i}}\phi\eta_i)\mathrm{K}_1(\sqrt{\mathrm{i}}\phi\eta_o) + \mathrm{K}_0(\sqrt{\mathrm{i}}\phi\eta_i)\mathrm{I}_1(\sqrt{\mathrm{i}}\phi\eta_o)} \tag{2.34b}$$

In these expressions, $\mathrm{I}_0$, $\mathrm{I}_1$, $\mathrm{K}_0$ and $\mathrm{K}_1$ are the modified Bessel functions of the first and second kind of order 0 and 1, respectively. The solution is written in terms of modified Bessel functions to avoid some numerical problems that arise with the ordinary Bessel functions. The solution for the axial velocity $v$ can be written as:

$$v(\xi,\eta) = \frac{\mathrm{i}\Gamma}{\rho_0 c_0} D(s,\eta) \Big[ A e^{\Gamma\xi} - B e^{-\Gamma\xi} \Big] + \\ + v_s \Big[ D_1(s)\mathrm{I}_0(\sqrt{\mathrm{i}}s\eta) + D_2(s)\mathrm{K}_0(\sqrt{\mathrm{i}}s\eta) \Big] \tag{2.35}$$

with:

$$D(s,\eta) = 1 - D_1(s)\mathrm{I}_0(\sqrt{\mathrm{i}}s\eta) - D_2(s)\mathrm{K}_0(\sqrt{\mathrm{i}}s\eta) \tag{2.36}$$

As in the expression for the axially vibrating cylindrical tube, the second term in equation (2.35) accounts for the effect of the vibrating wall. It does not introduce any additional effects of heat conduction.

### Velocity profile

Figure 2.7 shows the influence of the shear wave number on the two terms of equation (2.35) which determine the shape of the velocity profile. The magnitude of the expressions is plotted as a function of the dimensionless radius $\eta$. The influence of the shear wave number is similar to that for an axially vibrating cylindrical tube. For large values of the shear wave number, equations (2.32) and (2.35) converge to the solutions for standard acoustic wave propagation.

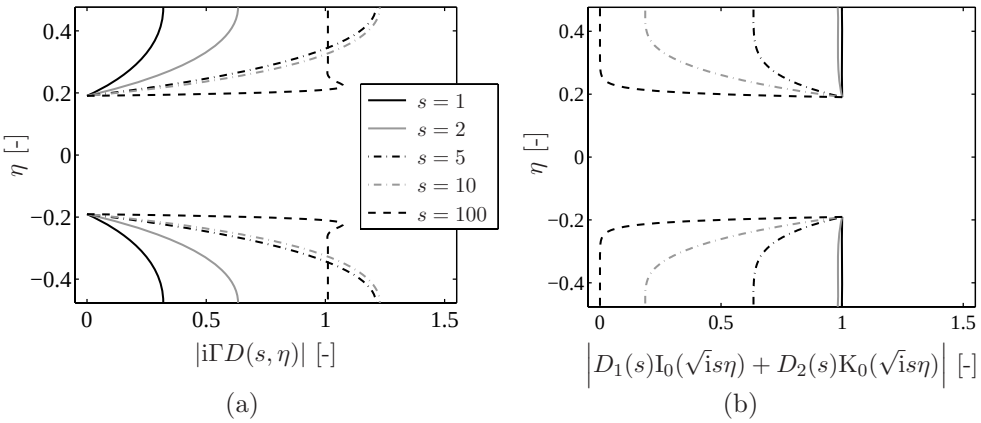


**Figure 2.7**: Magnitude of the two terms of equation (2.35) determining the shape of velocity profile, plotted for different values of the shear wave number ($R_i/R_o = 0.4$).

For the models described in Section 2.3, the velocity in axial direction as defined by equation (2.35) is averaged over the cross-section of the layer. This leads to the following expression:

$$\bar{v}(\xi) = -\frac{\mathrm{i}\gamma}{\Gamma n}\frac{1}{\rho_0 c_0}\left[Ae^{\Gamma\xi} - Be^{-\Gamma\xi}\right] + v_s\left[\frac{\gamma}{\Gamma^2 n} + 1\right] \tag{2.37}$$

It should be noted that this equation has the same form as the expression for the axial velocity in an axially vibrating cylindrical tube. Only the propagation coefficient $\Gamma$ and the polytropic coefficient $n$ are defined differently now. In the other sections, the bar will be omitted, so the symbol $v$ is used for the velocity in axial direction *averaged* over the cross-section.

## 2.3 One-dimensional analytical models

In this section, two one-dimensional models are presented to describe the sound radiated by and transmitted through a panel with tube resonators.

### 2.3.1 Sound radiation

Figure 2.8 shows the model of a characteristic area of a panel with tube resonators. The model consists of two parts: the sound field inside the resonator and the radiated sound field in front of the panel. The pressure $p_1$ and the axial velocity $v_1$ inside the resonator are described by equations (2.21) and

(2.26), respectively. For the pressure $p_2$ and the axial velocity $v_2$ of the radiated sound field, the standard acoustic solutions are used. The sound field in the resonator is defined with reference to the axial coordinate $x_{\mathrm{I}}$ and the radiated sound field is defined with reference to coordinate $x_{\mathrm{II}}$ (see Figure 2.8). $A_1$ and $B_1$ are the pressure amplitudes of the backward and forward travelling sound waves in the resonator, respectively. $B_2$ is the pressure amplitude of the radiated sound wave. These amplitudes are determined by the boundary conditions of the system. Since the sound is radiated to the far field, no reflection is assumed to take place and the pressure amplitude $A_2$ equals zero.

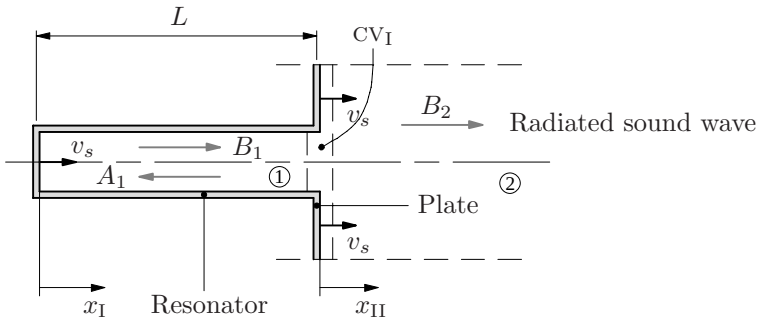


**Figure 2.8**: Model of sound radiation by a rigid characteristic area.

Assuming that the plate and the resonator vibrate harmonically with the same normal velocity $v_s$, three boundary conditions can be formulated. The first boundary condition states that the fluid velocity at the end of the resonator is equal to the velocity of the structure (no-slip condition). At the entrance of the resonator, the pressure is assumed to be continuous and conservation of mass is applied for the control volume $\mathrm{CV_I}$, indicated by the dashed lines in Figure 2.8. All together, these boundary conditions can be written as:

$$v_1|_{x_{\mathrm{I}}=0} = v_s \tag{2.38}$$

$$p_1|_{x_{\mathrm{I}}=L} = p_2|_{x_{\mathrm{II}}=0} \tag{2.39}$$

$$v_1|_{x_{\mathrm{I}}=L}\, S_r + v_s\,(S - S_r) = v_2|_{x_{\mathrm{II}}=0}\, S \tag{2.40}$$

where $S_r$ is the cross-sectional area of the resonator, $S$ is the characteristic area, and $L$ is the effective length of the resonator. Due to inlet effects at the entrance of the resonator, the effective length of the resonator is slightly larger than the physical length of the resonator (see Section 2.5). By applying these boundary conditions to equations (2.21) and (2.26), the unknown pressure amplitudes $A_1$, $B_1$ and $B_2$ can be solved for a given structural velocity $v_s$.

Subsequently, the radiated sound power is determined as will be described in Section 2.4.1.

### 2.3.2 Sound transmission

In this section, one-dimensional analytical models are presented to predict the transmission of sound through two panel configurations. One is a thin plate with tubes attached to it (see Figure 2.1), referred to here as panel with tubes. The other is a sandwich panel with one of the plates perforated (see Figure 2.9), referred to here as sandwich panel. The advantage of the last configuration is that it can be manufactured easily, for example, by perforating one of the skin panels of a common honeycomb sandwich panel. In both cases, normal incident plane waves are considered.

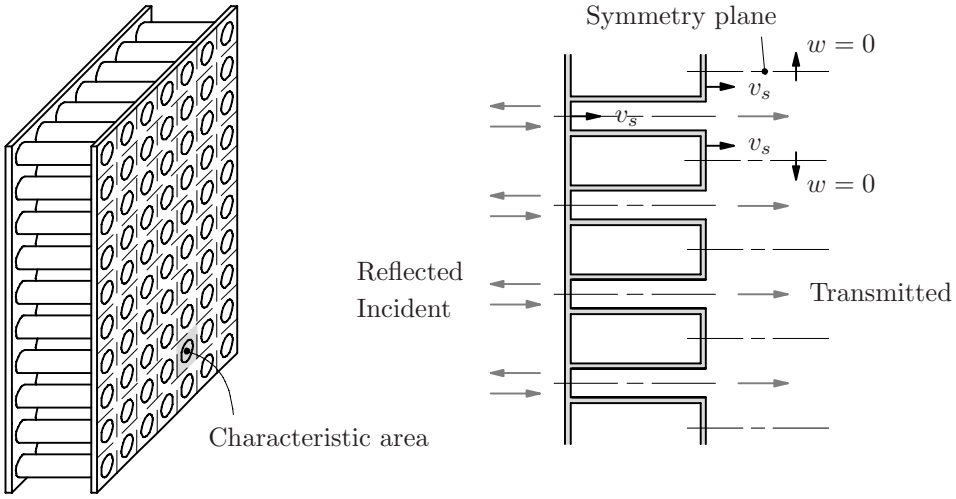


**Figure 2.9**: Part of a panel with resonators divided into characteristic areas - sandwich panel.

#### Panel with tubes

Figure 2.10 shows the model of a characteristic area of a panel with tubes. The model consists of four parts: the sound fields in front of the panel, behind the panel, inside the resonator and around the resonator. Due to acoustic excitation, the structure is assumed to vibrate harmonically with an unknown normal velocity $v_s$. The sound fields at the right-hand side of the panel are modelled in the same way as in the previous section. The pressure $p_3$ and the

axial velocity $v_3$ around the resonator are described by equations (2.32) and (2.37), respectively. For the pressure $p_4$ and the axial velocity $v_4$ of the incident sound field, the standard acoustic solutions are used. Both sound fields are defined with reference to coordinate $x_\mathrm{I}$ (see Figure 2.10). $A_3$ and $B_3$ are the pressure amplitudes of the backward and forward travelling waves around the resonators, respectively, and $A_4$ and $B_4$ are the pressure amplitudes of the incident and reflected sound waves, respectively. These pressure amplitudes, as well as the structural velocity $v_s$, are determined by the boundary conditions of the system and the equation of motion.

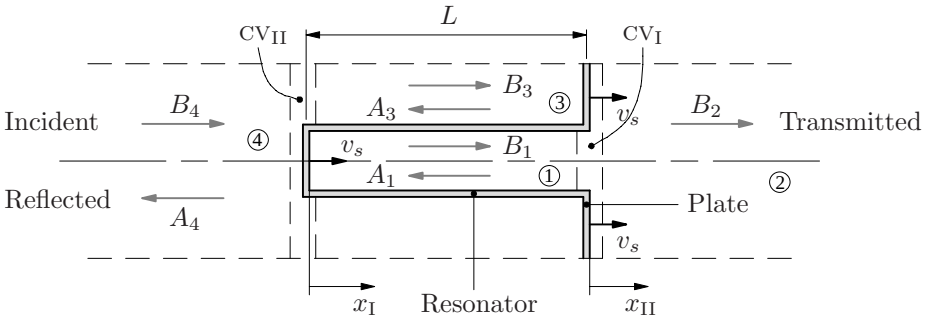


**Figure 2.10**: Model of normal incidence sound transmission through a rigid characteristic area - panel with tubes.

For the right-hand side of the panel, the boundary conditions described by equations (2.38) to (2.40) remain the same. Additionally, at the left-hand side of the panel similar boundary conditions have to be satisfied:

$$v_3|_{x_\mathrm{I}=L} = v_s \tag{2.41}$$

$$p_3|_{x_\mathrm{I}=0} = p_4|_{x_\mathrm{I}=0} \tag{2.42}$$

$$v_3|_{x_\mathrm{I}=0}\,(S - S_r) + v_s\,S_r = v_4|_{x_\mathrm{I}=0}\,S \tag{2.43}$$

Furthermore, equilibrium of forces is required for the entire system:

$$p_4|_{x_\mathrm{I}=0}\,S_r + p_3|_{x_\mathrm{I}=L}\,(S - S_r) - p_1|_{x_\mathrm{I}=0}\,S_r - p_2|_{x_\mathrm{I}=0}\,(S - S_r) = mi\omega v_s \tag{2.44}$$

where $m$ is the mass of the characteristic area. By applying these boundary conditions to equations (2.21), (2.26), (2.32) and (2.37), the unknown pressure amplitudes $A_1$, $B_1$, $B_2$, $A_3$, $B_3$ and $A_4$ and the structural velocity $v_s$ can be solved for a given incident pressure amplitude $B_4$. Subsequently, the sound transmission loss of the panel is determined as will be described in Section 2.4.2.

**Sandwich panel**

The model of a characteristic area of a sandwich panel (see Figure 2.11) consists of the same four sound fields as the model of a panel with tubes. To solve the unknown pressure amplitudes and the structural velocity, a similar set of boundary conditions can be formulated. The boundary conditions described by equations (2.38) to (2.41) remain the same. The other boundary conditions change into:

$$v_3|_{x_\mathrm{I}=0} = v_s \tag{2.45}$$

$$v_4|_{x_\mathrm{I}=0} = v_s \tag{2.46}$$

$$\begin{aligned} p_4|_{x_\mathrm{I}=0}\, S - p_1|_{x_\mathrm{I}=0}\, S_r - p_3|_{x_\mathrm{I}=0}\, (S - S_r) + \\ + p_3|_{x_\mathrm{I}=L}\, (S - S_r) - p_2|_{x_\mathrm{II}=0}\, (S - S_r) = m\mathrm{i}\omega v_s \end{aligned} \tag{2.47}$$

By applying these boundary conditions to equations (2.21), (2.26), (2.32) and (2.37), the unknown pressure amplitudes $A_1$, $B_1$, $B_2$, $A_3$, $B_3$ and $A_4$ and the structural velocity $v_s$ can be solved again for a given incident pressure amplitude $B_4$.

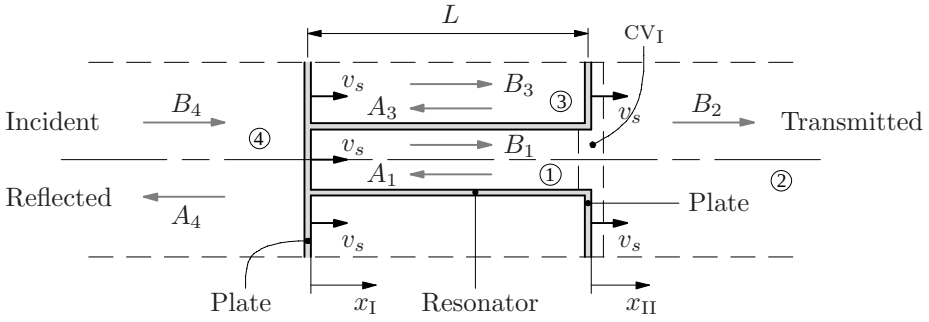


**Figure 2.11**: Model of normal incidence sound transmission through a rigid characteristic area - sandwich panel.

## 2.4 Parameter study

In this section, the models developed in Section 2.3 are used to explain the working principle of the resonators and to examine the influence of different parameters on the radiated and transmitted sound.

### 2.4.1 Sound radiation

The working principle of the resonators is explained in more detail by examining the influence of the porosity on the sound radiated by the rigid characteristic area. The porosity $\Omega = S_r/S$ of the panel is defined as the ratio of the cross-sectional area of the resonators $S_r$ and the characteristic area $S$. Subsequently, the influence of viscothermal effects is presented.

#### Radiated sound power

A measure to quantify the reduction of radiated sound is the so-called insertion loss. The insertion loss $IL$ corresponds to the difference in radiated sound power level between a panel without resonators $L_{W0}$ and a panel with resonators $L_{Wr}$:

$$IL = L_{W0} - L_{Wr} \tag{2.48}$$

The sound power level is defined as:

$$L_W = 10 \log_{10} \left( \frac{\bar{W}}{\bar{W}_{\text{ref}}} \right) \tag{2.49}$$

where $\bar{W}_{\text{ref}} = 1 \cdot 10^{-12}$ W is the reference power and the time-averaged sound power $\bar{W}$ is calculated by:

$$\bar{W} = \int_S \bar{I}_n(\mathbf{r}) \mathrm{d}S \tag{2.50}$$

with $\bar{I}_n(\mathbf{r})$ the time-averaged sound intensity at position $\mathbf{r}$ in the direction $n$ normal to the surface area $S$. In the case of harmonic time dependence, the time-averaged sound intensity is defined as:

$$\bar{I}_n(\mathbf{r}) = \frac{1}{2} \mathrm{Re} \left[ p(\mathbf{r}) v_n^*(\mathbf{r}) \right] \tag{2.51}$$

where $^*$ denotes the complex conjugate [22]. In this thesis, the terms sound power and sound intensity will be used as abbreviations of time-averaged sound power and time-averaged sound intensity.

### Influence of the porosity

Figure 2.12 shows the insertion loss for different values of the porosity[7]. No viscothermal effects are included. It is seen that by tuning the dimensions of the resonators, considerable reductions of the radiated sound power can be obtained over a broad frequency range.

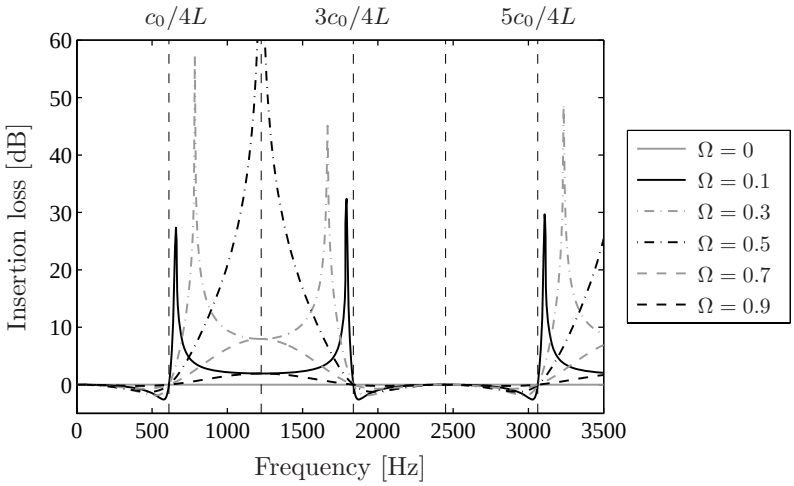


**Figure 2.12**: Insertion loss for different porosities ($L = 0.14$ m).

Equation (2.40) shows that no sound is radiated by the characteristic area if the volume velocities at the entrance of the resonators and at the vibrating panel surface are equal in magnitude and opposite in phase, so:

$$\left| v_1|_{x_\mathrm{I}=L} \right| S_r \;=\; v_s\,(S - S_r) \qquad\qquad \angle\, v_1|_{x_\mathrm{I}=L} - \angle v_s = \pm\pi \tag{2.52}$$

If the porosity is very small, this is achieved when the fluid velocity at the entrance of the resonator is very large compared to the velocity of the structure, so:

$$S_r \ll S \qquad \rightarrow \qquad \left| v_1|_{x_\mathrm{I}=L} \right| \gg v_s \tag{2.53}$$

Figure 2.13(a) shows that this occurs near the frequencies $f$ for which a quarter, or odd multiples of a quarter, of the acoustic wavelength $\lambda = c_0/f$ equals the length of the resonator, i.e. $f \approx (2j+1)c_0/4L$ with $j = 0, 1, 2, \ldots$. At these frequencies, the air inside the resonator is in resonance, which causes the large fluid velocities at the entrance of the resonator. In Figure 2.14 it can be

[7]For all calculations in this thesis the following air conditions were used: $c_0 = 343$ m/s, $\rho_0 = 1.2$ kg/m$^3$, $\mu = 18.2 \cdot 10^{-6}$ Ns/m$^2$, $\gamma = 1.4$ and $\sigma = 0.845$.

seen that, indeed, no sound is radiated at these frequencies. The magnitude of the transfer function $B_2/v_s$ is plotted here as a function of the frequency. The pressure amplitude $B_2$ of the radiated sound wave (see Figure 2.8), which is linearly dependent on the excitation velocity $v_s$, determines directly the sound power radiated by a characteristic area. The volume velocities at the entrance of the resonator and at the panel surface are shown in Figure 2.15.

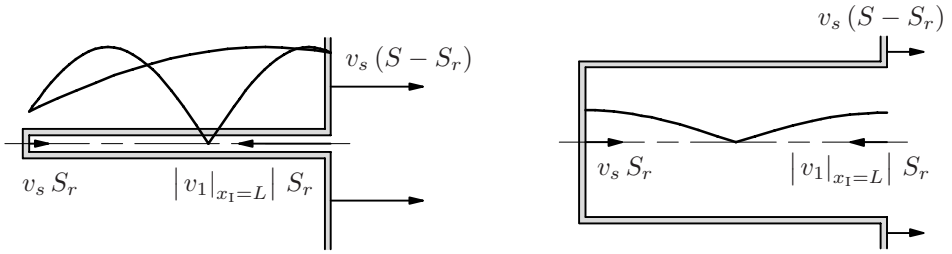


(a) $\Omega \ll 1$ at $f = c_0/4L$ and $f = 3c_0/4L$. (b) $\Omega = 0.5$ at $f = c_0/2L$.

**Figure 2.13**: Axial fluid velocity distribution (magnitude) over the length of the resonator at the frequencies for which maximum sound reduction is obtained. The arrows indicate the volume velocities.

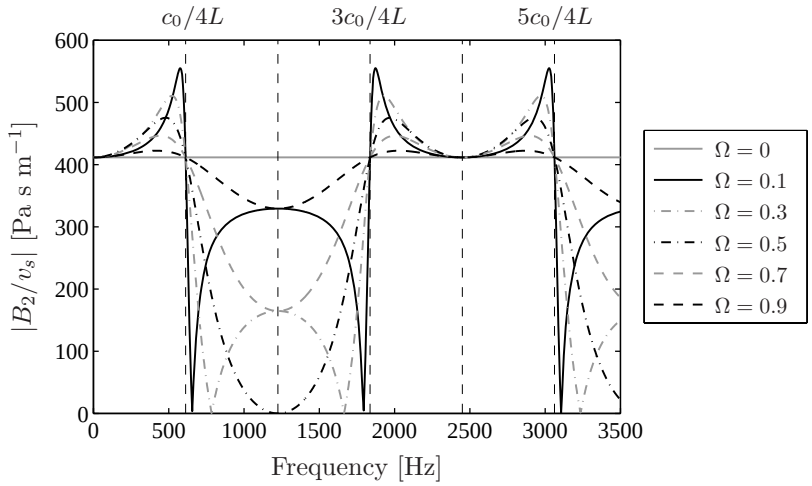


**Figure 2.14**: Radiated sound for different porosities ($L = 0.14$ m).

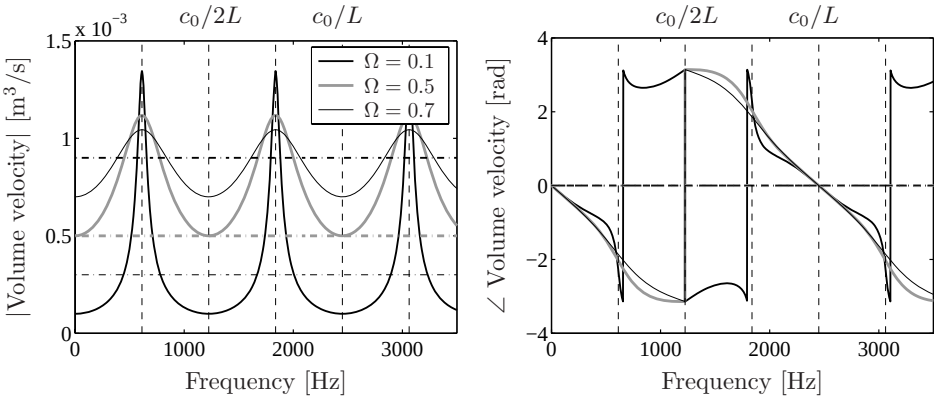


(a) Magnitude. (b) Phase.

**Figure 2.15**: Volume velocities at the entrance of the resonator $v_1|_{x_1=L}\, S_r$ (solid lines) and at the panel surface $v_s\,(S - S_r)$ (dash-dotted lines) for different porosities ($L = 0.14$ m, $S = 1 \cdot 10^{-4}$ m$^2$, $v_s = 1$ m/s).

If the porosity is $\Omega = 0.5$, equation (2.52) is satisfied when the magnitude of the fluid velocity at the entrance of the resonator is equal to the magnitude of the velocity of the structure, so:

$$S_r = S \qquad \rightarrow \qquad \left| v_1|_{x_1=L} \right| \; = \; v_s \tag{2.54}$$

In Figure 2.13(b) it is seen that this occurs at frequencies for which a half, or odd multiples of a half, of the acoustic wavelength corresponds with the length of the resonator, i.e. $f = (2j+1)c_0/2L$ with $j = 0, 1, 2, \ldots$. This is also seen in Figure 2.14. For a porosity of $\Omega = 0.5$ large reductions in radiated sound power are obtained in a relatively broad frequency range. If the porosity approaches one, the results converge to the sound radiated by a rigid characteristic area without a resonator.

In Figure 2.14 it is also seen that the amplitude of the radiated sound pressure can only be zero if the porosity is $\Omega \leq 0.5$. The standard acoustic solution for the fluid velocity at the entrance of the resonator is:

$$v_1|_{x_1=L} \; = \; v_s \, \frac{1 + \mathrm{i}(\Omega - 1)\sin(kL)}{\cos(kL) + \mathrm{i}\Omega \sin(kL)} \tag{2.55}$$

which means that $\left| v_1|_{x_1=L} \right| \geq v_s$. Hence, to satisfy the condition for zero sound radiation as described by equation (2.52), the areas have to be such that $S_r \leq S - S_r$, or $\Omega \leq 0.5$.

At the frequencies $f = (2j + 1)c_0/4L$ with $j = 0, 1, 2, \ldots$, the radiated sound power of a panel with resonators is equal to the radiated sound power of a panel without resonators. In the frequency ranges $jc_0/L < f < (1/4+j)c_0/L$ and $(3/4 + j)c_0/L < f < (1 + j)c_0/L$ with $j = 0, 1, 2, \ldots$, more sound is radiated than by a panel without resonators. However, the amplifications are much smaller than the reductions that are obtained.

The insertion loss integrated over a frequency range of $jc_0/L < f < (j + 1)c_0/L$ with $j = 0, 1, 2, \ldots$ is maximal for a porosity of $\Omega = 0.5$. The integral of the transfer function $|B_2/v_s|$ over the same frequency range is minimal for a porosity of $\Omega = 0.44$.

### Viscothermal effects

Figure 2.16 shows the influence of the viscothermal effects on the insertion loss. The porosity is kept constant at $\Omega = 0.45$, while the resonator radius is varied. If the resonator radius decreases, the viscothermal effects increase, which causes a decrease of both the amplifications and the reductions of the radiated sound. The frequency range over which the noise is reduced broadens and it is possible to obtain larger reductions at lower frequencies without lengthening the resonators. Since the shear wave number decreases with decreasing frequency, more viscothermal effects are observed at lower frequencies. Furthermore, it is seen that the locations of the maxima shift slightly to lower frequencies. This is caused by the fact that due to viscous effects, the effective speed of sound $c_{\text{eff}} = c_0/\text{Im}(\Gamma)$ is lower than the undisturbed speed of sound $c_0$. Figure 2.17 shows that at the frequencies of maximum sound reduction, the pressure amplitude $B_2$ of the radiated sound wave no longer becomes zero. Due to viscothermal effects, damping is introduced, which lowers the velocity at the entrance of the resonators and decreases the heights of the peaks and troughs in the insertion loss curve. For small resonator radii, the decrease of the troughs even results in a complete disappearance of the amplifications. In Figure 2.18, the volume velocities at the entrance of the resonator and at the panel surface are shown with and without viscothermal effects.

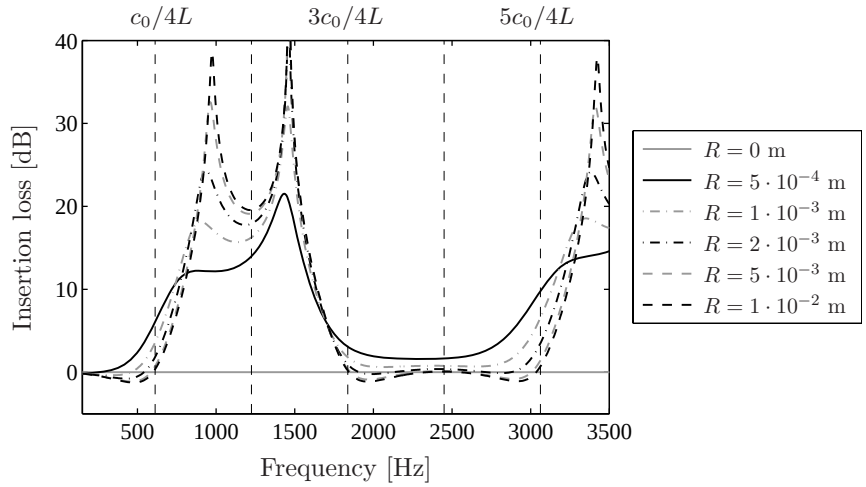


**Figure 2.16**: Insertion loss for different resonator radii ($L = 0.14$ m, $\Omega = 0.45$).

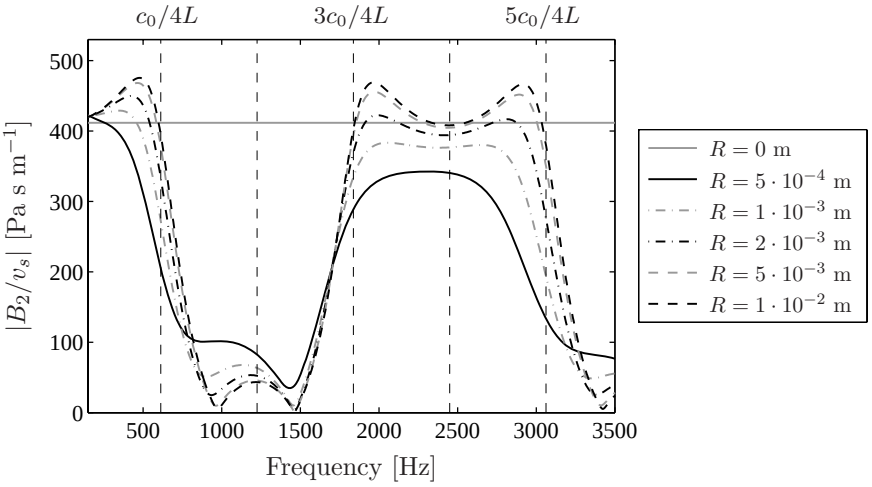


**Figure 2.17**: Radiated sound for different resonator radii ($L = 0.14$ m, $\Omega = 0.45$).

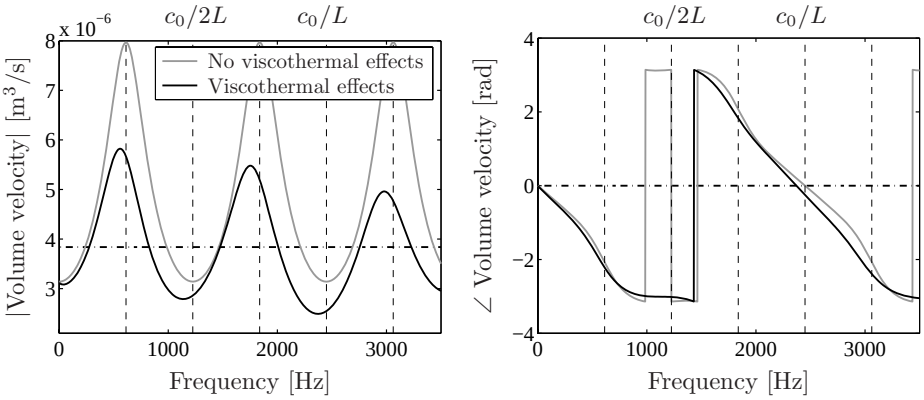


(a) Magnitude. (b) Phase.

**Figure 2.18**: Volume velocities at the entrance of the resonator $v_1|_{x_1=L}\, S_r$ (solid lines) and at the panel surface $v_s\,(S - S_r)$ (dash-dotted lines) ($L = 0.14$ m, $R = 1 \cdot 10^{-3}$ m, $\Omega = 0.45$, $v_s = 1$ m/s).

### Folded resonators

In the study described above, it was seen that the frequency range in which the radiated sound is reduced is determined by the length of the resonators. For sound reduction at low frequencies, relatively long resonators are necessary. For some applications, this may be impractical because of limited space. One of the possibilities to reduce the length of the resonators is by folding them [35]. In this section, the performance of two types of folded resonators is demonstrated. Schematic representations of the two configurations are shown in Figure 2.19. The models for sound radiation, as well as the experimental validation of one of these models, are presented in Appendix C. If no viscothermal effects are taken into account, the mathematical models for both resonator types are the same.

In Figure 2.20 the performance of the folded resonators is shown for different ratios of the tube or layer lengths $L_1$ and $L_2$ (see Figures C.1 and C.2). In all cases, the porosity and the total length of the resonators are kept the same and no viscothermal effects are included. The different parts of the resonators are indicated in Figure 2.19 by ① and ②. For both resonators, the cross-sectional area of part ① is chosen to be equal to the cross-sectional area of part ②. It can be seen that by folding the resonator, the insertion loss changes considerably. This is mainly caused by the fact that the bend in the bent tube resonator and the transition from tube to cylindrical layer in the tube-in-tube

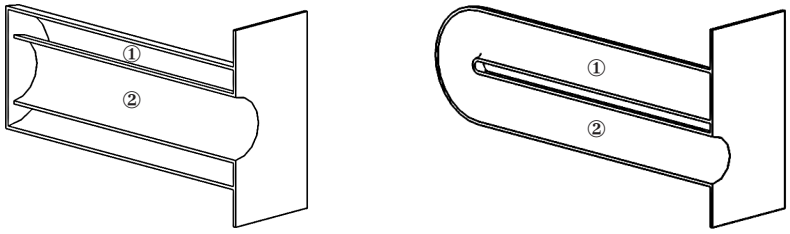


(a) Tube-in-tube resonator. (b) Bent resonator.

**Figure 2.19**: Cross-sectional view of different types of folded resonators [35].

resonator behave as additional volume sources. Another difference is that the ends of the folded resonators vibrate in the direction opposite to the end of an unfolded resonator.

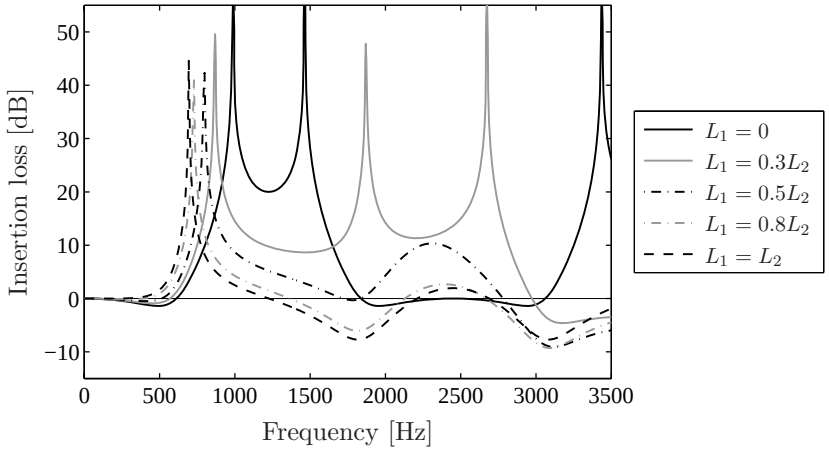


**Figure 2.20**: Insertion loss of folded resonators for different ratios of the tube or layer lengths ($L_1 + L_2 = 0.14$ m, $\Omega = 0.45$).

Figure 2.21 shows the insertion loss of folded resonators for different porosities. The lengths and the cross-sectional areas of both parts are chosen to be the same. The results are compared with unfolded resonators of the same total length and the same porosity. It is seen that, for a large porosity, the performance deteriorates a lot by folding the resonator. For small porosities, similar reductions can be achieved as with unfolded resonators. Only the centre frequency of the range in which reduction is obtained shifts from $f = c_0/2L$ to $f = c_0/L$. This means that folding the resonators such that $L_1 = L_2 = L/2$ is useless, unless reductions are only desired in a small frequency range around

$f = c_0/4L$. To find a configuration that satisfies the required sound reduction while minimising the thickness of the panel, the dimensions of the different parts of the resonators can be tuned using optimisation [35]. Viscothermal effects have similar influences on the radiated sound as in cases of unfolded tube resonators.

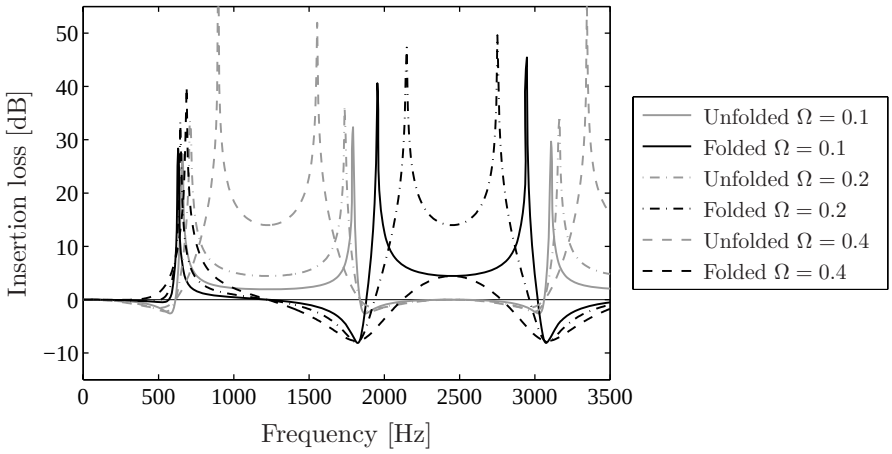


**Figure 2.21**: Insertion loss of folded ($L = 0.14$ m) and unfolded ($L_1 = L_2 = 0.07$ m) resonators for different porosities.

### 2.4.2 Sound transmission

In this section, the influence of the porosity and the viscothermal effects on the sound transmission through a panel with resonators is presented.

#### Sound transmission loss

The conventional measure for the amount of sound that is transmitted through a panel is the sound transmission loss $TL$. The transmission coefficient $\tau$ is defined as the ratio of the transmitted sound power and the incident sound power. For the models of both configurations presented in Section 2.3.2, this can be written as:

$$\tau = \left| \frac{B_2}{B_4} \right|^2 \tag{2.56}$$

The sound transmission loss is directly related to the transmission coefficient by:

$$TL = 10 \log_{10} \left( \frac{1}{\tau} \right) \tag{2.57}$$

In Chapter 1, it was seen that above the first structural eigenfrequency, the sound transmission loss of an isotropic panel without resonators is described by the so-called mass law. In this frequency range, the transmission of sound is mainly controlled by the mass per unit area of the panel. Damping and stiffness do not play a significant role then. For normal incidence, the mass law is given by:

$$TL = 10 \log_{10} \left[ 1 + \left( \frac{\bar{m}\omega}{2\rho_0 c_0} \right)^2 \right] \tag{2.58}$$

where $\bar{m}$ is the mass per unit area of the panel. The transmission loss increases with 6 dB per doubling of frequency and 6 dB per doubling of mass. In this thesis, the mass law (i.e. the sound transmission loss of a panel with the same mass, but without resonators) is used as a reference to evaluate the performance of panels with resonators.

### Influence of the porosity

Figure 2.22 shows the transmission loss of a characteristic area of a panel with tubes and a sandwich panel for different porosities. No viscothermal effects are included. As can be seen, large increases in sound transmission loss are predicted over a broad frequency range, compared with the normal incidence mass law. The increase in transmission loss of the sandwich panel is slightly smaller than that of the panels with tubes. Internal resonances in the cavities of the sandwich panel cause an extra peak and trough in the transmission loss curve at frequencies for which a half, and odd multiples of a half, of the acoustic wavelength is equal to the length of the resonator. The other peaks in the transmission loss curves can be explained in a similar way as for sound radiation. If the porosity is $\Omega = 0.5$ and $f = (2j+1)c_0/2L$ with $j = 0, 1, 2, \ldots$, the pressure forces at both sides of the panel are such that the nett load on the panel is zero. This means that the panel is not vibrating and no sound is transmitted. For the panels with tubes, the transmission loss curves of a panel with a porosity of $\Omega$ and a panel with a porosity of $1 - \Omega$ are the same. For the sandwich panels, these curves are different (see Figure 2.22(b)).

A system is called acoustic reciprocal if the acoustic response remains the same when source and receiver are interchanged. In Appendix B it is shown that, in the absence of viscothermal effects, the models of both a characteristic area of a panel with tubes and of a sandwich panel are reciprocal. This also means that, if the conditions at both sides of the panel are the same, the orientation of the panel does not influence the amount of sound which is transmitted through the panel, i.e. it does not matter whether the resonator

openings are located at the incident side or at the receiving side.

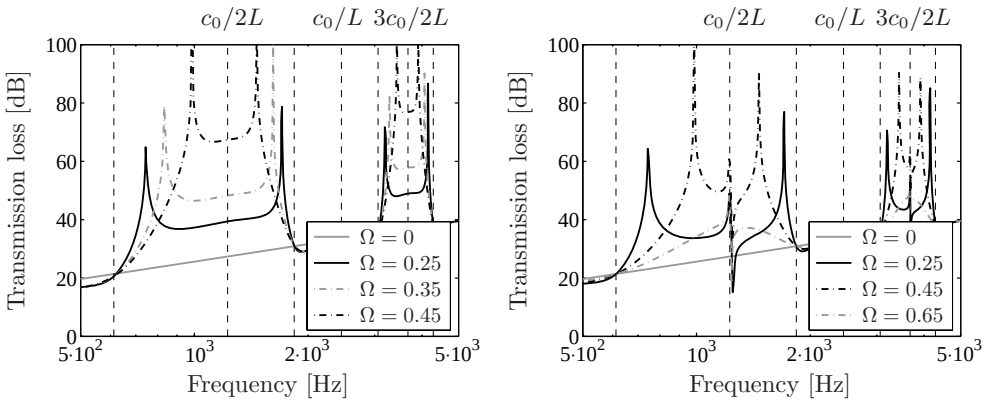


(a) Panel with tubes.

(b) Sandwich panel.

**Figure 2.22**: Transmission loss for different porosities ($L = 0.14$ m, $\bar{m} = 2.5$ kg/m$^2$).

### Viscothermal effects

Figures 2.23 and 2.24 show the influence of the viscothermal effects on the sound transmission loss. The results are shown both for a characteristic area of a panel with tubes and of a sandwich panel. The porosity is kept constant at $\Omega = 0.45$, while the resonator radius is varied. The trends that are seen are similar to those observed for the radiation of sound in Section 2.3.1. The mass of the panel determines the structural velocity of the panel. This means that the mass also influences the amount of viscous effects that are introduced by the vibration of the walls of the resonators. The amount of viscous effects in turn influence the structural velocity of the panel again.

In Appendix B it is shown that if viscothermal effects are present, the system is no longer reciprocal. This means that the acoustic response changes when source and receiver are interchanged. This is also seen in Figures 2.23 and 2.24.

## 2.5 Experimental validation

The model for sound radiation as described in Section 2.3.1, as well as the low reduced frequency solution for a vibrating cylindrical tube as presented in Section 2.2.2, are validated by means of experiments in an impedance tube. In this section, the experiments and their results are discussed.

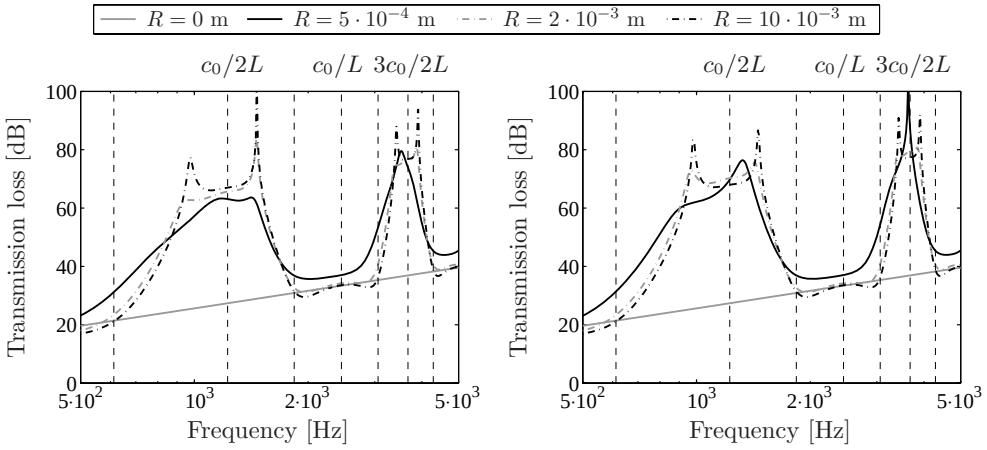


(a) Resonator openings at receiving side. (b) Resonator openings at incident side.

**Figure 2.23**: Transmission loss for different resonator radii - panel with tubes ($L = 0.14$ m, $\Omega = 0.45$, $\bar{m} = 2.5$ kg/m$^2$).

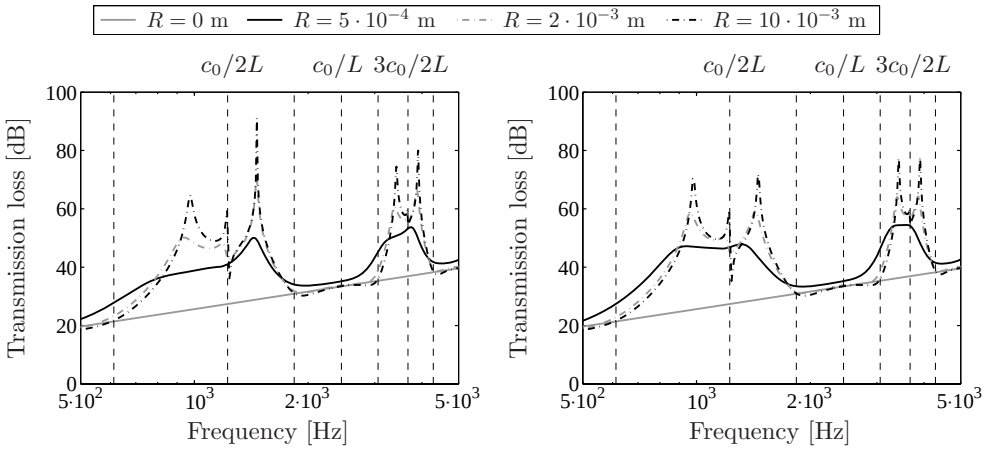


(a) Resonator openings at receiving side. (b) Resonator openings at incident side.

**Figure 2.24**: Transmission loss for different resonator radii - sandwich panel ($L = 0.14$ m, $\Omega = 0.45$, $\bar{m} = 2.5$ kg/m$^2$).

### Experimental setup and procedure

A schematic representation of the experimental setup is shown in Figure 2.25 [30, 51]. A sample with resonator was harmonically excited in an impedance tube by a shaker. The shaker was driven by a random signal, so that a

broadband sound field was generated. The sound pressures $p_{\mathrm{I}}$ and $p_{\mathrm{II}}$ were measured at two positions in the impedance tube and the excitation velocity $v_s$ was derived from the signal of an accelerometer which was attached to the sample. To make a comparison with the model, the transfer function $p_{\mathrm{I}}/v_s$ was determined. The end of the impedance tube was equipped with a baffle to give it a well-defined end condition. The dimensions of the experimental setup are listed in Table 2.1. Additional information on the measurement equipment is shown in Table 2.2.

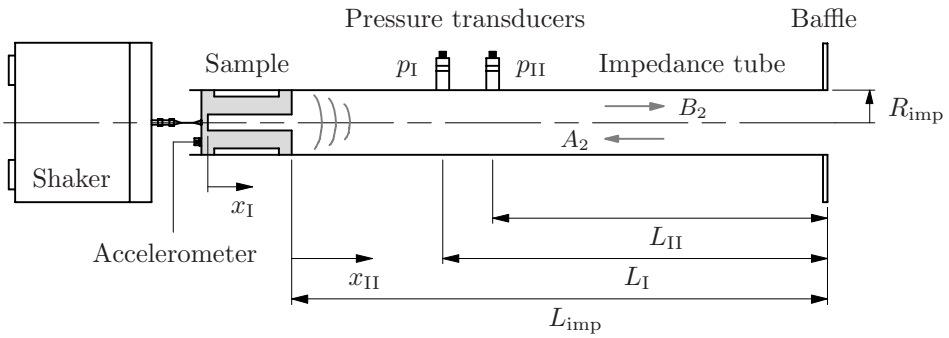


**Figure 2.25**: Experimental setup for measurement of sound radiation.

| **Dimensions** | |
|---|---|
| $R_{\mathrm{imp}}$ | 0.025 |
| $L_{\mathrm{I}}$ | 0.495 |
| $L_{\mathrm{II}}$ | 0.450 |

**Table 2.1**: Dimensions of the experimental setup [m].

### Model of the experimental setup

The difference between the experimental setup and the model described in Section 2.3.1 is that the impedance tube is not infinitely long. Therefore, sound is reflected at the end of the impedance tube. The pressure amplitude $A_2$ of the reflected sound waves is calculated by imposing an impedance condition at the end of the impedance tube. This boundary condition can be written as:

$$\frac{p_2|_{x_{\mathrm{II}}=L_{\mathrm{imp}}}}{v_2|_{x_{\mathrm{II}}=L_{\mathrm{imp}}}} = Z \tag{2.59}$$

| Description | Type | Remarks |
|---|---|---|
| Pressure transducers (2×) | Kulite XCS-190M-0.14 bar D | |
| Accelerometer | Brüel & Kjær (B&K) 4374 | |
| Shaker | B&K 4809 | |
| Pre-amplifier | Kulite D486 | For pressure transducers |
| Charge amplifier | B&K 2626 | For accelerometer |
| Power amplifier | B&K 2706 | For shaker |
| Siglab | Model 20-42 | Data acquisition and generation of excitation signal |
| Personal computer | | |

**Table 2.2**: Measurement equipment for sound radiation measurements.

where $L_{\text{imp}}$ is the distance from the front of the sample to the end of the impedance tube. The impedance $Z$ at the end of the impedance tube was determined from the transfer function $H_{21} = p_{\text{II}}/p_{\text{I}}$ of the pressures measured by the two pressure transducers [11, 12]. Using equations (2.21) and (2.26) with $v_s = 0$, the relation between the impedance and the measured transfer function is found to be:

$$Z = -\rho_0 c_0 \frac{\Gamma_2 n_2}{\mathrm{i}\gamma} \frac{H_{21}\sinh(\Gamma_2 k L_{\text{I}}) - \sinh(\Gamma_2 k L_{\text{II}})}{H_{21}\cosh(\Gamma_2 k L_{\text{I}}) - \cosh(\Gamma_2 k L_{\text{II}})} \tag{2.60}$$

where $L_{\text{I}}$ and $L_{\text{II}}$ are the distances of the two pressure transducers to the end of the impedance tube. Though the influence is only small, the viscothermal effects in the impedance tube are also taken into account. By combining equation (2.59) with the other boundary conditions (2.38) to (2.40), the unknown pressure amplitudes $A_1$, $B_1$, $A_2$ and $B_2$ can be solved as a function of the excitation velocity $v_s$ and the transfer function $p_{\text{I}}/v_s$ can be calculated at the position of the first pressure transducer.

Due to inlet effects, the effective length of the resonator $L = L_{\text{phy}} + \delta$ is slightly larger than the physical length $L_{\text{phy}}$ of the resonator (see also Section 3.2). For a tube centrally located in another tube, the end correction $\delta$ is given by [8]:

$$\delta = \frac{8R}{3\pi}\left[1 - 1.25\frac{R}{R_{\text{imp}}}\right], \qquad \text{with} \quad \frac{R}{R_{\text{imp}}} < 0.6 \tag{2.61}$$

### Samples

Figures 2.26(a), 2.26(b) and 2.26(c) show the three samples with resonators that were tested: two rigid aluminium samples and one sample with an aluminium tube that was used for the resonator panel as presented in Chapter 5. The dimensions of the resonators, as well as the distances from the fronts of the samples to the end of the impedance tube, are listed in Table 2.3. The radius of sample 1 is chosen to be small enough to perceive the viscothermal effects and large enough to distinguish the influence of the resonator. The radius of sample 2 is such that a large reduction of the radiated sound power is obtained over a broad frequency range. For radiation to the far field, a reduction in sound power level of at least 15 dB is predicted in the frequency range of 1035-2045 Hz.

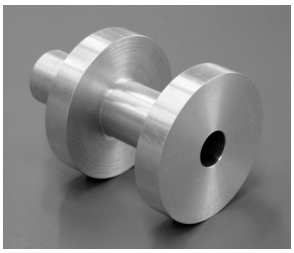

(a) Sample 1.

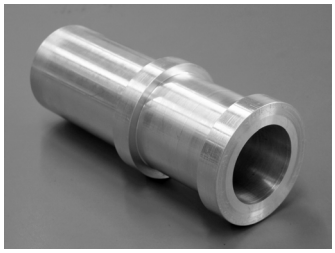

(b) Sample 2.

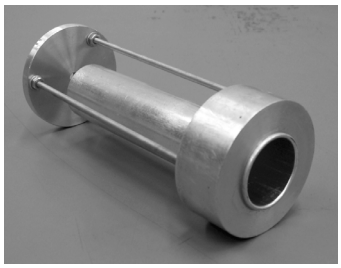

(c) Sample 3.

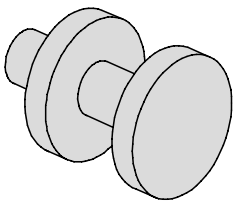

(d) Reference case (model).

**Figure 2.26**: Photos of the samples for experimental validation and a schematic representation of the reference case.

### Results

Figure 2.27 shows the results of the measurements on sample 1, compared with the analytical results. It can be seen that there is an excellent agreement be-

| | $L_{\text{phy}}$ [m] | $R$ [m] | $\Omega$ [-] | $L_{\text{imp}}$ [m] |
|---|---|---|---|---|
| Sample 1 | 0.0615 | 0.0060 | 0.06 | 0.663 |
| Sample 2 | 0.1112 | 0.0161 | 0.41 | 0.640 |
| Sample 3 | 0.1090 | 0.0122 | 0.24 | 0.650 |

**Table 2.3**: Dimensions of the samples and experimental setup for validation.

tween model and measurement. To show the reduction in radiated sound, the calculated transfer function of a rigid piston (i.e. a characteristic area without resonator - see Figure 2.26(d)) is plotted as a reference. If the magnitude of the transfer function of the sample is lower than the transfer function of the piston, the radiated sound is reduced. The peaks in the transfer functions are caused by resonances in the impedance tube.

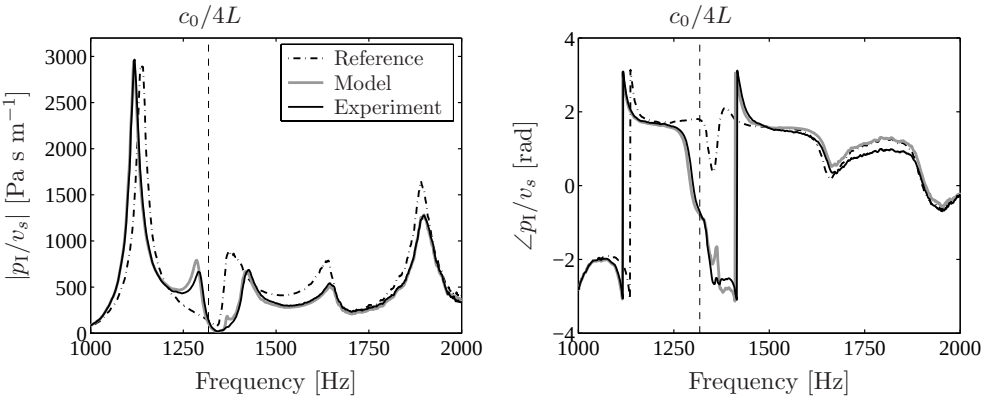


(a) Magnitude. (b) Phase.

**Figure 2.27**: Magnitude and phase of calculated and measured transfer functions $p_I/v_s$ for sample 1.

The results of the measurements on sample 2 are shown in Figure 2.28. It can be seen that there is a fairly good agreement between model and measurement. The discrepancies that are observed are mainly caused by the fact that the sound pressures are so small here that they approximate the noise floor of the pressure transducers. This makes the measurements less accurate. Furthermore, it should be noted that Bolt [8] proved that the end correction defined by equation (2.61) is valid for $R/R_{\text{imp}} < 0.6$. However, for sample 2 the ratio of the resonator radius and the radius of the impedance tube equals 0.64. The reason that the transfer function of the reference differs from the transfer function of the reference in Figure 2.27 is that the distance $L_{\text{imp}}$ from

the front of the sample to the end of the impedance tube was different for the two experiments (see Table 2.3).

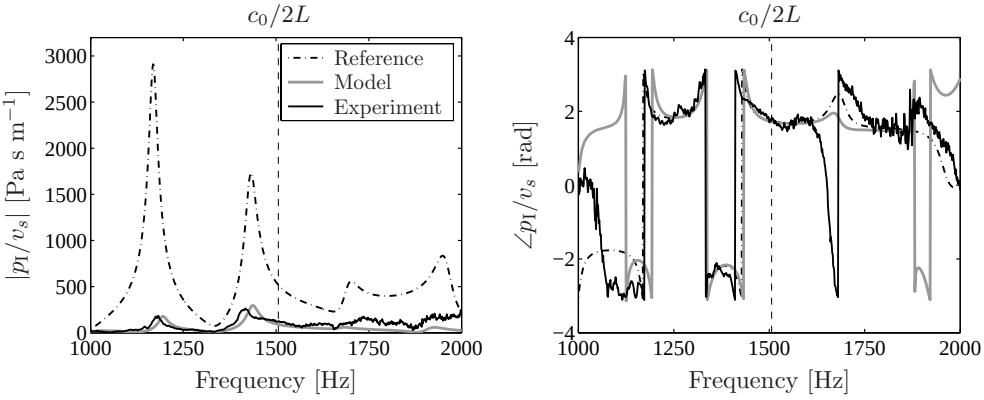


(a) Magnitude. (b) Phase.

**Figure 2.28**: Magnitude and phase of calculated and measured transfer functions $p_\mathrm{I}/v_s$ for sample 2.

Figure 2.29 shows the results of the measurements on sample 3, compared with the analytical results. Excellent agreement is obtained up to 2000 Hz. Possible deformations of the thin wall or end of the resonator can explain the discrepancies above 2000 Hz. Further discussions on this can be found in the next chapters.

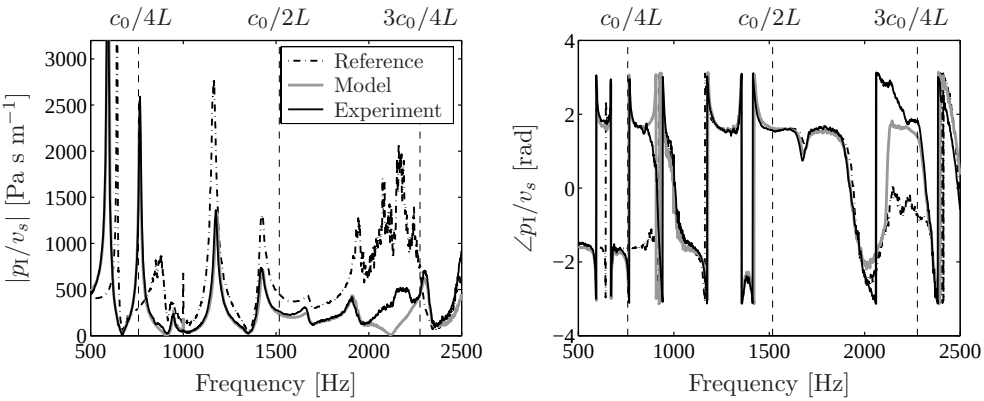


(a) Magnitude. (b) Phase.

**Figure 2.29**: Magnitude and phase of calculated and measured transfer functions $p_\mathrm{I}/v_s$ for sample 3.

## 2.6 Concluding remarks

In this chapter, one-dimensional analytical models were presented to study the radiation of sound by and the transmission of sound through panels with tube resonators. To describe the viscothermal wave propagation inside and around the resonators, the low reduced frequency model was used. Solutions were derived for axially vibrating cylindrical tubes and layers.

Simulations showed that, by the application of tube resonators, the radiated or transmitted sound can be reduced considerably over a broad frequency range. The length of the resonators determines the centre frequency of the range in which the sound is reduced and the porosity determines the shape of the spectrum. Furthermore, it was seen that viscothermal effects increase the reductions at lower frequencies, decrease the amplifications, but also decrease the reductions around the centre frequency. To validate the models for sound radiation, experiments were performed in an impedance tube. Generally, good agreement was obtained between model and measurements.

As mentioned in Chapter 1, tube resonators are well known for their sound absorption applications. In this chapter it was demonstrated that the working principle of the resonators for the reduction of radiated or transmitted sound is quite different. If no viscothermal effects are present, sound absorption only occurs at those frequencies at which the air inside the resonators is in resonance. These frequencies are the frequencies for which a quarter, and odd multiples of a quarter, of the acoustic wavelength is equal to the length of the resonator. In the case of sound radiation or sound transmission, the centre frequency of the frequency range in which the sound is reduced is the frequency for which a half, and odd multiples of a half, of the acoustic wavelength is equal to the length of the resonator. The frequencies for which sound reduction is maximal are not only related to the length of the resonators, but also depend on the porosity of the panel.

# Chapter 3

# Two-dimensional modelling

## 3.1 Introduction

In the previous chapter, one-dimensional analytical models were presented to study the transmission of normal incident sound through panels with resonators. The panels were assumed to be rigid and infinitely large. However, in practice, sound is incident from many different directions, the panel is flexible, and its dimensions are finite. Furthermore, the discontinuity of the surface of the structure, introduced by the presence of resonators, may cause scattering of the incident and transmitted sound fields. In this chapter, two two-dimensional models are presented, which are used to investigate the influence of the aforementioned aspects.

In Section 3.2, the influence of scattering by the resonator openings on sound radiation and normal incidence sound transmission is considered. The sound fields at both sides of the panel are described by a two-dimensional analytical model. As in Chapter 2, the panel is again assumed to be rigid and infinitely large. Because of the periodicity of the structure, the scattered sound fields can be expressed as a series of spatial Fourier harmonics.

In Section 3.3, the transmission of sound through a panel with resonators is modelled using the finite element method (FEM). A two-dimensional model of a panel mounted between two rooms is considered. The difference with the previously presented models is that the sound is random incident and the panel is bounded and flexible now. The effects of these conditions are demonstrated by means of a parameter study.

The models presented in this chapter only consider the tube panel configuration (see Figure 2.1). Moreover, no viscothermal effects are taken into account.

## 3.2 Two-dimensional semi-analytical model

Figure 3.1 shows the transmission of a normal incident plane sound wave through a rigid panel with resonators. When the sound wave impinges on the panel, the sound is scattered by the resonators in the structure. Depending on the ratio of the width $b$ of the characteristic areas and the acoustic wavelength $\lambda$, these waves are either plane waves radiating into the far field or evanescent surface waves. The sound wave which is reflected in the direction opposite to that of the incident wave is the so-called specular reflection.

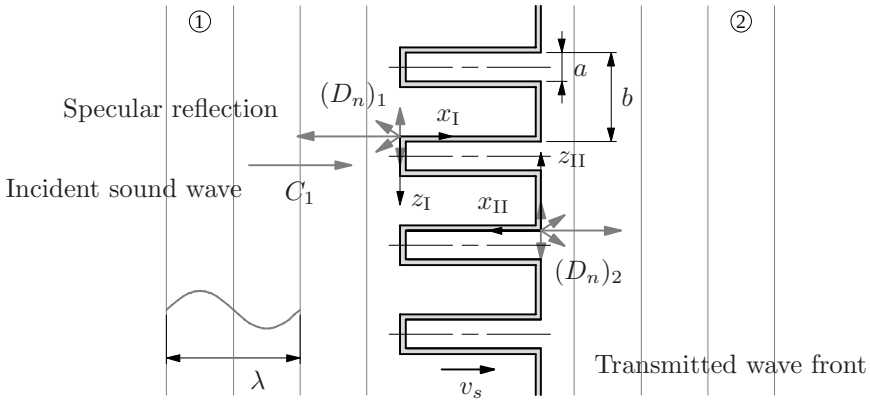


**Figure 3.1**: Transmission of a normal incident plane wave through an infinitely large, rigid panel with resonators.

Since the structure is periodic, and assumed here to be infinitely large, the sound fields at both sides of the panel can be expressed as a series of spatial Fourier harmonics. Mechel [36] used the same formulation to investigate the performance of periodic absorbers. Besides the absorption characteristics of different periodic structures, he also considered the transmission of sound through perforated plates into porous absorption material. The difference between the model presented in this section and the cases investigated by Mechel is that in the present work the rigid structure is vibrating. This means that there is an interaction between the velocity of the structure and the fluid velocities in the sound fields.

The model presented by Mechel was also used to demonstrate the influence of the angle of incidence of an obliquely incident plane wave on the absorption characteristics of a structure. However, when considering sound transmission through a rigid panel, obliquely incident plane waves are not transmitted. An explanation for this can be found in Figure 3.2. Sound impinging on a flexible panel, introduces bending waves in that panel, which make the panel radiate

sound to the other side. In the case of a rigid panel, no deformations are induced, so sound can only be transmitted by the movement of the panel as a whole. In the case of normal incidence, this happens because the excitation pressure is the same at any position on the surface. However, when the angle of incidence is oblique, the excitation pressure varies spatially over the panel surface and the integral of the pressure load is zero (see Figure 3.2). This means that in this situation the panel does not move and no sound is transmitted. The model that is presented here therefore only describes the transmission of normal incident plane waves.

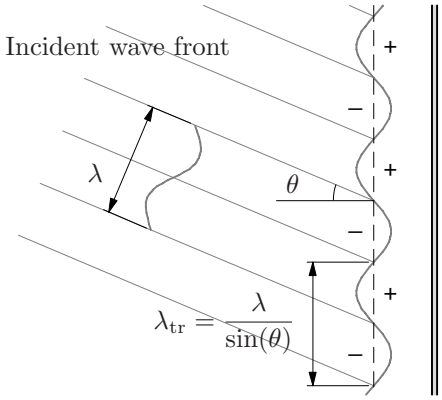


**Figure 3.2**: Obliquely incident sound field on an infinitely large, rigid panel without resonators.

In Section 3.2.1, the formulation of the two-dimensional sound fields at both sides of the panel is presented. Expressions are derived for the pressure and the fluid velocity in the direction normal to the panel. Subsequently, the model for sound transmission is composed by coupling the two two-dimensional sound fields to the sound fields inside and around[1] the resonators. The latter sound fields are described by the one-dimensional analytical models as presented in Chapter 2. The model for sound radiation is then derived from the model for sound transmission. Finally, the influence of scattering by the resonator openings on sound radiation and sound transmission is demonstrated.

[1]In this section, the air volumes with the opening at the receiving side are referred to as air *inside* the resonators and the air volumes with the opening at the incident side are referred to as air *around* the resonators.

### 3.2.1 Two-dimensional sound fields

For the two sound fields at both sides of the panel (see Figure 3.1), a similar two-dimensional formulation can be used. The incident sound field is composed of a normal incident plane sound wave and its reflection on the surface. The formulation of the radiated sound field at the receiving side is similar to that of the reflected part at the incident side. The general expressions for the pressure and the fluid velocity are defined in the $x$, $z$-plane. Later on, subscript I will be used for the incident side and subscript II for the receiving side (see Figure 3.1).

Assuming harmonic time dependence, the two-dimensional pressure field can be written as [36]:

$$p(x,z) = Ce^{-\mathrm{i}kx} + \sum_{n=-\infty}^{\infty} D_n e^{\gamma_n x} e^{-\mathrm{i}\beta_n z} \tag{3.1}$$

The first term represents an incident sound wave with amplitude $C$ and the second term is the general formulation of a scattered sound field with amplitudes $D_n$. The latter components are the so-called spatial harmonics, where the component $n = 0$ is the specular reflection. The coefficients $\beta_n$ and $\gamma_n$ are related by the fact that the pressure has to satisfy the wave equation. For a two-dimensional sound field and harmonic time dependence, the wave equation is given by:

$$\frac{\partial^2 p}{\partial x^2} + \frac{\partial^2 p}{\partial z^2} + k^2 p = 0 \tag{3.2}$$

For the pressure field as defined by equation (3.1), this equation is only satisfied if:

$$\gamma_n^2 = \beta_n^2 - k^2 \tag{3.3}$$

Since the structure is periodic in $z$ with period $b$, the pressure at the surface must be periodic in the same way. This is satisfied if:

$$\beta_n = n2\pi/b \qquad \text{with} \qquad n = 0, \pm 1, \pm 2, \ldots \tag{3.4}$$

where $b$ is the width of the characteristic area. With equation (3.3), the expression for $\gamma_n$ becomes:

$$\gamma_n = k\sqrt{(n\lambda/b)^2 - 1} \qquad \text{with} \qquad n = 0, \pm 1, \pm 2, \ldots \tag{3.5}$$

where $\lambda = c_0/f$ is the free-field wavelength. The pressure field can now be written as:

$$p(x,z) = \left\{ Ce^{-\mathrm{i}kx} + \sum_{n=-\infty}^{\infty} D_n e^{kx\sqrt{(n\lambda/b)^2-1}} e^{-\mathrm{i}n2\pi z/b} \right\} \tag{3.6}$$

At the incident side, the pressure amplitude $C$ is prescribed. At the receiving side, no incident sound wave is assumed to be present, so $C = 0$. The pressure amplitudes $D_n$ at both sides of the panel are determined by the boundary conditions at the surface ($x_{\mathrm{I}} = 0$, $x_{\mathrm{II}} = 0$). Depending on whether the radicand in the exponent of the sum terms is positive or negative, the corresponding harmonics are either evanescent surface waves or plane waves which radiate into the far field. Only the latter components contribute to the radiated sound power. The radicand in the exponent of the sum terms is negative, and thus the spatial harmonics are radiating if:

$$-\frac{b}{\lambda} \leq n \leq \frac{b}{\lambda} \tag{3.7}$$

For the acoustic wavelengths and the widths of the characteristic areas that are considered in this thesis, i.e. $b/\lambda < 1$, this implies that only the component $n = 0$ contributes to the radiated sound power. In fact, this would mean that other components could be omitted. However, to satisfy the boundary conditions described in the next section and to obtain an accurate solution for the pressure amplitude $D_0$, a certain number of components $n \neq 0$ still has to be taken into account.

To determine the sound power through a surface parallel to the panel, the fluid velocity $v$ in $x$-direction also has to be known. This fluid velocity is related to the pressure by Euler's equation of motion, which is given by:

$$-\rho_0 \frac{\partial \tilde{v}(x,z)}{\partial t} = \frac{\partial \tilde{p}(x,z)}{\partial x} \tag{3.8}$$

Harmonic expansion yields:

$$v(x,z) = \frac{\mathrm{i}}{\rho_0 \omega} \frac{\partial p(x,z)}{\partial x} \tag{3.9}$$

With equation (3.6), the fluid velocity in $x$-direction can then be written as:

$$v(x,z) = \frac{1}{\rho_0 c_0} \left[ C e^{-\mathrm{i}kx} + \mathrm{i} \sum_{n=-\infty}^{\infty} D_n \sqrt{(n\lambda/b)^2 - 1} e^{kx\sqrt{(n\lambda/b)^2-1}} e^{-\mathrm{i}n2\pi z/b} \right] \tag{3.10}$$

### 3.2.2 Sound radiation and transmission

#### Sound transmission

In accordance with the one-dimensional model presented in Section 2.3.2, the model for sound transmission consists of four parts. A schematic overview

of this is shown in Figure 3.3. The sound fields at the incident side and the receiving side of the panel are described by the two-dimensional analytical models as presented in the previous section. The pressures $p_1$ and $p_2$ and the fluid velocities $v_1$ and $v_2$ at these sides are given by equations (3.6) and (3.10), respectively. The sound fields inside and around the resonators are described by the one-dimensional analytical models as presented in Section 2.2. If no viscothermal effects are taken into account, the pressures $p_3$ and $p_4$ and fluid velocities $v_3$ and $v_4$ in these two parts can be written as:

$$p_j(x) = A_j e^{\mathrm{i}kx} + B_j e^{-\mathrm{i}kx} \qquad j = 3, 4 \tag{3.11}$$

$$v_j(x) = -\frac{1}{\rho_0 c_0}\left(A_j e^{\mathrm{i}kx} - B_j e^{-\mathrm{i}kx}\right) \qquad j = 3, 4 \tag{3.12}$$

The sound fields ① and ③ at the incident side are defined with respect to coordinates $x_\mathrm{I}$ and $z_\mathrm{I}$ and the sound fields ② and ④ at the receiving side are defined with respect to coordinates $x_\mathrm{II}$ and $z_\mathrm{II}$ (see Figure 3.3). The unknown pressure amplitudes $(D_n)_1$, $A_3$, $B_3$, $(D_n)_2$, $A_4$ and $B_4$ and the structural velocity $v_s$ are determined by the boundary conditions of the system and the equation of motion. These boundary conditions describe both the coupling between the different sound fields and the coupling between the sound fields and the structure.

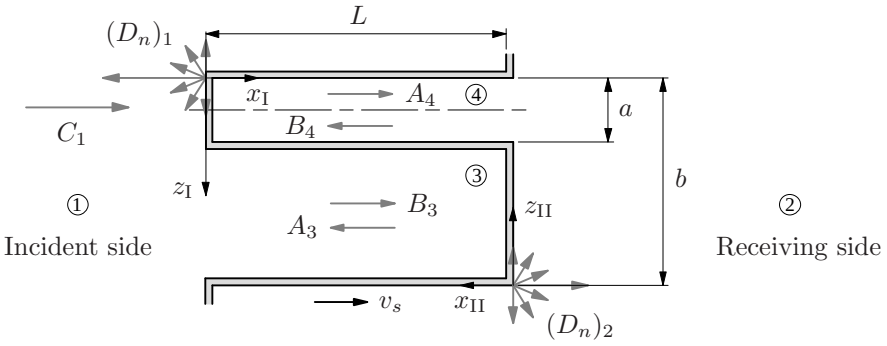


**Figure 3.3**: Transmission of a normal incident plane wave through an infinitely large, rigid panel with resonators.

### Boundary conditions

At the incident side of the panel three boundary conditions have to be satisfied. The first boundary condition states that the fluid velocity in $x_\mathrm{I}$-direction is continuous at the surface $x_\mathrm{I} = 0$. This implies that at the end of the resonator

the fluid velocity $v_1$ is equal to the structural velocity $v_s$ and in the opening around the resonator the fluid velocity $v_1$ is equal to the fluid velocity $v_3$. Because the set of equations does not have a closed-form solution, it is written in a weak form by multiplying the velocities by weighting functions $w(z_\mathrm{I})$ and integrating over $z_\mathrm{I}$:

$$\int_0^b w(z_\mathrm{I})\; v_1(z_\mathrm{I})|_{x_\mathrm{I}=0}\; \mathrm{d}z_\mathrm{I} \;=\; v_s \int_0^a w(z_\mathrm{I})\,\mathrm{d}z_\mathrm{I} \;+\; v_3|_{x_\mathrm{I}=0} \int_a^b w(z_\mathrm{I})\,\mathrm{d}z_\mathrm{I} \tag{3.13}$$

where $a$ is the resonator diameter. Since no viscothermal effects are taken into account, the velocity profiles inside and around the resonators are flat, so the fluid velocities $v_3$ and $v_4$ are independent of $z_\mathrm{I}$ and $z_\mathrm{II}$, respectively. The weighting functions are chosen to be:

$$w(z) = e^{\mathrm{i}q2\pi z/b} \qquad \text{with} \qquad q = 0, \pm 1, \pm 2, \ldots \tag{3.14}$$

The second boundary condition states that the pressure in the opening around the resonator is continuous. This pressure condition is written as:

$$\int_a^b p_1(z_\mathrm{I})|_{x_\mathrm{I}=0}\; \mathrm{d}z_\mathrm{I} \;=\; p_3|_{x_\mathrm{I}=0}\; [b-a] \tag{3.15}$$

Since the pressures $p_3$ and $p_4$ inside and around the resonators are independent of $z_\mathrm{I}$ and $z_\mathrm{II}$, this means that the condition is only satisfied in an average sense. The third boundary condition requires that the fluid velocity $v_3$ at the panel surface is equal to the structural velocity:

$$v_3|_{x_\mathrm{I}=L} \;=\; v_s \tag{3.16}$$

At the receiving side similar boundary conditions have to be satisfied, which can be written as:

$$\int_0^b w(z_\mathrm{II})\; v_2(z_\mathrm{II})|_{x_\mathrm{II}=0}\; \mathrm{d}z_\mathrm{II} \;=\; -\,v_s \int_0^{b-a} w(z_\mathrm{II})\,\mathrm{d}z_\mathrm{II} \;+\; v_4|_{x_\mathrm{II}=0} \int_{b-a}^b w(z_\mathrm{II})\,\mathrm{d}z_\mathrm{II} \tag{3.17}$$

$$\int_{b-a}^b p_2(z_\mathrm{II})|_{x_\mathrm{II}=0}\; \mathrm{d}z_\mathrm{II} \;=\; p_4|_{x_\mathrm{II}=0}\; a \tag{3.18}$$

$$v_4|_{x_\mathrm{II}=L} \;=\; -\,v_s \tag{3.19}$$

Furthermore, the equation of motion of the entire system is given by:

$$\int_0^a p_1(z_\mathrm{I})|_{x_\mathrm{I}=0}\; \mathrm{d}z_\mathrm{I} + p_3|_{x_\mathrm{I}=L}\; [b-a] - p_4|_{x_\mathrm{II}=L}\; a - \int_0^{b-a} p_2(z_\mathrm{II})|_{x_\mathrm{II}=0}\; \mathrm{d}z_\mathrm{II} = m\mathrm{i}\omega v_s \tag{3.20}$$

By applying these boundary conditions to equations (3.6), (3.10), (3.11) and (3.12), the unknown pressure amplitudes and the structural velocity can be solved for a given amplitude $C_1$ of the incident sound wave.

**Sound transmission loss**

As mentioned in Section 2.4.2, the transmission coefficient is defined as the ratio of the transmitted sound power $\bar{W}_t$ and the incident sound power $\bar{W}_i$:

$$\tau = \frac{\bar{W}_t}{\bar{W}_i} \tag{3.21}$$

Both sound powers are calculated with equations (2.50) and (2.51), where the sound intensities at $x_{\mathrm{I}} = 0$ and $x_{\mathrm{II}} = 0$, respectively, are integrated over the width of one characteristic area. For the incident sound power this yields:

$$\bar{W}_i = \frac{b|C_1|^2}{2\rho c_0} \tag{3.22}$$

With the expression for the transmission coefficient, the sound transmission loss is calculated with equation (2.57).

**Sound radiation**

In the case of sound radiation, only the receiving side of the panel is considered (see Figure 3.3). The rigid panel is assumed to vibrate harmonically in normal direction with a given normal structural velocity $v_s$ and the radiated sound field can be determined by solving the unknown pressure amplitudes $(D_n)_2$, $A_4$ and $B_4$ from the system of equations formed by boundary conditions (3.17) to (3.19). The radiated sound power is calculated with equations (2.50) and (2.51), integrating the sound intensity at $x_{\mathrm{II}} = 0$ over the width of one characteristic area. Finally, the insertion loss is calculated with equation (2.48).

### 3.2.3 Parameter study

This section demonstrates the influence of scattering by the resonator openings on the sound radiation by and sound transmission through an infinitely large, rigid panel with resonators.

**Sound radiation**

Figure 3.4(a) shows the insertion loss of various configurations with the same porosity[2] but different values of the resonator diameters $a$ and widths $b$ of the characteristic areas. For accurate solutions, the system was truncated at

[2]The porosity is defined here as $\Omega = a/b$ (see Figure 3.3).

$n = \pm 20$. Comparison with the results obtained with the one-dimensional analytical model (without viscothermal effects) as presented in Chapter 2 shows that when the dimensions of the resonators and characteristic areas increase, the effects of scattering also increase. Consequently, the peaks of the insertion loss curves shift to lower frequencies. An explanation for this can be found in the fact that scattering by the resonator openings causes inlet effects, which make the effective length of the resonators a little longer than the physical length. These inlet effects are clearly visible in Figure 3.5, where the pressure and the sound intensity of the radiated sound field are plotted at an arbitrary frequency. In accordance with the observations in Section 2.5, the effective length changes for different values of the resonator diameters and widths of the characteristic areas.

In Figure 3.5(b) it can be seen that the sound intensity at the panel surface is in the direction away from the surface[3]. The sound intensity at the resonator opening is in the opposite direction, into the resonator. Since these sources partly cancel each other out, the sound intensity at a small distance from the panel is lower than at the panel surface, which means that the radiated sound is reduced.

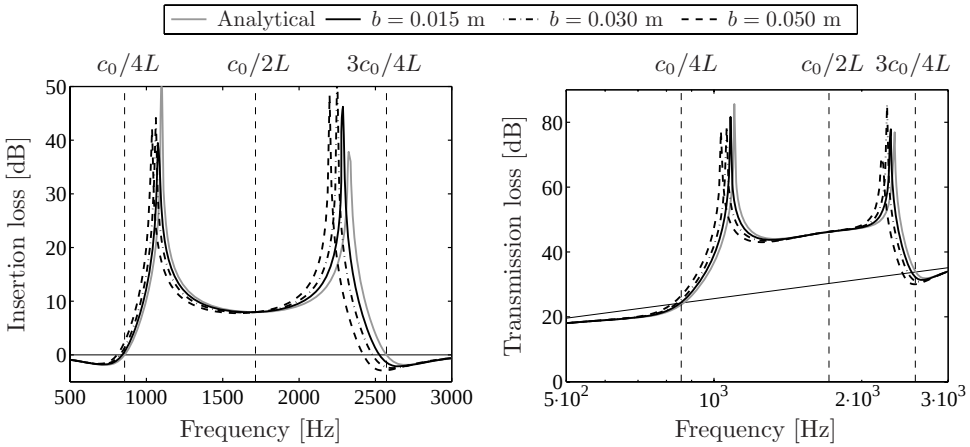


(a) Sound radiation. (b) Sound transmission.

**Figure 3.4**: Insertion loss and normal incidence transmission loss for different resonator radii and widths of the characteristic areas ($L = 0.1$ m, $\Omega = 0.3$, $\bar{m} = 2.5$ kg/m).

[3]Note that the positive directions of $x_{\mathrm{II}}$ and thus $\bar{I}_2$ are into the resonator.

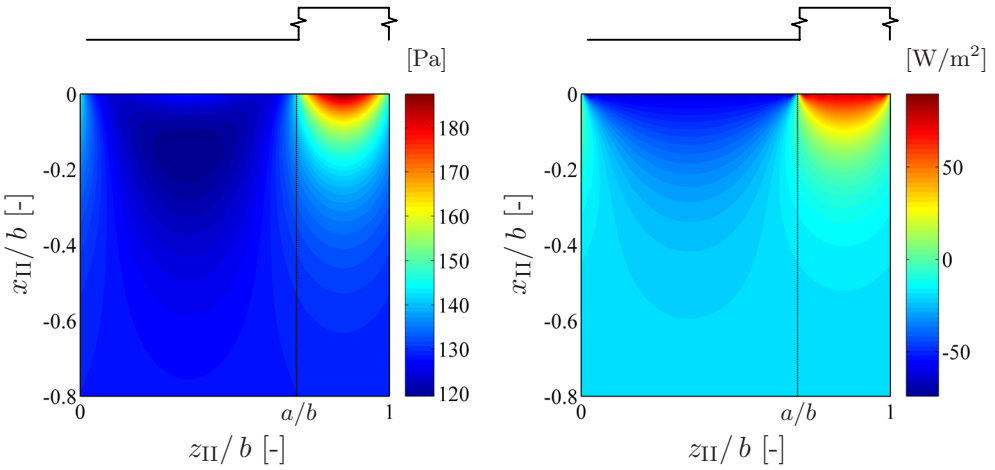


(a) Magnitude of pressure $p_2$.

(b) Sound intensity $\bar{I}_2$.

**Figure 3.5**: Magnitude of pressure $p_2$ and sound intensity $\bar{I}_2$ in normal direction over one characteristic area at 2000 Hz ($L = 0.1$ m, $b = 0.03$ m, $\Omega = 0.3$, $v_s = 1$ m/s).

### Normal incidence sound transmission

Figure 3.4(b) shows the normal incidence transmission loss of various panels with the same porosity but different values of the resonator diameters $a$ and widths $b$ of the characteristic areas. For accurate solutions, the system was truncated at $n = \pm 20$. The conclusions that can be drawn by comparison with the one-dimensional analytical model are the same as in the case of sound radiation discussed above.

## 3.3 Finite element model

Another way of modelling the transmission of sound through a panel with resonators is by using the finite element method (FEM). With this method, the transmission of non-normal incident sound can also be considered. Moreover, the flexibility and boundedness of the panel can be taken into account.

In this section, a two-dimensional FEM model is used to study the transmission of sound through a panel with resonators mounted between two rooms. A schematic representation of the setup is shown in Figure 3.6. In one room, a sound source is located at an arbitrary position and in the other room, the transmitted sound power is calculated. The first room has three acoustically hard walls, whereas in the other room one or more walls are fully sound ab-

sorbing and the remaining walls are acoustically hard. The panel is simply supported.

The degrees of freedom (DOF) of an acoustic FEM model are the total pressures at the nodes. Because of this, it is not straightforward to make a distinction between incident sound waves and reflected sound waves. This also means that, using this method, it is not straightforward to model obliquely incident plane sound waves at specific angles of incidence. In this work, therefore, only random incident sound transmission is considered.

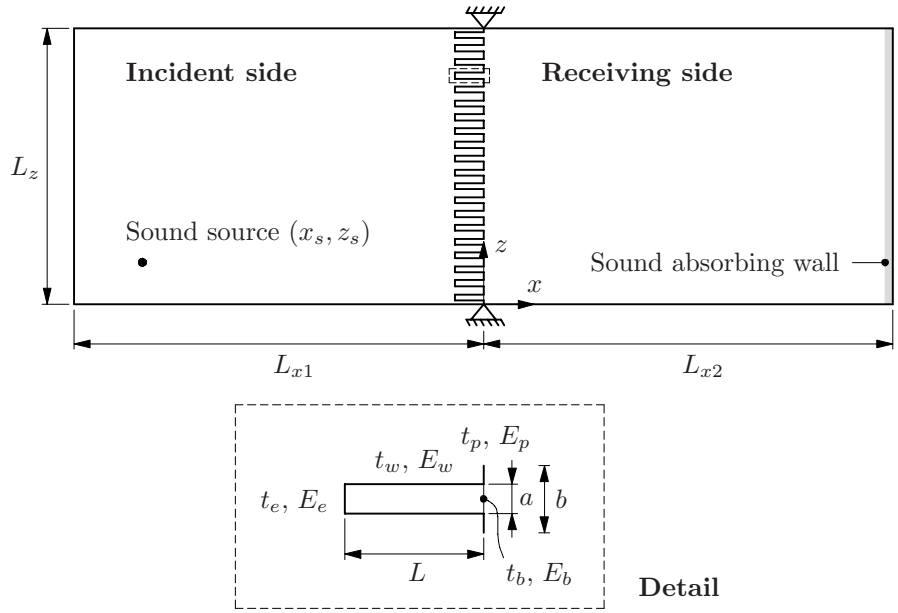


**Figure 3.6**: Simply supported panel with resonators between two rooms.

### 3.3.1 Sound transmission

The setup as shown in Figure 3.6 was modelled using the commercial FEM program ANSYS. The panel with resonators consists of 20 characteristic areas, with dimensions and material properties as listed in Table 3.1. $t_p$, $t_w$ and $t_e$ are the thicknesses of the plate and the walls and ends of the resonators, respectively. The entire structure was meshed with two-node beam elements (BEAM3). In reality, the tube resonators are cylindrical, so the stiffness of the walls and ends of the resonators is much higher than those of the beam elements if the actual Young's modulus were to be applied. In the FEM model, the additional stiffness of these parts was therefore simulated using a Young's

modulus of $E_w = E_e = 1000E$. To increase the stiffness of the plate, additional stiffness was also introduced at the entrance of the resonators. Extra beam elements of thickness $t_b$ and Young's modulus $E_b = E$ were applied across the resonator openings (see Figure 3.6). For the plate, a Young's modulus of $E_p = E$ was used. In the parameter study in the next section, the value of $E$ is varied.

| **Characteristic area** | | |
|---|---|---|
| $b$ | 0.03 | m |
| $a$ | 0.012 | m |
| $L$ | 0.11 | m |
| $t_p$ | 0.002 | m |
| $t_w$ | 0.0003 | m |
| $t_e$ | 0.0006 | m |
| $t_b$ | 0.002 | m |

| **Material** | | |
|---|---|---|
| $\rho$ | 2710 | kg/m$^3$ |
| $\nu$ | 0.3 | - |

**Table 3.1**: Dimensions and material properties of the panel.

The air at both sides of the panel was meshed with linear four-node fluid elements (FLUID29). A part of the FEM mesh around the structure is shown in Figure 3.7. At the interface, the structural mesh and the mesh of the air were coincident and full coupling was present. Only the additional beam elements across the resonator openings were not coupled to the air. The dimensions of the rooms and the position of the sound source are listed in Table 3.2. Both rooms were modelled with 100 fluid elements in the $x$-direction. The sound source in the room at the left-hand side of the panel was defined by prescribing a volume flow at one node. The sound absorbing wall(s) in the receiving room was/were modelled by prescribing a dimensionless impedance of one.

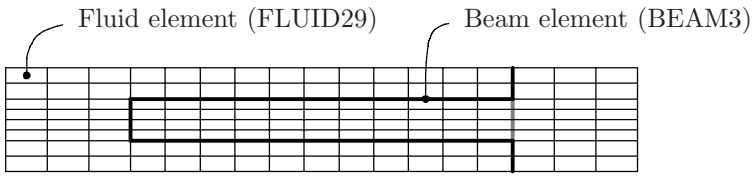


**Figure 3.7**: FEM mesh of part of the structure with the surrounding air.

### Sound transmission loss

To determine the sound transmission loss, the incident sound power has to be known. However, as mentioned before, in a FEM model it is not straightfor-

| Room dimensions | | |
|---|---|---|
| $L_{x1}$ | 1.2+L | m |
| $L_{x2}$ | 1.2 | m |
| $L_z$ | 0.6 | m |

| Source position | | |
|---|---|---|
| $x_s$ | -1.0-L | m |
| $z_s$ | 3b | m |

**Table 3.2**: Dimensions of the two rooms and source positions and strengths.

ward to make a distinction between incident sound waves and reflected sound waves. Usually, in the case of plane wave excitation and a fully reflective surface, the incident part of the pressure on the panel can be approximated by half the total pressure [20]. However, in the case of a panel with resonators, the reflection coefficient is not equal to one. In this work, therefore, an alternative approach is used.

The estimation is based on the assumption of a one-dimensional sound field between two closely spaced points. As a first step, the pressures $p_{\mathrm{I}}$ and $p_{\mathrm{II}}$ are determined at two closely spaced nodes, located at $x = x_{\mathrm{I}}$ and $x = x_{\mathrm{II}}$, one element size apart (see Figure 3.8). Between these points, the pressures are assumed to be dependent on $x$ in the following way:

$$p(x) = Ae^{\mathrm{i}kx} + Be^{-\mathrm{i}kx} \tag{3.23}$$

The pressure amplitudes $A$ and $B$ can thus be written as a function of the pressures $p_{\mathrm{I}}$ and $p_{\mathrm{II}}$ and the $x$-coordinates of the two nodes:

$$A = \frac{\mathrm{i}\left(p_{\mathrm{II}}e^{-\mathrm{i}kx_{\mathrm{I}}} - p_{\mathrm{I}}e^{-\mathrm{i}kx_{\mathrm{II}}}\right)}{2\sin\left[k(x_{\mathrm{I}} - x_{\mathrm{II}})\right]} \qquad B = \frac{\mathrm{i}\left(p_{\mathrm{I}}e^{\mathrm{i}kx_{\mathrm{II}}} - p_{\mathrm{II}}e^{\mathrm{i}kx_{\mathrm{I}}}\right)}{2\sin\left[k(x_{\mathrm{I}} - x_{\mathrm{II}})\right]} \tag{3.24}$$

With the expression for $B$, the incident pressure and fluid velocity normal to the panel surface at point $x = (x_{\mathrm{I}} + x_{\mathrm{II}})/2$, respectively, are then obtained by:

$$p_i(x) = Be^{-\mathrm{i}kx} \tag{3.25}$$

$$v_i(x) = \frac{1}{\rho_0 c_0} Be^{-\mathrm{i}kx} \tag{3.26}$$

Subsequently, the incident sound intensity at this point is determined by equation (2.51). At the other side of the panel, the sound intensities are calculated using the pressures and fluid velocities resulting directly from the FEM analysis. The sound powers at both sides are obtained by integrating the sound intensities from 0 to $L_z$ over $z$ using the trapezoidal rule, in accordance with equation (2.50). Finally, the sound transmission loss is determined by equations (3.21) and (2.57).

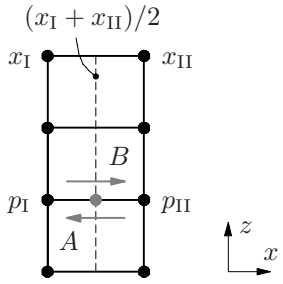


**Figure 3.8**: One-dimensional approach for determining the incident part of the sound power through the surface indicated by the dashed line.

### 3.3.2 Parameter study

In this section, the influence of different parameters on the sound transmission loss is presented. First, the influence of the flexibility of the plate and the resonators is studied. Second, the influence of two environmental parameters is considered: the position of the sound source and the number of sound absorbing walls in the receiving room. The basic parameters that were used in the model are listed in Tables 3.1 and 3.2.

#### Flexibility of the panel

The influence of the flexibility of the panel is examined by alternately changing the Young's modulus of the plate, the resonator walls and the resonator end. Two different values for the Young's modulus were applied: $E = 70{\cdot}10^9$ N/m$^2$, which is referred to as flexible, and $E = 70 \cdot 10^{12}$ N/m$^2$, which is referred to as stiff.

Figure 3.9(a) shows the sound transmission loss of an entirely stiff panel with resonators. Apart from the additional peaks and troughs, the transmission loss curve reasonably resembles the results predicted by the one-dimensional analytical model presented in Chapter 2. Most of the peaks and troughs are caused by acoustic resonances in the room at the incident side, which start occurring from 135 Hz. The shapes of the acoustic modes that cause the first two peaks in the sound transmission loss curve are shown in Figure 3.10. It is also seen that the structural eigenfrequencies of the panel, indicated by the rectangular boxes in Figure 3.9(a), have a negative effect on the sound transmission loss. The modes shapes associated with these frequencies are shown in Figure 3.11. For this panel, the structural resonances that occur in the frequency range of interest are only concerned with deformations of the plate; the resonators remain undeformed here. In Figure 3.9(a) the sound

transmission loss of a panel without resonators is also shown. This panel has the same mass, Young's modulus and Poisson's ratio, and was modelled in the same setup.

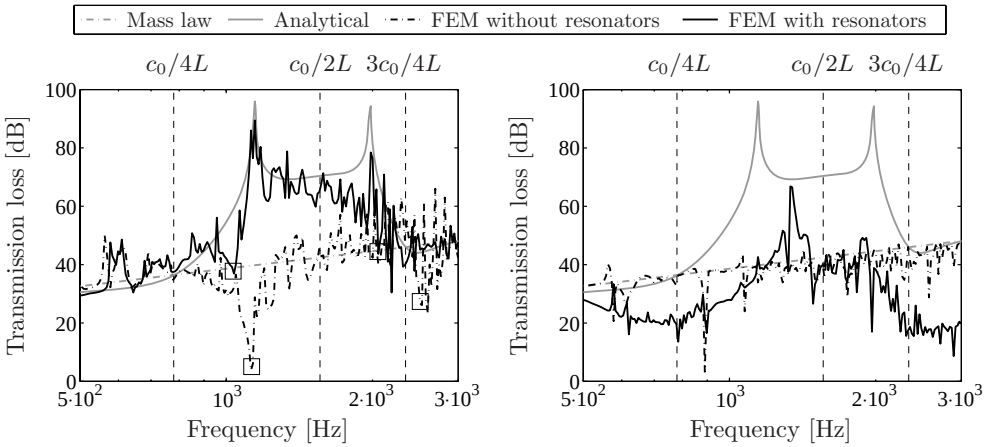


(a) Stiff panel. (b) Flexible panel.

**Figure 3.9**: Sound transmission loss of stiff and flexible panels, with and without resonators.

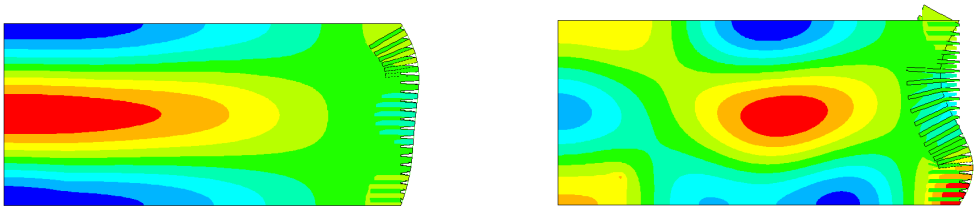

577 Hz 610 Hz

**Figure 3.10**: Acoustic mode shapes at the incident side of stiff panel with resonators at 577 Hz and 610 Hz.

In Figure 3.9(b), the sound transmission loss of an entirely flexible panel with and without resonators is shown. It can be seen that for the panel with resonators, the flexibility of the structure has a very large negative effect on the sound transmission loss. In Figure 3.12 the sound transmission loss of panels with resonators with different stiff and flexible parts is shown. From this, it can be concluded that the inferior performance of the entirely flexible panel is mainly caused by the deformations of the resonator walls. The first (coupled) structural eigenfrequency of the entirely flexible panel with resonators is 21 Hz.

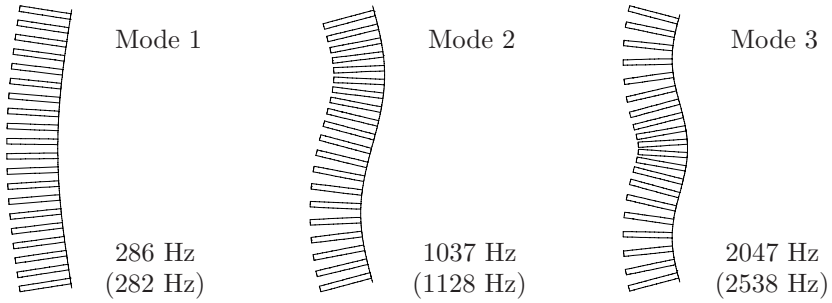


**Figure 3.11**: First three structural mode shapes (uncoupled) of the stiff panel with resonators. The corresponding eigenfrequencies of the stiff panel without resonators are shown in brackets.

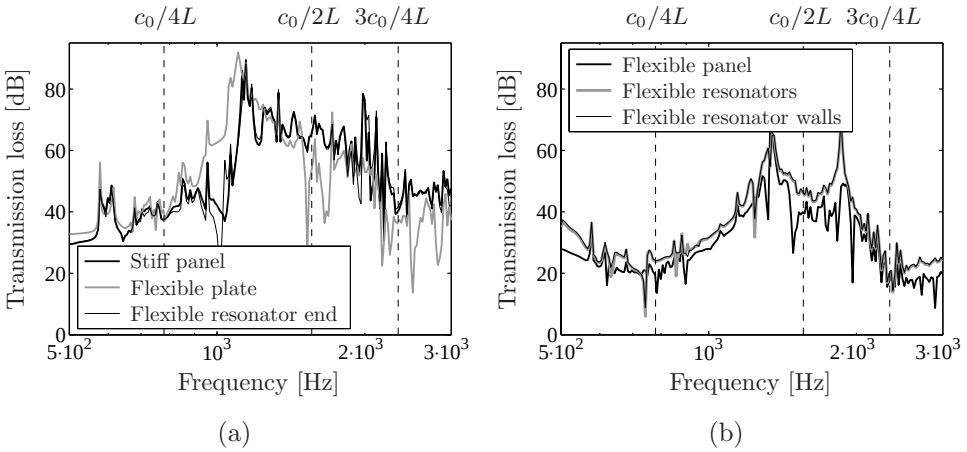


**Figure 3.12**: Sound transmission loss of panels with resonators with different stiff and flexible parts.

This means that, in the frequency range of interest, the modal density is rather high. The modes in this range are not only concerned with deformations of the plate, but also with the resonators, which now deform. This can clearly be seen in Figure 3.13, where the deformation shapes are shown which are associated with some maxima and minima in the sound transmission loss curve. The local peaks and troughs in the curves are, again, also partly caused by acoustic resonances in the room at the incident side. The acoustic eigenfrequencies of 577 Hz and 610 Hz are, for example, observed in all figures. In Figure 3.14 two other acoustic modes are shown, occurring at the large peak in Figure 3.9(b).

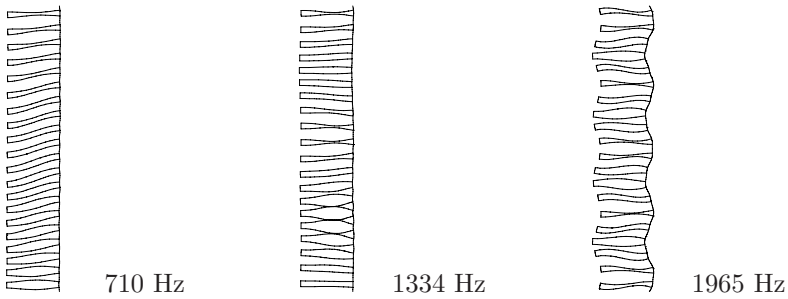


**Figure 3.13**: Structural deformation shapes (coupled) of the flexible panel with resonators.

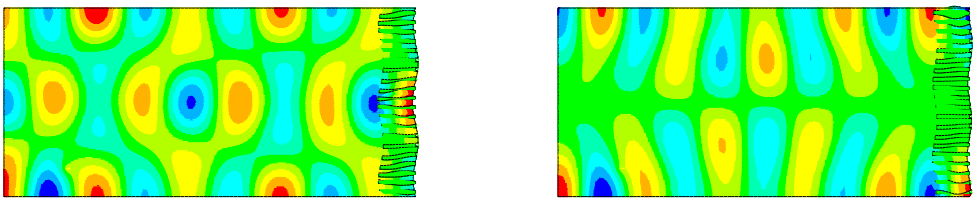


**Figure 3.14**: Acoustic mode shapes at the incident side of the flexible panel with resonators at 1299 Hz and 1334 Hz.

It should be noted that in the present model, the pressure of the air between the resonators is larger than in reality. This is caused by the fact that in a two-dimensional model, the air remains captured between the resonators, whereas in practice it can flow more freely around the resonators. The deformations of the walls of the resonators are therefore also larger here, having a more negative effect on the sound transmission loss.

### Position of sound source

In Figure 3.15(a) the sound transmission loss is shown for four different positions of the sound source. The coordinates of the respective positions are listed in Table 3.3. Since the panel was excited in different ways, small differences in sound transmission loss are observed. However, the general trends of the curves are the same.

### Sound absorbing walls in the receiving room

Figure 3.15(b) shows the sound transmission loss for different numbers of sound absorbing walls in the receiving room. In one case, only the back wall is sound

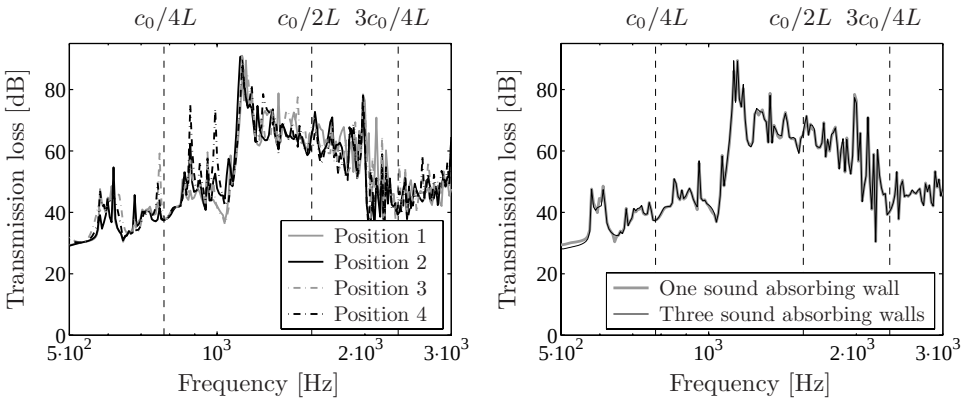


(a) Positions of the sound source. (b) Number of sound absorbing walls.

**Figure 3.15**: Sound transmission loss for different positions of the sound source and different numbers of sound absorbing walls in the receiving room.

| Position | $x_s$ [m] | $z_s$ [m] |
|---|---|---|
| 1 | $-1.0 - L$ | $3b$ |
| 2 | $-1.0 - L$ | $14b$ |
| 3 | $-0.5 - L$ | $3b$ |
| 4 | $-0.5 - L$ | $14b$ |

**Table 3.3**: Different positions of the source.

absorbing and the other two walls are acoustically hard. In the other case, all three wall are fully sound absorbing. A panel with resonators with a Young's modulus of $E = 70 \cdot 10^{12}$ N/m$^2$ was considered. No considerable differences are observed between the two curves.

## 3.4 Concluding remarks

In this chapter, two two-dimensional models were presented. The first, a semi-analytical model of an infinitely large, rigid panel with resonators, was used to study the influence of scattering by the resonator openings. Both sound radiation and normal incidence sound transmission were considered. It was seen that scattering by the resonator openings causes inlet effects, which make the effective length of the resonators slightly longer than the physical length. These effects hardly influence the insertion loss and the transmission loss. Only the maxima in the curves occur at slightly lower frequencies than

predicted by the one-dimensional analytical models presented in Chapter 2.

The second model was a two-dimensional FEM model of a panel with resonators, mounted between two rooms. With this model, the influence of different parameters on random incident sound transmission was examined for a specific configuration. It appeared that for a stiff panel, the sound transmission loss curve was similar to the sound transmission loss curve that was obtained with the one-dimensional analytical model presented in Chapter 2. Nevertheless, additional peaks and troughs appeared due to structural resonances of the panel and acoustic resonances in the room at the incident side. For a flexible panel, it was seen that the deformations of the resonator walls have a large influence on the sound transmission loss. For a stiff panel, the position of the sound source and the number of sound absorbing walls in the receiving room hardly influenced the sound transmission loss.

In Section 3.3.1, an approximation method was presented to make a distinction between the incident and the reflected sound intensities at the incident side of a panel. Using the pressure signals of a sound intensity probe with two closely spaced microphones (see Section 5.2.2), this method could also be applied for (in situ) sound transmission loss measurements in cases where no reverberation room is available. For spatially averaging the incident sound intensities, the so-called discrete point method (ISO 9614-1) could be applied.

# Chapter 4

# Three-dimensional modelling

## 4.1 Introduction

Up to now, only one-dimensional and two-dimensional models have been considered. To be able to model more complex and realistic setups, and to investigate the limitations of the previously presented models, this chapter introduces three three-dimensional numerical models.

All three methods presented here consist of a structural model of the panel and an acoustic model of the surrounding air. The coupling between these two parts is generally referred to as acousto-elastic interaction. For most modelling in this chapter, the finite element method (FEM) is used. The advantage of this method is that it is possible to model structures with complex geometries and different boundary conditions. Moreover, different sound fields can be considered. However, modelling the complete structure, including the resonators and the interaction with the air inside and around the resonators, is computationally very expensive. Especially when the models are used for optimisation purposes, long computation times are undesirable. To avoid this, all models presented here are reduced in some way.

#### Acousto-elastic interaction

The main difference between the three methods presented in this chapter lies in the modelling of the acousto-elastic interaction. Generally, there is a two-way coupling between the structure and the air (see Figure 4.1). The air exerts a force on the structure, inducing vibrations in the structure, and the other way around, the vibrations of the structure excite the surrounding air. In the case of one-way coupling, one of these mechanisms is assumed to be weak and is neglected in the model.

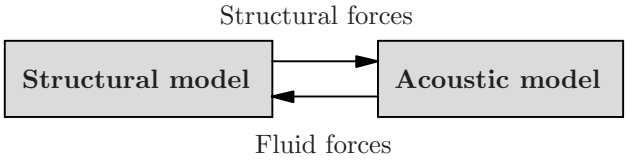


**Figure 4.1**: Two-way coupling of structural and acoustic model.

Another difference in the modelling of the acousto-elastic interaction is the way the flexibility of the resonators is taken into account. In the structural models of all methods, both the plate and the resonators are modelled as flexible structures. However, in the formulation of the acousto-elastic interaction, the resonators are in some cases assumed to be rigid. This means that in these cases no interaction between the deformation of the tubes and the air inside and around the resonators is taken into account. An overview of the three methods and the assumptions made for modelling the acousto-elastic interaction is shown in Table 4.1.

| **Method** | **Coupling** | **Flexibility of the resonators included** |
|---|---|---|
| Structural FEM + Rayleigh | One-way | No |
| Reduced FEM | Two-way | No |
| Full FEM | Two-way | Yes |

**Table 4.1**: Aspects regarding acousto-elastic interaction in the three-dimensional models.

In Section 4.2, the Rayleigh integral method is used to model free-field sound radiation by a panel with resonators which is assumed to be placed in an infinite baffle. The input for this method is the normal structural velocities which generally result from a structural analysis. The method is based on one-way coupling and in the formulation of the acousto-elastic interaction the resonators are assumed to be rigid. To study the effect of the boundaries of the panel, first a rigid panel with resonators is considered. Subsequently, sound radiation by a flexible panel with resonators is discussed. The structure is modelled here using the FEM.

In Section 4.3, sound transmission is investigated. Both the structure and the surrounding air are now modelled using the FEM. To reduce computation time, a reduced model is developed, which takes advantage of the repetitive pattern of resonators in the panel. Two-way coupling is included, but in the formulation of the acousto-elastic interaction the resonators are still assumed

to be rigid.

In Section 4.4, the effect of local deformations of the resonators is studied by means of a full FEM model of one characteristic area. The model now includes both two-way coupling and the interaction between the deformations of the tube and the air inside and around the resonators.

Because the resonators in question are relatively wide, no viscothermal effects are taken into account in this chapter. Furthermore, only the tube panel configuration is considered here (see Figure 2.1). However, with some small adjustments, the models can also be used to analyse sandwich panel configurations (see Figure 2.9).

## 4.2 Rayleigh integral method

In the (semi-)analytical models presented in the previous chapters, the panels with resonators were assumed to be infinitely large. In this section, panels of finite dimensions are considered, which are assumed to be placed in an infinite baffle. By means of the Rayleigh integral method, the free-field sound radiation is predicted for a given vibration response of the structure. In contrast to a panel without resonators, the surface velocities of the structure are not equal to the fluid velocities close to the surface. An impedance relation is therefore derived between these two quantities.

### 4.2.1 Theory

Wave propagation through a homogeneous fluid such as air is described by the wave equation [22]. In the case of harmonic time dependence, this equation reduces to the so-called Helmholtz differential equation. In the absence of external volume sources, the latter equation can be written as:

$$\nabla^2 p(\mathbf{r}) + k^2 p(\mathbf{r}) = 0 \tag{4.1}$$

where $p(\mathbf{r})$ is the pressure at location $\mathbf{r}$. To solve this equation, the Helmholtz differential equation is often transformed into the so-called Kirchhoff-Helmholtz integral equation, which is given by:

$$\alpha(\mathbf{r})p(\mathbf{r}) = \int_S \left[ p(\mathbf{r}_0) \frac{\partial G(\mathbf{r}, \mathbf{r}_0)}{\partial n} + \mathrm{i}\omega\rho_0 v(\mathbf{r}_0)\, G(\mathbf{r}, \mathbf{r}_0) \right] \mathrm{d}S \tag{4.2}$$

The pressure at location $\mathbf{r}$ is now related to the pressure $p(\mathbf{r}_0)$ and the normal fluid velocity $v(\mathbf{r}_0)$ close to the surface. The factor $\alpha(\mathbf{r})$ depends on the position where the pressure is evaluated; $\alpha(\mathbf{r}) = 1$ for an exterior point and

$\alpha(\mathbf{r}) = 0.5$ for a point on the (smooth) surface $S$. The Green's function $G(\mathbf{r}, \mathbf{r}_0)$ is the solution of the Helmholtz differential equation in the case of excitation by a Dirac pulse and is given by:

$$G(\mathbf{r}, \mathbf{r}_0) = \frac{e^{-\mathrm{i}k|\mathbf{r}-\mathbf{r}_0|}}{4\pi|\mathbf{r}-\mathbf{r}_0|} \tag{4.3}$$

For a flat panel in an infinite baffle, the Kirchhoff-Helmholtz integral equation (4.2) reduces to Rayleigh's second integral (or the Rayleigh integral) [22]:

$$p(\mathbf{r}) = \frac{\mathrm{i}\omega\rho_0}{2\pi} \int_S v(\mathbf{r}_0) \frac{e^{-\mathrm{i}k|\mathbf{r}-\mathbf{r}_0|}}{|\mathbf{r}-\mathbf{r}_0|} \mathrm{d}S \tag{4.4}$$

A schematic representation of the vectors in this expression is depicted in Figure 4.2.

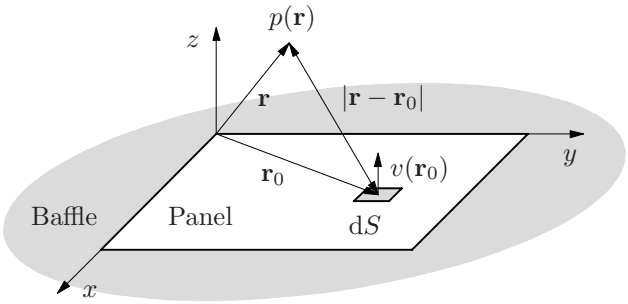


**Figure 4.2**: Geometric representation of vectors in the Rayleigh integral.

### Discretisation

To solve the Rayleigh integral, the structure is divided into $N$ rectangular elements of equal size, which are small compared to the acoustic wavelength. The normal surface velocity is assumed to be constant across each element. Physically, these elements can be seen as a set of elemental radiators or pistons which each move harmonically with constant velocity amplitude. Applying this discretisation, equation (4.4) can be written as:

$$\mathbf{p} = \mathbf{Z}\mathbf{v} \tag{4.5}$$

where $\mathbf{p}$ is the vector with pressures in the field points, $\mathbf{v}$ is the vector with $N$ normal fluid velocities close to the surface of the elemental radiators, and $\mathbf{Z}$ is

acoustic impedance matrix. The elements of this frequency dependent matrix are given by:

$$Z_{ij} = \frac{\mathrm{i}\omega\rho_0 S_e}{2\pi} \frac{e^{-\mathrm{i}kr_{ij}}}{r_{ij}} \tag{4.6}$$

where $S_e$ is the area of the elemental radiator, and $r_{ij} = |\mathbf{r}_i - \mathbf{r}_j|$ is the distance between a field point $i$ and a surface point $j$. If the pressure is evaluated at the location of the elemental radiator (i.e. $r_{ii} = 0$), this expression becomes singular. To avoid this singularity, the diagonal elements in the impedance matrix are approximated by the impedance of a baffled circular piston of the same area, so $R = \sqrt{S_e/\pi}$. This impedance is given by [6]:

$$Z_{ii} = \rho_0 c_0 \left[ \frac{(kR)^2}{2} + \frac{8\mathrm{i}kR}{3\pi} \right] \tag{4.7}$$

To determine the radiated sound power, the pressures $\mathbf{p}$ are evaluated at the same points close to the surface as $\mathbf{v}$. By combining equations (2.50) and (4.5), the radiated sound power can now be written as:

$$\bar{W} = \frac{S_e}{2} \mathrm{Re}\left[ (\mathbf{v})^{\mathrm{H}} \, \mathbf{p}_{\mathrm{surf}} \right] = \frac{S_e}{2} \mathrm{Re}\left[ (\mathbf{v})^{\mathrm{H}} \, \mathbf{Z}_{\mathrm{surf}} \, \mathbf{v} \right] \tag{4.8}$$

where superscript H denotes the complex conjugate transpose (Hermitian), and $\mathbf{p}_{\mathrm{surf}} = \mathbf{Z}_{\mathrm{surf}} \, \mathbf{v}$ are the surface pressures, with $\mathbf{Z}_{\mathrm{surf}}$ the (square) impedance matrix evaluated close to the vibrating surface. Hence, for calculating the radiated sound power, the normal fluid velocities $\mathbf{v}$ close to the surface have to be known.

### Fluid velocities

Close to the surface of an acoustically hard panel without resonators, the normal fluid velocities $\mathbf{v}$ are equal to the normal structural velocities $\mathbf{v}_s$ (see Figure 4.3(a)). The structural velocities generally result from a structural analysis. However, for a panel with resonators, the normal fluid velocities $\mathbf{v}$ close to the surface are not equal to the normal structural velocities $\mathbf{v}_s$ (see Figure 4.3(b)). Therefore, an impedance relation is derived to relate these two quantities.

For this purpose, a characteristic area of a panel with resonators is considered (see Figure 4.4). The characteristic area vibrates harmonically with a normal structural velocity $v_s$ and is assumed to be rigid and small compared to the acoustic wavelength. As in the previous chapters, the air inside the resonators is approximated by a one-dimensional sound field, so the wave

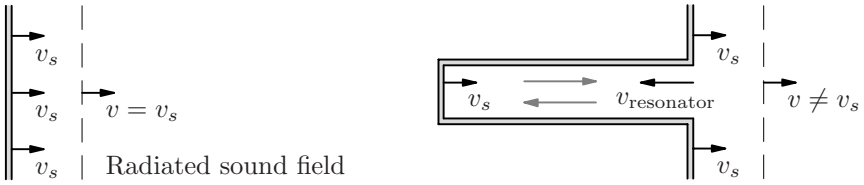


(a) Panel without resonators. (b) Panel with resonators.

**Figure 4.3**: Normal fluid velocities $v$ close to the surface.

propagation is described by equations (2.21) and (2.26). If viscothermal effects are neglected, the boundary conditions (2.38) to (2.40) at the end and the entrance of the resonator, respectively, can be written as:

$$-\frac{1}{\rho_0 c_0}(\mathbf{a}-\mathbf{b}) = \mathbf{v}_s \tag{4.9}$$

$$\mathbf{a}e^{\mathrm{i}kL} + \mathbf{b}e^{-\mathrm{i}kL} = \mathbf{p}_{\text{surf}} \tag{4.10}$$

$$-\frac{S_r}{\rho_0 c_0}\left(\mathbf{a}e^{\mathrm{i}kL} - \mathbf{b}e^{-\mathrm{i}kL}\right) + \mathbf{v}_s(S - S_r) = \mathbf{v}S \tag{4.11}$$

where $\mathbf{a}$ and $\mathbf{b}$ are vectors with the pressure amplitudes $A$ and $B$ inside the resonators, for each elemental radiator. Note that, in contrast to the model presented in Chapter 2, the radiated sound field is now not described by the solution of the one-dimensional wave equation, but by the Rayleigh integral.

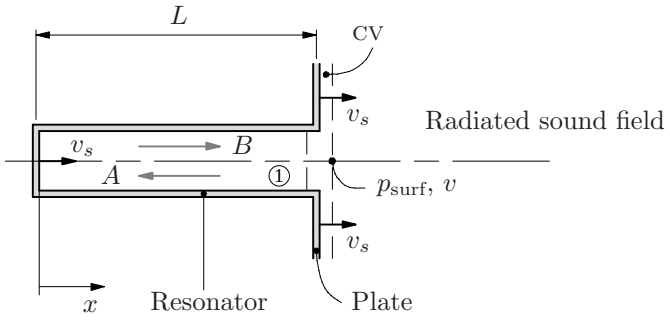


**Figure 4.4**: Model of sound radiation by a rigid characteristic area.

For a given set of normal structural velocities $\mathbf{v}_s$, the surface pressures can be solved from equations (4.9) to (4.11) as a function of the fluid velocities:

$$\mathbf{p}_{\text{surf}} = \chi_1 \mathbf{v} + \chi_0 \mathbf{v}_s \tag{4.12}$$

with:

$$\chi_1 = \mathrm{i}\rho_0 c_0 \frac{1}{\Omega \tan(kL)}$$
$$\chi_0 = \mathrm{i}\rho_0 c_0 \left[ \frac{1}{\tan(kL)} - \frac{1}{\Omega \tan(kL)} - \frac{1}{\sin(kL)} \right] \tag{4.13}$$

According to equation (4.5), the surface pressures can also be written as:

$$\mathbf{p}_{\mathrm{surf}} = \mathbf{Z}_{\mathrm{surf}} \mathbf{v} \tag{4.14}$$

Combining equations (4.12) and (4.14) finally yields the following expression for the fluid velocities:

$$\mathbf{v} = \chi_0 (\mathbf{Z}_{\mathrm{surf}} - \chi_1 \mathbf{I})^{-1} \mathbf{v}_s \tag{4.15}$$

where $\mathbf{I}$ is the identity matrix. For the examples in this work, the matrix $\mathbf{Z}_{\mathrm{surf}} - \chi_1 \mathbf{I}$ is inverted using the GMRES (generalised minimal residual) method [44]. The speed and memory usage were further improved by taking advantage of the fact that the matrix is a Toeplitz matrix [57]. The radiated sound power is finally calculated by substituting the solution for $\mathbf{v}$ into equation (4.8).

It should be stressed that the model of one characteristic area is only used to derive a relation between the normal structural velocities $\mathbf{v}_s$ and the normal fluid velocities $\mathbf{v}$ close to the surface. The number of elemental radiators that is used in the calculations is mainly determined by the convergence of the solution and does not need to be equal to the number of characteristic areas in the panel.

### 4.2.2 Sound radiation

In this section, two examples are discussed. First, the influence of the boundaries is demonstrated by assuming the panels with resonators to be rigid. Second, a flexible panel with resonators is considered.

#### Rigid panel - influence of the boundaries

In this example, two baffled panels with resonators are considered, both of different dimensions. The dimensions of the first panel are $1.00 \times 1.00$ m and the dimensions of the other panel are $0.40 \times 0.40$ m. Both panels are assumed to be rigid, which means that the structural velocity $v_s$ is the same for all elemental radiators (see Figure 4.5(a)). The resonators have a length of $L = 0.11$ m, while the porosity of the panels is varied. The size of the characteristic

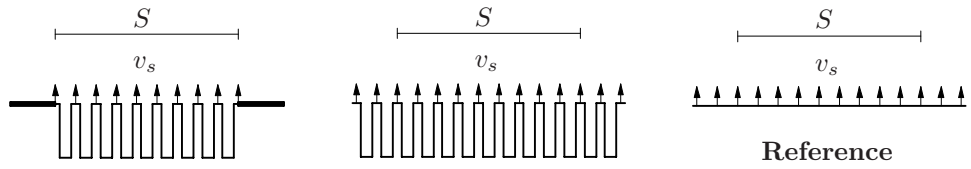


(a) Baffled panel with resonators (3D).

(b) Infinitely large panel with resonators (1D).

(c) Infinitely large panel without resonators (1D).

**Figure 4.5**: Rigid panels with and without resonators, with different boundary conditions.

areas is assumed to be small compared to the acoustic wavelength. Both acoustic models consisted of 32 × 32 elemental radiators.

To investigate the influence of the boundaries of the baffled panels with resonators, a comparison is made with the one-dimensional model as described in Section 2.3.1. Here, the panels with resonators were also assumed to be rigid. However, instead of baffled, they were assumed to be infinitely large (see Figure 4.5(b)).

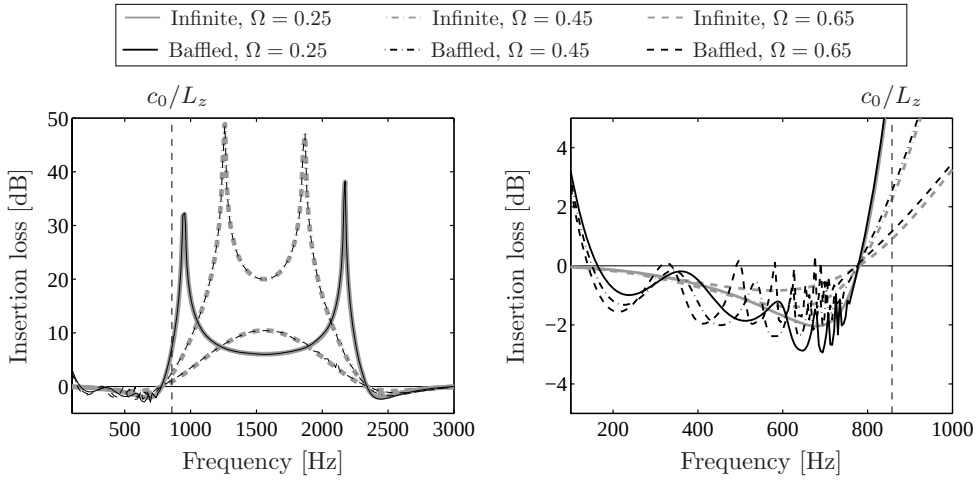


(a) Full frequency range.

(b) Low frequency range.

**Figure 4.6**: Insertion loss of a baffled (1.00 × 1.00 m) panel with resonators and an infinitely large panel with resonators ($L = 0.11$ m).

In Figures 4.6 and 4.7 the insertion loss of the two panels with resonators is shown for different porosities. The insertion loss was determined as described in Section 2.4.1. To clearly show the effect of the boundaries, the sound power

level radiated by an infinitely large, rigid panel without resonators, was used as a reference here (see Figure 4.5(c)). In the latter case, the radiated sound power was calculated over an area $S$ with the same dimensions as the baffled panel.

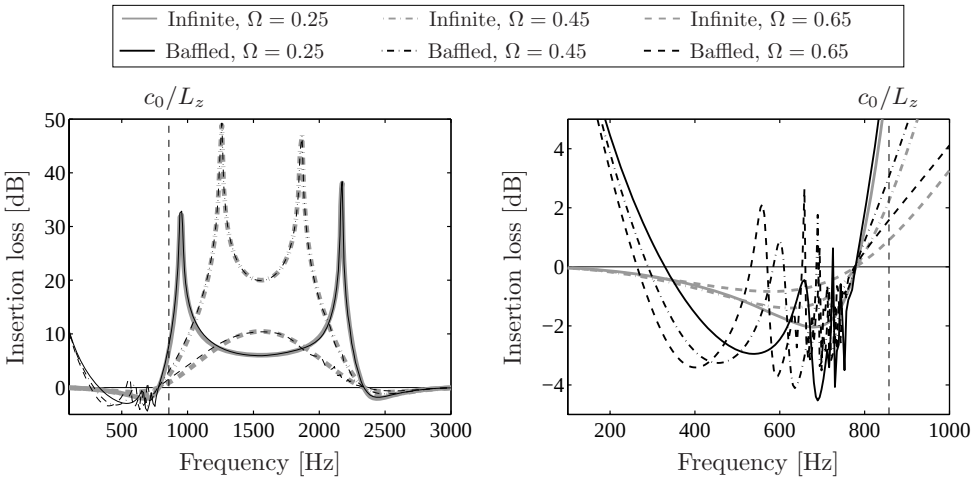


(a) Full frequency range. (b) Low frequency range.

**Figure 4.7**: Insertion loss of a baffled (0.40 × 0.40 m) panel with resonators and an infinitely large panel with resonators ($L = 0.11$ m).

Comparison of the baffled panels with resonators with the infinitely large panels with resonators (see Figures 4.6 and 4.7) shows that if the acoustic wavelength is small compared to the dimensions $L_y$ and $L_z$ of the panels (i.e. at higher frequencies), the boundaries do not play a role. However, if the acoustic wavelength and the dimensions of the panels are of the same order (i.e. at lower frequencies), the boundaries start influencing the radiated sound power.

Figures 4.8 and 4.9 show the pressure and normal velocity distributions over one of the baffled panels with resonators at a frequency where the acoustic wavelength is small compared to the dimensions of the panels. It can be seen that the distributions are by no means uniform (but oscillatory). However, the radiated sound power is the same as would be radiated by a section of a uniform plane wave of area $L_y \times L_z$. A similar observation was made in the book by Bies and Hansen [6] concerning the radiation of sound by a baffled circular piston.

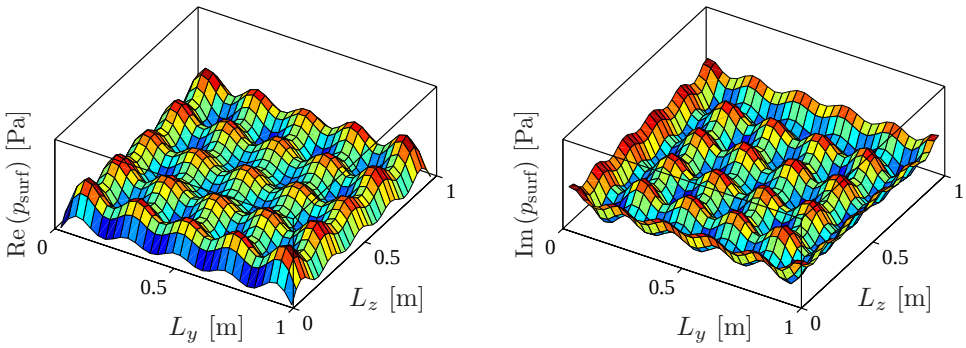


(a) Real part. (b) Imaginary part.

**Figure 4.8**: Pressure distribution over a baffled (1.00 × 1.00 m) panel with resonators at 1700 Hz ($L = 0.11$ m, $\Omega = 0.25$).

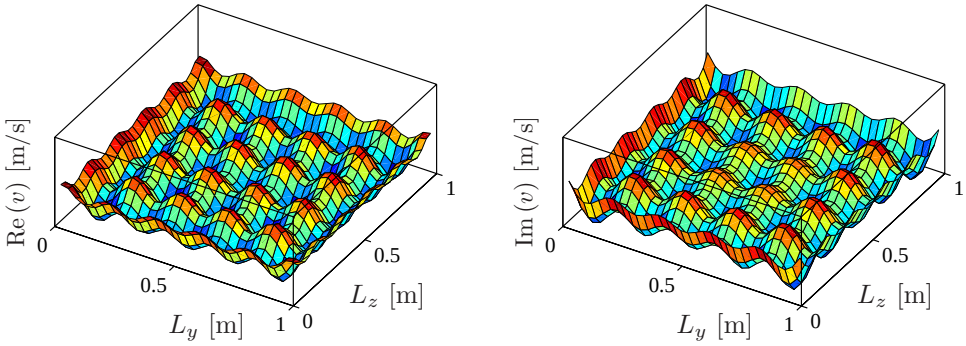


(a) Real part. (b) Imaginary part.

**Figure 4.9**: Normal fluid velocity distribution over a baffled (1.00 × 1.00 m) panel with resonators at 1700 Hz ($L = 0.11$ m, $\Omega = 0.25$).

### Flexible panel

In this example a baffled, flexible panel with resonators is considered (see Figure 4.10(a)). The panel contains 20 × 20 resonators, and the dimensions and the material properties of the plate and the resonators are listed in Table 4.2. $R$ is the resonator radius, $L$ is the resonator length, $t_w$ is the thickness of the resonator walls, $t_e$ is the thickness of the resonator ends, $L_y$ and $L_z$ are the height and width of the plate, $t_p$ is the thickness of the plate, and $b$ is the width of a characteristic area. The Young's modulus of the structure is chosen to be relatively high here to reduce the modal density in the considered frequency

range. The simply supported panel was structurally excited by applying a unit force at the arbitrary point $(x, y) = (3b, 2b)$, measured from one of the corners of the plate.

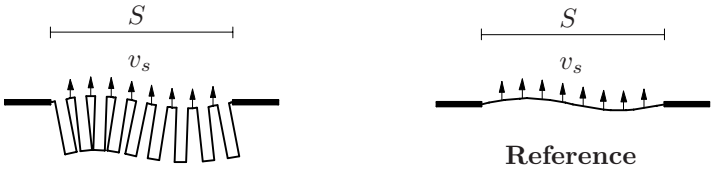


(a) Panel with resonators. (b) Panel without resonators.

**Figure 4.10**: Baffled, flexible panels with and without resonators (3D).

| Resonator | | |
|---|---|---|
| $R$ | 0.0095 | m |
| $L$ | 0.11 | m |
| $t_w$ | 0.0003 | m |
| $t_e$ | 0.0006 | m |

| Plate | | |
|---|---|---|
| $L_y$ | 0.50 | m |
| $L_z$ | 0.50 | m |
| $t_p$ | 0.002 | m |
| $b$ | 0.025 | m |

| Material | | |
|---|---|---|
| $\rho$ | 2710 | kg/m$^3$ |
| $E$ | $70{\cdot}10^{12}$ | N/m$^2$ |
| $\nu$ | 0.3 | - |

**Table 4.2**: Dimensions and material properties of the panel.

Since weak coupling was assumed between the vibration of the panel and the radiated sound field, the analysis could be performed in two steps. First, the normal structural velocity distribution $\mathbf{v}_s$ due to the excitation force was determined by performing a harmonic response analysis on the structure. This analysis was performed using the FEM. The panel was modelled using the commercial FEM program ANSYS. Second, the structural velocities were imported in MATLAB, where the radiated sound power was determined by means of the Rayleigh integral method. A schematic representation of this procedure is depicted in Figure 4.11.

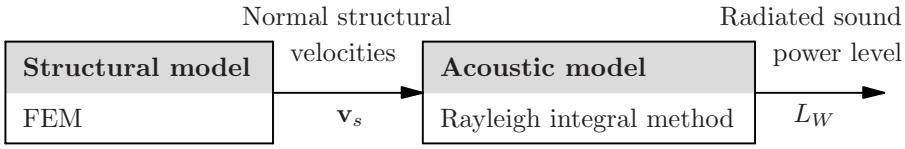


**Figure 4.11**: One-way coupling of structural and acoustic model.

The structural model was composed of linear four-node plate elements (SHELL63). To reduce computation time, the structural analysis was per-

formed using component mode synthesis (CMS). The acoustic model consisted of 20 × 20 elemental radiators, coinciding with the characteristic areas of the panel. The normal structural velocities $\mathbf{v}_s$ in the centres of the elemental radiators were calculated by averaging the normal structural velocities of 16 master nodes at the plate boundaries of the characteristic areas. Note that, to determine the structural response, the entire structure was flexible. However, in the formulation of the interaction with the air inside the resonators, the influence of the flexibility of the resonators was neglected.

In Figure 4.12 the radiated sound power level and the insertion loss of the baffled, flexible panel with resonators are shown. As a reference for the insertion loss, the radiated sound power of a baffled, flexible panel without resonators was used (see Figure 4.10(b)). This panel had the same normal structural velocity distribution (i.e. the same dynamic properties) as the panel with resonators. For both panels, the Rayleigh integral method was used.

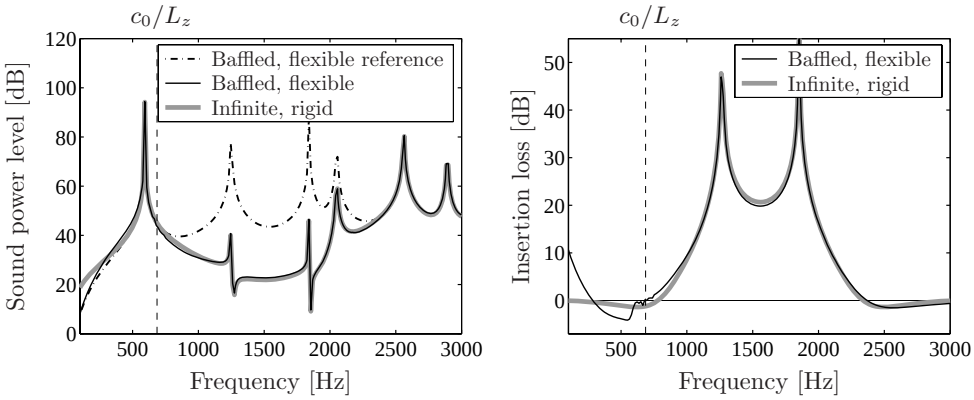


(a) Radiated sound power level.

(b) Insertion loss.

**Figure 4.12**: Radiated sound power level and insertion loss of baffled, flexible panel with resonators and infinitely large, rigid panel with resonators.

Figure 4.12 also shows the prediction for an infinitely large, rigid panel with resonators (see Figure 4.5(b)). The results are obtained with the one-dimensional analytical model as presented in Section 2.3.1. The frequency dependent, normal structural velocity $v_s$ that was prescribed to calculate the radiated sound power equalled the spatial average of the normal structural velocity $\mathbf{v}_s$ resulting from the structural analysis of the baffled, flexible panel.

The peaks that appear in the radiated sound power level correspond to the first six structural eigenfrequencies of the panel. Comparison of the insertion loss curves again only shows discrepancies in the frequency range where the

dimensions of the panel are smaller than, or of the same order as the acoustic wavelength.

## 4.3 Reduced finite element model

In this section, the transmission of sound through panels with resonators is modelled using the FEM. In contrast to the model presented in the previous section, two-way coupling is now present between the structure and the surrounding air. To reduce computation time, a reduced model is developed here. In the previous chapters, it was seen that the structure is characterised by a repetitive pattern of resonators. Advantage can be taken of this by using substructuring. By means of the Guyan reduction method, so-called superelements are generated to represent the structural part of each characteristic area (see Figure 4.13). The acoustic domains on both sides of the panel are modelled using standard fluid elements. To enable coupling between the structure and the air, a new interface element is formulated [28]. Besides acousto-elastic interaction, this interface element also includes the acoustic behaviour of the air inside and around the resonators. This means that these air volumes do not need to be meshed by fluid elements. As will be shown later, the same interface elements can be used for both sides of the panel.

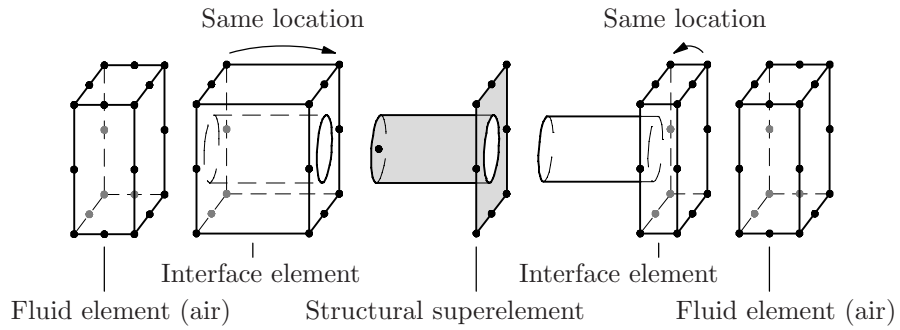


**Figure 4.13**: Element types to model a panel with resonators with air on both sides.

### 4.3.1 Structural model

The number of degrees of freedom (DOF), and thus the computation time, of the structural model of the panels with resonators can be reduced considerably by applying substructuring. The reduction method that is used here is Guyan reduction.

### Guyan reduction

In the Guyan reduction method, the entire set of DOF of a substructure is condensed to a smaller set of so-called interface DOF or master DOF [25]. This leads to a superelement with a reduced mass and stiffness matrix. For a panel with resonators, a substructure consists of the structural part of one characteristic area. Because all characteristic areas are identical, only one superelement has to be generated. By connecting the substructures at their shared master nodes, the complete structure is assembled.

To demonstrate the method, the equations of motion for a substructure in the frequency domain are partitioned into two groups:

$$-\omega^2 \begin{bmatrix} \mathbf{M}^{mm} & \mathbf{M}^{ms} \\ (\mathbf{M}^{ms})^{\mathrm{T}} & \mathbf{M}^{ss} \end{bmatrix} \begin{Bmatrix} \mathbf{u}^m \\ \mathbf{u}^s \end{Bmatrix} + \begin{bmatrix} \mathbf{K}^{mm} & \mathbf{K}^{ms} \\ (\mathbf{K}^{ms})^{\mathrm{T}} & \mathbf{K}^{ss} \end{bmatrix} \begin{Bmatrix} \mathbf{u}^m \\ \mathbf{u}^s \end{Bmatrix} = \begin{Bmatrix} \mathbf{f}^m \\ \mathbf{f}^s \end{Bmatrix} \tag{4.16}$$

where $\mathbf{u}^s$ are the internal or slave DOF, and $\mathbf{u}^m$ are the DOF on the interface boundaries or master DOF. Solving the second set of equations and substituting this into the first set of equations, would yield a smaller system with only $\mathbf{u}^m$ as DOF. However, the matrices of the reduced system would be frequency dependent. Therefore, Guyan suggested neglecting the inertia forces in the second set of equations. Solving $\mathbf{u}^s$ from the first set of equations then gives:

$$\mathbf{u}^s = -(\mathbf{K}^{ss})^{-1}(\mathbf{K}^{ms})^{\mathrm{T}}\mathbf{u}^m + (\mathbf{K}^{ss})^{-1}\mathbf{f}^s \tag{4.17}$$

The displacements can now be written as:

$$\mathbf{u} = \begin{Bmatrix} \mathbf{u}^m \\ \mathbf{u}^s \end{Bmatrix} = \boldsymbol{\psi}\mathbf{u}^m + \boldsymbol{\phi}$$

$$\text{with} \quad \boldsymbol{\psi} = \begin{Bmatrix} \mathbf{I} \\ -(\mathbf{K}^{ss})^{-1}(\mathbf{K}^{ms})^{\mathrm{T}} \end{Bmatrix} \quad \text{and} \quad \boldsymbol{\phi} = \begin{Bmatrix} \mathbf{0} \\ -(\mathbf{K}^{ss})^{-1}\mathbf{f}^s \end{Bmatrix} \tag{4.18}$$

Physically, the $j$th column of $\boldsymbol{\psi}$ represents the static displacement of the structure when the $j$th master DOF has unit displacement and all other master DOF are kept fixed. This displacement state is also called a constraint mode [13]. Substitution of equation (4.18) into the full set of equations of motion and premultiplication by $\boldsymbol{\psi}^{\mathrm{T}}$ yields the following reduced set of equations:

$$-\omega^2\mathbf{M}^{\mathrm{sub}}\mathbf{u}^m + \mathbf{K}^{\mathrm{sub}}\mathbf{u}^m = \mathbf{f}^{\mathrm{sub}} \tag{4.19}$$

with the reduced stiffness matrix, mass matrix and load vector of the substructure defined as:

$$\mathbf{K}^{\mathrm{sub}} = \boldsymbol{\psi}^{\mathrm{T}}\mathbf{K}\boldsymbol{\psi} \qquad \mathbf{M}^{\mathrm{sub}} = \boldsymbol{\psi}^{\mathrm{T}}\mathbf{M}\boldsymbol{\psi} \qquad \mathbf{f}^{\mathrm{sub}} = \boldsymbol{\psi}^{\mathrm{T}}(\mathbf{f} - \mathbf{M}\boldsymbol{\phi} - \mathbf{K}\boldsymbol{\phi}) \tag{4.20}$$

where $\mathbf{K}$, $\mathbf{M}$ and $\mathbf{f}$ are the full stiffness matrix, mass matrix and load vector, respectively. $\mathbf{M}^{\text{sub}}$ and $\mathbf{K}^{\text{sub}}$ are again symmetric matrices. The internal DOF of the $i$th constraint mode can be recovered from the second set of equations (4.16) by:

$$\begin{aligned}(\mathbf{u}^s)_i = &- [\mathbf{K}^{ss} - \omega_i^2 \mathbf{M}^{ss}]^{-1}[(\mathbf{K}^{ms})^{\mathrm{T}} - \omega_i^2 (\mathbf{M}^{ms})^{\mathrm{T}}](\mathbf{u}^m)_i + \\ &+ [\mathbf{K}^{ss} - \omega_i^2 \mathbf{M}^{ss}]^{-1}\mathbf{f}^s \end{aligned} \tag{4.21}$$

In static analysis, Guyan reduction introduces no additional approximation into FEM model. However, in dynamic analysis, the original eigenvalue problem is not exactly preserved, since the inertia forces are not correctly taken into account.

A more accurate and widely used reduction method for dynamic analysis is the Craig-Bampton method, a kind of component mode synthesis [16]. Besides the constraint modes, a number of so-called component modes, i.e. vibration modes of the individual substructure with its master DOF fixed, is included as an additional set of generalised DOF. However, in FEM code that was used for the relevant model, this reduction method could not be applied (yet).

#### Substructures

An example of a mesh for the generation of the superelements, and the resulting superelement are shown in Figure 4.14. Because of the FEM code that was adopted, the meshes of the structural and the acoustic domain had to coincide. In the examples presented in this section, the air behind and in front of the panel is modelled with 20-node hexahedral fluid elements (see Figure 4.13). The superelements can therefore only contain eight master nodes at the plate boundaries. For an accurate representation of the structural response, a ninth master node is located at the end of the resonator, taking into account the inertia and stiffness effects of the tube. The DOF of the latter node are, however, not coupled to the acoustic domain. All master nodes have six degrees of freedom, three displacements and three rotations.

### 4.3.2 Acousto-elastic interaction

The structure and the air behind and in front of the panel are coupled by means of a new interface element. This interface element describes both the acousto-elastic interaction and the acoustic behaviour of the resonators. The finite element formulation of this element is presented below.

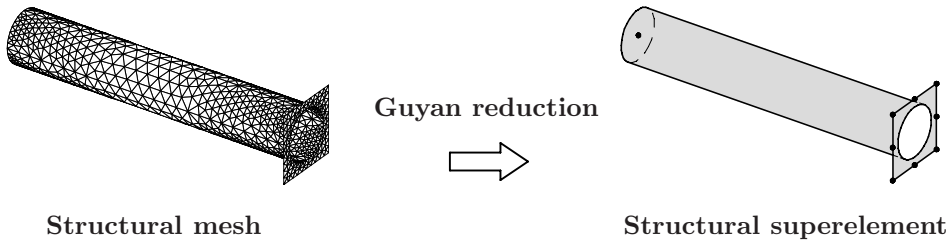


**Figure 4.14**: Structural mesh for generating structural superelement.

### Basics for finite element formulation of interface elements

Figure 4.15 shows a schematic representation of a characteristic area with a resonator of length $L$. $p_l$ and $p_r$ are the pressures at the left-hand side and the right-hand side of the panel, respectively. The purpose of the interface element is to relate the pressures to the structural displacements of the panel.

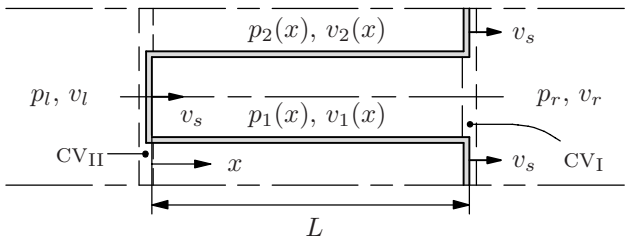


**Figure 4.15**: Characteristic area with parameters used to formulate the interface element.

For the derivation of the interface element, the characteristic area is assumed to be rigid, so both the plate and the resonator are assumed to vibrate with the same normal structural velocity $v_s e^{\mathrm{i}\omega t}$. Note that this assumption is only used to find a relation between the pressures and the structural displacements. In the complete FEM model, the panel is modelled as a flexible structure, so there can be a velocity distribution over the characteristic areas. The assumption also implies that no interaction between the deformation of the tubes and the air inside and around the resonators is taken into account. The dimensions of the characteristic areas are assumed to be small compared to the acoustic wavelength.

### Basic equations

The pressures $p_1$ and $p_2$ and the fluid velocities $v_1$ and $v_2$ in axial direction, inside and around the resonators (see Figure 4.15), are described by the solutions of the one-dimensional Helmholtz equation and Euler's equation:

$$p_j(x) = A_j e^{\mathrm{i}kx} + B_j e^{-\mathrm{i}kx} \qquad j = 1, 2 \tag{4.22}$$

$$v_j(x) = -\frac{1}{\rho_0 c_0}\left(A_j e^{\mathrm{i}kx} - B_j e^{-\mathrm{i}kx}\right) \qquad j = 1, 2 \tag{4.23}$$

The amplitudes of the backward and forward travelling sound waves inside and around the resonators, $A_j$ and $B_j$, respectively, are determined by the boundary conditions of these domains. In this derivation no viscothermal effects are taken into account. At the right-hand side of the panel, the same boundary conditions are applied as in Section 2.3.1. These conditions can be formulated as follows:

$$v_1|_{x=0} = v_s \tag{4.24}$$

$$p_1|_{x=L} = p_r \tag{4.25}$$

$$v_1|_{x=L}\, S_r + v_s\,(S - S_r) = v_r\, S \tag{4.26}$$

At the left-hand side of the panel similar boundary conditions have to be satisfied. These conditions are described by equations (2.41) to (2.43) and are written as:

$$v_2|_{x=L} = v_s \tag{4.27}$$

$$p_2|_{x=0} = p_l \tag{4.28}$$

$$v_2|_{x=0}\, S_l + v_s\,(S - S_l) = v_l\, S \tag{4.29}$$

where $S_l$ is the cross-sectional area of the air volume around the resonators[1]. By substitution of equations (4.27) and (4.28) into equations (4.22) and (4.23), the pressure amplitudes $A_2$ and $B_2$ can be solved. Substituting these solutions back into equation (4.22), gives the following expression for the pressure at the panel:

$$p_2|_{x=L} = p_l \sec(kL) - \mathrm{i}\rho_0 c_0 v_s \tan(kL) \tag{4.30}$$

where $\sec(kL) = 1/\cos(kL)$. The total force at the left-hand side of the characteristic area is:

$$F_l = p_l\,(S - S_l) + p_2|_{x=L}\, S_l \tag{4.31}$$

[1] If the wall thickness of the resonator is neglected, $S_l = S - S_r$.

Assuming the force to be uniformly distributed over the area, the distributed load is given by $q_l = F_l/S$. Introduction of the porosity $\Omega_l = S_l/S$ and substitution of equation (4.30) into the expression for the distributed load, gives:

$$q_l = p_l[1 - \Omega_l + \Omega_l \sec(kL)] - \mathrm{i}\rho_0 c_0 v_s \Omega_l \tan(kL) \tag{4.32}$$

By using equations (4.23) and (4.29), the fluid velocity at the left-hand side of the panel can be formulated as:

$$\rho_0 c_0 v_l = \rho_0 c_0 v_s[1 - \Omega_l + \Omega_l \sec(kL)] + \mathrm{i}p_l \Omega_l \tan(kL) \tag{4.33}$$

Since the velocity perturbations are assumed to be harmonic, relations (4.32) and (4.33) can be rewritten as:

$$q_l = p_l[1 - \Omega_l + \Omega_l \sec(kL)] + \rho_0 c_0 u_s \omega \Omega_l \tan(kL) \tag{4.34}$$

$$\rho_0 c_0 a_l = \rho_0 c_0 a_s[1 - \Omega_l + \Omega_l \sec(kL)] - p_l \omega \Omega_l \tan(kL) \tag{4.35}$$

where $u_s$ is the normal structural displacement, $a_s$ is the normal structural acceleration, and $a_l$ is the normal fluid acceleration.

In the same way, by using equations (4.24) to (4.26), similar expressions are found for the distributed load and the fluid acceleration at the right-hand side of the panel. The only difference is the change of the signs of the accelerations, velocities and displacements. This means that at both sides of the panel the same interface elements can be used. The subscripts $l$ and $r$ will therefore be omitted from now on.

**Finite element discretisation**

For discretisation, the pressures $p$ and the *normal* structural displacements $u_s$ are written in terms of vectors with nodal pressures $\mathbf{p}$ and nodal structural displacements $\mathbf{u}$, and vectors with interpolation functions $\mathbf{N}_f$ and $\mathbf{N}_s$:

$$p = (\mathbf{N}_f)^{\mathrm{T}} \mathbf{p}, \quad u_s = (\mathbf{N}_s)^{\mathrm{T}} \mathbf{u} \tag{4.36}$$

The element matrices for the acoustic part of the interface element are obtained by discretising the wave equation and substitution of equation (4.35). The element matrices of the structural part are obtained by discretising the equation of motion and substitution of equation (4.34). For both discretisations the Galerkin method is applied, which means that the weight functions are chosen equal to the interpolation functions [59]. Finally, this leads to the

following set of equations:

$$-\omega^2 \begin{bmatrix} \mathbf{M}_s & \mathbf{0} \\ \mathbf{M}_{fs}^{pu}(\omega) & \mathbf{M}_f + \mathbf{M}_{fs}^{pp}(\omega) \end{bmatrix} \begin{Bmatrix} \mathbf{u} \\ \mathbf{p} \end{Bmatrix} + \begin{bmatrix} \mathbf{K}_s + \mathbf{K}_{fs}^{uu}(\omega) & \mathbf{K}_{fs}^{up}(\omega) \\ \mathbf{0} & \mathbf{K}_f \end{bmatrix} \begin{Bmatrix} \mathbf{u} \\ \mathbf{p} \end{Bmatrix} = \\ = \begin{Bmatrix} \mathbf{f}_s \\ \mathbf{0} \end{Bmatrix} \tag{4.37}$$

where $\mathbf{M}_s$, $\mathbf{M}_f$, $\mathbf{K}_s$ and $\mathbf{K}_f$ are the structural and acoustic mass and stiffness matrices, respectively, and $\mathbf{f}_s$ is the structural force vector. The mass coupling matrices are formulated as:

$$\mathbf{M}_{fs}^{pu}(\omega) = \int_{\Gamma_{fs}} \rho_0 \left[1 - \Omega + \Omega \sec(kL)\right] \mathbf{N}_f \left[\mathbf{N}_s\right]^{\mathrm{T}} \mathrm{d}\Gamma \tag{4.38}$$

$$\mathbf{M}_{fs}^{pp}(\omega) = \int_{\Gamma_{fs}} \frac{\Omega \tan(kL)}{\omega c_0} \mathbf{N}_f \left[\mathbf{N}_f\right]^{\mathrm{T}} \mathrm{d}\Gamma \tag{4.39}$$

and the stiffness coupling matrices are formulated as:

$$\mathbf{K}_{fs}^{up}(\omega) = -\int_{\Gamma_{fs}} \left[1 - \Omega + \Omega \sec(kL)\right] \mathbf{N}_s \left[\mathbf{N}_f\right]^{\mathrm{T}} \mathrm{d}\Gamma \tag{4.40}$$

$$\mathbf{K}_{fs}^{uu}(\omega) = -\int_{\Gamma_{fs}} \rho_0 c_0 \omega \Omega \tan(kL) \mathbf{N}_s \left[\mathbf{N}_s\right]^{\mathrm{T}} \mathrm{d}\Gamma \tag{4.41}$$

where $\Gamma_{fs}$ is the interface area. A more detailed description of the derivations can be found in Appendix D. For a panel without resonators, i.e. $\Omega = 0$ or $L = 0$, the matrices $\mathbf{M}_{fs}^{pp}$ and $\mathbf{K}_{fs}^{uu}$ become zero and the matrices $\mathbf{M}_{fs}^{pu}$ and $\mathbf{K}_{fs}^{up}$ change into the standard $\omega$-independent coupling matrices. In that case, the element matrices of the standard acousto-elastic interface elements are obtained.

### 4.3.3 Sound transmission

In this section, an example is presented of normal incidence sound transmission through a panel with resonators. The setup was modelled using an in-house FEM program, running under MATLAB, in which the new interface element was implemented. First, the structural superelements were generated using the commercial FEM program ANSYS. Subsequently, the resulting element matrices were imported into MATLAB where the complete model was assembled.

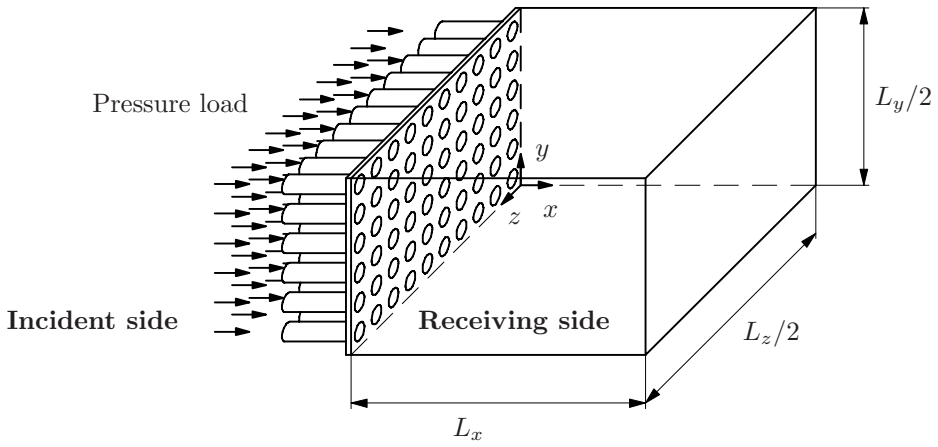


**Figure 4.16**: Panel with resonators with a room on one side (quarter).

### Model

The setup that was modelled is shown in Figure 4.16. A 0.30 × 0.50 m, simply supported panel with resonators is considered. The panel consists of 20 × 12 characteristic areas with dimensions and material properties as listed in Table 4.3. At the incident side, a uniformly distributed pressure load, representing a normal incident plane wave, is applied directly on the interface elements. At the other side of the panel, sound is radiated into a room with five fully sound absorbing walls. The sound absorbing walls were modelled by prescribing a dimensionless impedance of one. The depth of the room is $L_x = 0.25$ m. Since the structure, the acoustic domain, and the pressure load are all symmetric, only a quarter of the system had to be considered.

| **Resonator** | | |
|---|---|---|
| $R$ | 0.0095 | m |
| $L$ | 0.11 | m |
| $t_w$ | 0.0003 | m |
| $t_e$ | 0.0006 | m |

| **Plate** | | |
|---|---|---|
| $L_y$ | 0.30 | m |
| $L_z$ | 0.50 | m |
| $t_p$ | 0.002 | m |
| $b$ | 0.025 | m |

| **Material** | | |
|---|---|---|
| $\rho$ | 2710 | kg/m$^3$ |
| $E$ | 70·10$^9$ | N/m$^2$ |
| $\nu$ | 0.3 | - |

**Table 4.3**: Dimensions and material properties of the panel.

### Sound transmission loss

The sound transmission loss is defined as the ratio between the incident sound power and the transmitted sound power. Usually, from FEM calculations only

total pressures and fluid velocities are known. Therefore, the difficulty is to make a distinction between the incident and the reflected sound waves at the incident side of the panel. Yet, in Section 3.3.1, an approximation method was presented to solve this.

In the present example, however, the pressure load is applied directly to the interface elements, so no fluid elements are present at the incident side. The aforementioned approximation method can therefore not be used. Hence, the incident sound power has to be determined by an alternative approach. This approach is based on a one-dimensional description of the incident sound field. Since the sound field is normal incident, this seems to be a fair approximation[2]. According to equation (4.22), the prescribed pressure $p_l$ at the surface is written in terms of incident and reflected sound waves:

$$p_l = A_l + B_l \tag{4.42}$$

Together with the boundary conditions (4.27) to (4.29) and equations (4.22) and (4.23), the unknown pressure amplitude $B_l$ of the incident sound wave can be solved as a function of the quantities $p_l$ and $v_s$:

$$B_l = \frac{p_l}{2}[1 + \mathrm{i}\Omega_l \tan(kL)] + \frac{\rho_0 c_0 v_s}{2}[1 - \Omega_l + \Omega_l \sec(kL)] \tag{4.43}$$

The pressures $p_l$ are prescribed and the structural velocities $v_s$ result from the FEM analysis[3]. Using equation (2.51), the normal incident sound intensity $\bar{I}_i$ at a certain point on the panel is then calculated by:

$$\bar{I}_i = \frac{\mathrm{Re}(B_l)^2 + \mathrm{Im}(B_l)^2}{2\rho_0 c_0} \tag{4.44}$$

At the receiving side, the transmitted sound intensities were also calculated using equation (2.51). In this case, the pressures, determined at the centroids of the elements, were obtained directly from the FEM analysis. The fluid velocities were determined by using the derivatives of the shape functions to calculate the pressure gradients in normal direction at the centroids of the elements, and subsequently applying Euler's equation. Using equation (2.50), the sound powers at both sides of the panel were obtained by integrating the sound intensities over the surface of the panel. Finally, the sound transmission loss was determined with equation (3.21).

[2]However, if fluid elements are also present on the incident side of the panel and the sound field is random incident, the method presented in Section 3.3.1 is preferred.

[3]If $\Omega_l = 0$ or $L = 0$, the solution converges to the solution for a panel without resonators.

### Results

Figure 4.17 shows the normal incidence sound transmission loss of the considered configuration, calculated both with the reduced FEM model and the one-dimensional analytical model presented in Chapter 2. It is seen that the trends of the two curves are similar. However, the dynamic behaviour of the panel has a large influence on the sound transmission loss. In Figure 4.18, the structural response of the panel is shown. It can be seen that the frequencies of the resonances and anti-resonances of the panel correspond with the frequencies of the peaks and troughs in the transmission loss curve, respectively. To demonstrate the acoustic effect of the resonators, the sound transmission loss is also shown of a panel without resonators, but with the same dynamic properties. The structural behaviour seems to have the same influence on both panels. Since no damping is present in the model, the influence of the eigenfrequencies may be overestimated.

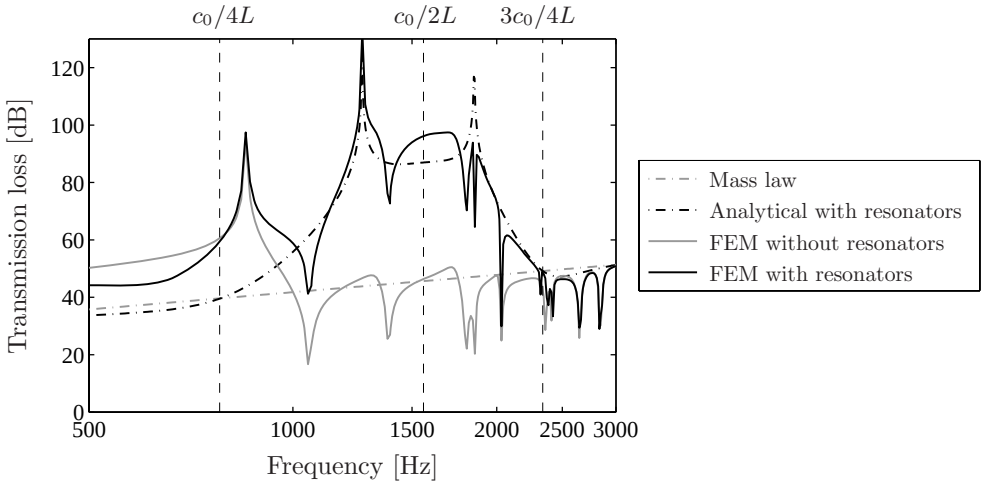


**Figure 4.17**: Normal incidence sound transmission loss.

### Limitations of the model

For the panels with resonators considered in this thesis, the acoustic frequency range of interest is approximately between 500 Hz and 2000 Hz. Because the stiffness of the panels with tubes is relatively low, the modal density of these panels in this range is very high. Attention should therefore be paid to the question of whether the accuracy of the structural model is still sufficient.

For a sufficiently accurate acoustic model, generally at least three quadratic

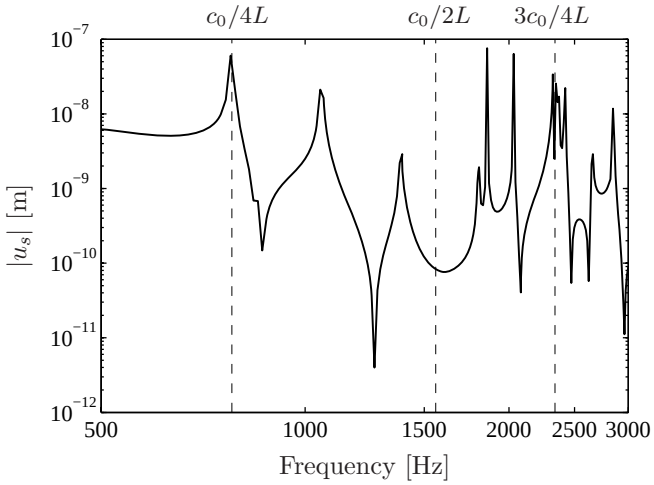


**Figure 4.18**: Normal structural displacements at point ($y$=0.075 mm, $z$=0.125 mm).

elements per wavelength are required. Since the meshes of the structural and acoustic domain have to coincide here, the accuracy of the acoustic model is dependent on the size of the characteristic areas. In this case, the rule of thumb is obeyed for the frequencies $f < c_0/3b$.

## 4.4 Full finite element model

In the formulation of the acousto-elastic interaction for the models previously presented in this chapter, it was assumed that the tube resonators are rigid. No interaction between the deformation of the tubes and the air inside and around the resonators was taken into account. In this section, the influence of the flexibility of the resonators is examined by means of a fully coupled FEM model of one characteristic area, placed in a square impedance tube. Sound radiation as well as sound transmission are considered.

### 4.4.1 Sound radiation

The modelled setup for demonstrating the influence of the flexibility of the resonator on sound radiation is shown in Figure 4.19. In Table 4.4 the dimensions and the material properties of the characteristic area and the impedance tube are listed, respectively. The dimensions and material properties of the resonator are the same as those of the tubes used for the panel with resonators presented in Chapter 5. To investigate the influence of porosity and the flex-

ibility of the resonators, only the width $b$ of the characteristic area and the Young's modulus $E$ were varied.

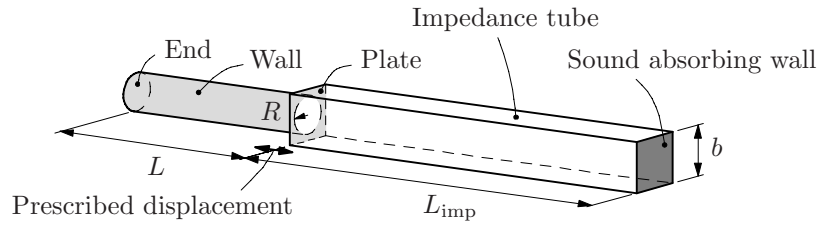


**Figure 4.19**: Setup for sound radiation by a characteristic area into an impedance tube.

| **Dimensions** | | |
|---|---|---|
| $R$ | 0.0122 | m |
| $L$ | 0.109 | m |
| $t_p$ | 0.002 | m |
| $t_w$ | 0.00028 | m |
| $t_e$ | 0.0006 | m |
| $L_{\text{imp}}$ | 0.10 | m |

| **Material** | | |
|---|---|---|
| $\rho$ | 2710 | kg/m$^3$ |
| $\nu$ | 0.3 | - |

**Table 4.4**: Dimensions and material properties of the modelled setup.

### Model

The setup was modelled using the FEM program Ansys. The plate and the resonator were meshed with linear shell elements (three-node SHELL63 elements) and the air inside the resonator and in the impedance tube was modelled by linear tetrahedral fluid elements (four-node FLUID30 elements). An example of the mesh is shown in Figure 4.20. The structure and the air were fully coupled. At the end of the impedance tube, full sound absorption was imposed by prescribing a dimensionless impedance of one. Excitation took place by prescribing a harmonic unit displacement at the edges of the plate. Up to the so-called cut-off frequency, the sound field in the impedance tube approximates a one-dimensional sound field. For a square tube, this frequency is $f = c_0/2b$. For the setup considered in this section, this frequency is far above the frequency range of interest. The insertion loss could therefore be calculated in the same way as described in Section 2.4.1.

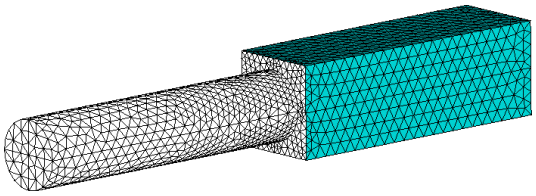

**Figure 4.20**: FEM mesh of characteristic area and air in the impedance tube.

### Results

The structure of the characteristic area consists of three parts: the plate, the resonator walls and the resonator end. In the simulations, these parts were considered to be either flexible ($E = 70 \cdot 10^9$ N/m$^2$) or rigid ($E = 70 \cdot 10^{15}$ N/m$^2$), successively. The numerical results are compared with the results of the one-dimensional analytical model as presented in Chapter 2, where the entire characteristic area was assumed to be rigid. The effective resonator length (see Section 2.5) that was used in the latter model is $L = 0.1115$ m.

In Figure 4.21 the insertion loss is shown for characteristic areas with different flexible and rigid parts. For an entirely rigid characteristic area, the agreement with the results of the one-dimensional analytical model is good (see Figure 4.21(a)). If only the plate, only the resonator walls or only the resonator end are flexible, there are hardly any differences with the entirely rigid case. The same holds if both the plate and the resonator end are flexible. These results are not shown in Figure 4.21.

In the case where both the plate and the resonator walls are flexible, discrepancies appear between the one-dimensional analytical model and the FEM model (see Figure 4.21(b)). These discrepancies increase with increasing frequencies and decreasing porosity. Due to the inertia forces that are caused by the prescribed displacement at the edges of the characteristic area and the pressure inside the resonator, the resonator tube deforms in axial direction (see Figure 4.22(a)). Also the plate deforms, which means that the axial structural velocity varies over the surface. Both these matters cause differences in amplitude between the axial structural velocities of the plate and the resonator end, while in the one-dimensional analytical model it was assumed that these velocities are uniform. Figures 4.23 and 4.24 show the ratios of the velocities $u_e$ at the centre of the resonator end and $u_p$ at one of the corners of the plate. It can be seen that the differences increase with increasing frequencies and decreasing porosity.

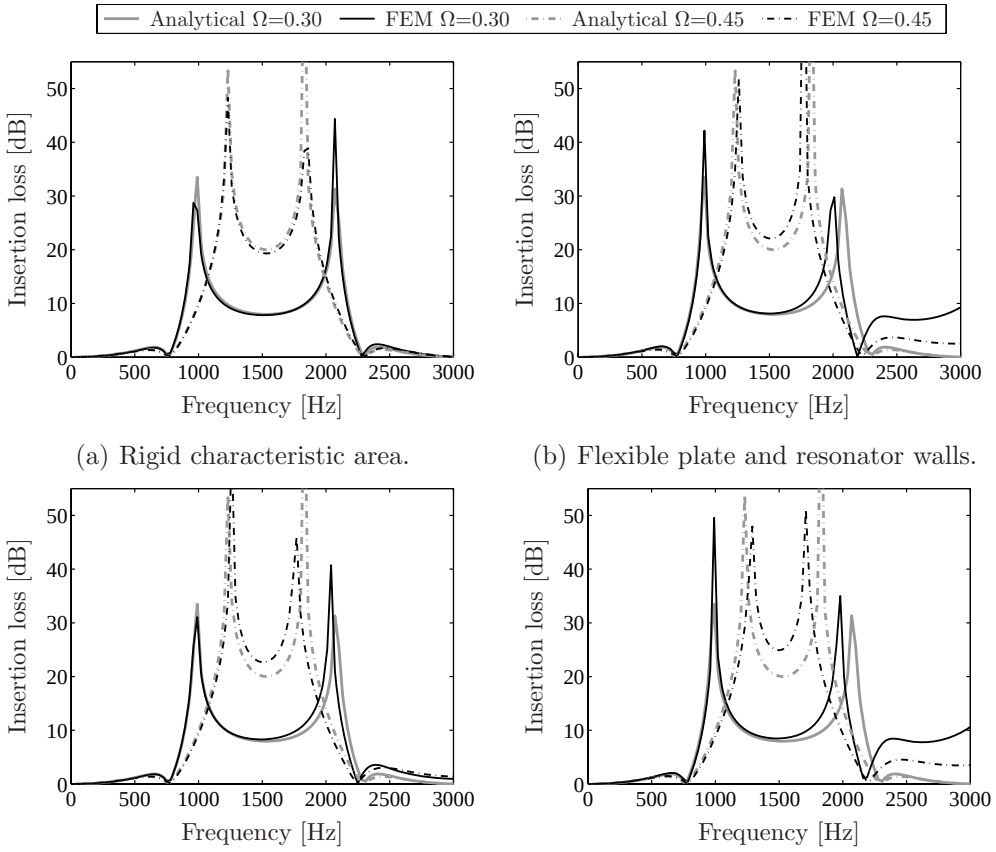


(a) Rigid characteristic area.

(b) Flexible plate and resonator walls.

(c) Flexible resonator.

(d) Flexible characteristic area.

**Figure 4.21**: Insertion loss for characteristic areas with different flexible and rigid parts and different porosities.

Smaller but similar effects are observed if both the walls and the end of the resonator are flexible (see Figure 4.21(c)). However, the differences in velocity are smaller and the discrepancies increase less with frequency. An example of the deformation shape is shown in Figure 4.22(b).

If the characteristic area is entirely flexible, the effects of the deformations of all parts are combined (see Figure 4.22(c)) and the differences with the one-dimensional analytical model are the largest (see Figure 4.21(d)). Nevertheless, the trends of the curves remain reasonably the same.

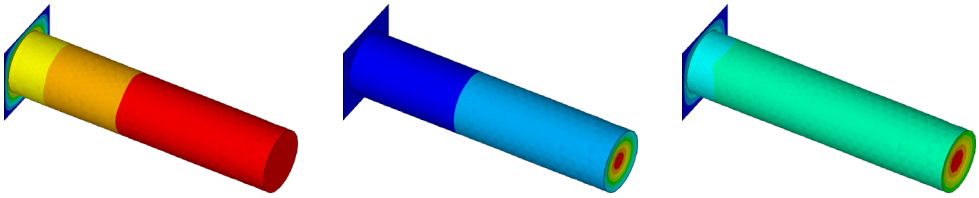

(a) Flexible plate and resonator walls.

(b) Flexible resonator.

(c) Flexible characteristic area.

**Figure 4.22**: Deformation shapes at 2000 Hz for characteristic areas with different flexible and rigid parts ($\Omega$=0.45).

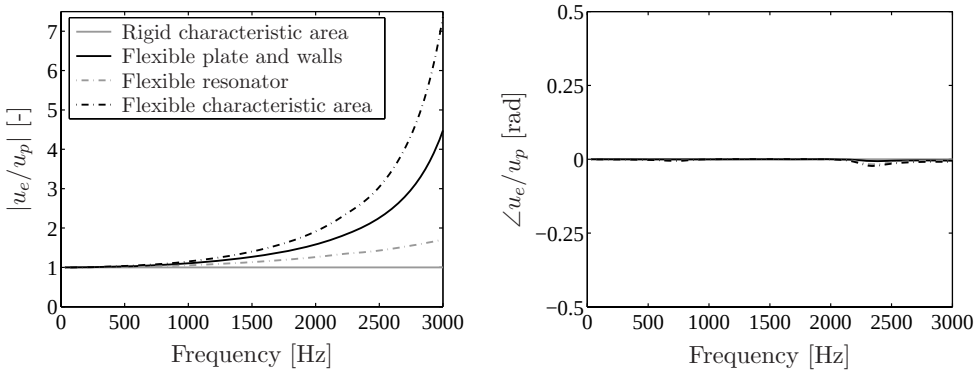


(a) Magnitude.

(b) Phase.

**Figure 4.23**: Ratio $u_e/u_p$ of the axial structural velocities of the centre of the resonator end and one of the corners of the plate ($\Omega$=0.30).

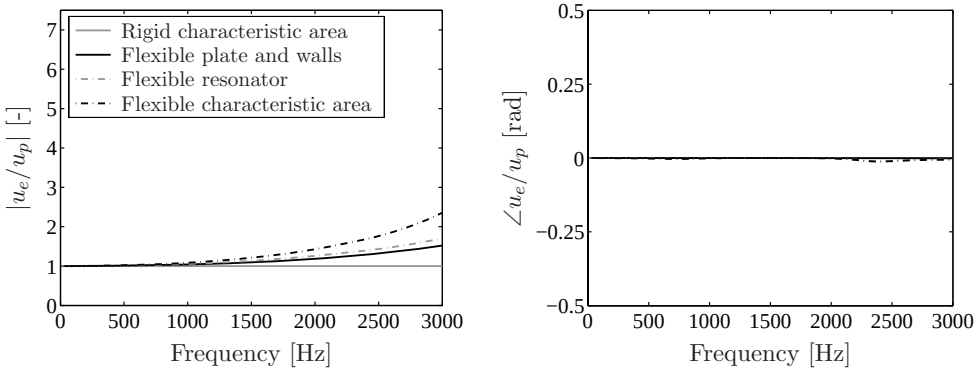


(a) Magnitude. (b) Phase.

**Figure 4.24**: Ratio $u_e/u_p$ of the axial structural velocities at the centre of the resonator end and at one of the corners of the plate ($\Omega$=0.45).

### 4.4.2 Sound transmission

The modelled setup for demonstrating the influence of the flexibility of the resonator on sound transmission is shown in Figure 4.25. The dimensions and material properties are listed in Table 4.4. The length of the impedance tube at the incident side is $L_{\text{impI}} = 0.15 + L$. The length of the impedance tube at the receiving side is $L_{\text{impII}} = L_{\text{imp}}$.

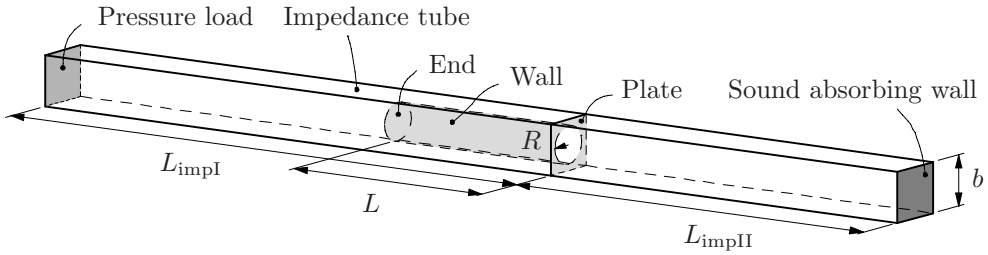


**Figure 4.25**: Setup for sound transmission through a characteristic area.

#### Model

The setup is modelled in the same way as the setup for sound radiation. Only the excitation of the structure is different now. Acoustic excitation is applied by prescribing a uniformly distributed pressure at one end of the

impedance tube (see Figure 4.25). The boundaries of the characteristic area are unconstrained.

### Sound transmission loss

Because the sound field in the impedance tube approximates a one-dimensional sound field, the sound transmission loss can be calculated as described below [46]. Using equation (4.22), the pressures at both sides of the characteristic area are expressed as a function of $x$ (see Figure 4.26). As a result of the FEM analysis, the pressures $p_{\mathrm{I}}$, $p_{\mathrm{II}}$, $p_{\mathrm{III}}$ and $p_{\mathrm{IV}}$ at four locations in the impedance tube are then used to determine the amplitudes of the backward and forward travelling sound waves[4]:

$$A_1 = \frac{\mathrm{i}\left(p_{\mathrm{II}}e^{-\mathrm{i}kx_{\mathrm{I}}} - p_{\mathrm{I}}e^{-\mathrm{i}kx_{\mathrm{II}}}\right)}{2\sin\left[k(x_{\mathrm{I}} - x_{\mathrm{II}})\right]} \qquad B_1 = \frac{\mathrm{i}\left(p_{\mathrm{I}}e^{\mathrm{i}kx_{\mathrm{II}}} - p_{\mathrm{II}}e^{\mathrm{i}kx_{\mathrm{I}}}\right)}{2\sin\left[k(x_{\mathrm{I}} - x_{\mathrm{II}})\right]} \tag{4.45a}$$

$$A_2 = \frac{\mathrm{i}\left(p_{\mathrm{IV}}e^{-\mathrm{i}kx_{\mathrm{III}}} - p_{\mathrm{III}}e^{-\mathrm{i}kx_{\mathrm{IV}}}\right)}{2\sin\left[k(x_{\mathrm{III}} - x_{\mathrm{IV}})\right]} \qquad B_2 = \frac{\mathrm{i}\left(p_{\mathrm{III}}e^{\mathrm{i}kx_{\mathrm{IV}}} - p_{\mathrm{IV}}e^{\mathrm{i}kx_{\mathrm{III}}}\right)}{2\sin\left[k(x_{\mathrm{III}} - x_{\mathrm{IV}})\right]} \tag{4.45b}$$

With these pressure amplitudes, the transmission loss is subsequently calculated as described in Section 2.4.2.

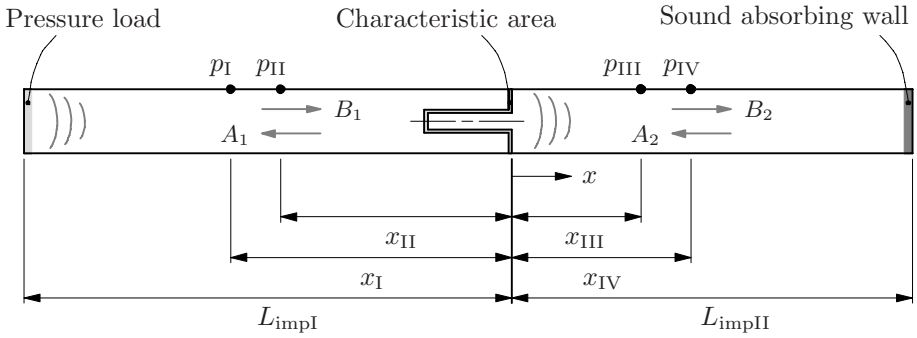


**Figure 4.26**: Coordinate system for determining pressure amplitudes.

[4]Since the end of the impedance tube is fully sound absorbing, pressure amplitude $A_2$ equals zero here.

**Results**

In Figure 4.27 the sound transmission loss is shown for characteristic areas with different flexible and rigid parts and different porosities[5]. For an entirely rigid characteristic area, the agreement with the results of the one-dimensional analytical model is good (see Figure 4.27(a)). If only the plate is flexible, there are again hardly any differences compared with the entirely rigid case. These results are not shown in Figure 4.27.

However, if only the walls or only the end of the resonator are flexible, the differences become more pronounced (see Figures 4.27(b) and 4.27(c)). The flexibility of the structure has much more influence now than in the case of sound radiation as presented in the previous section. If the porosity is $\Omega = 0.30$, the differences are rather small, but if the porosity is $\Omega = 0.45$, the sound transmission loss is reduced considerably. Also, the peaks in the transmission loss curve disappear. The discrepancies are again mainly caused by the differences in amplitude between the axial structural velocities of the plate and the resonator end (see Figures 4.28 and 4.29). However, in the case of sound transmission, these effects are the largest around the frequency for which the acoustic wavelength equals half of the length of the resonator, while for sound radiation they increase with frequency. If the characteristic area is entirely flexible, the effects of the deformations of all parts are combined and the differences with the one-dimensional analytical model are the largest (see Figure 4.27(d)). In some cases the sound transmission loss is increased, in other cases the sound transmission loss is reduced.

[5]The porosity was varied by varying the width $b$ of the characteristic areas. The mass of the configurations with the different porosities was therefore slightly different.

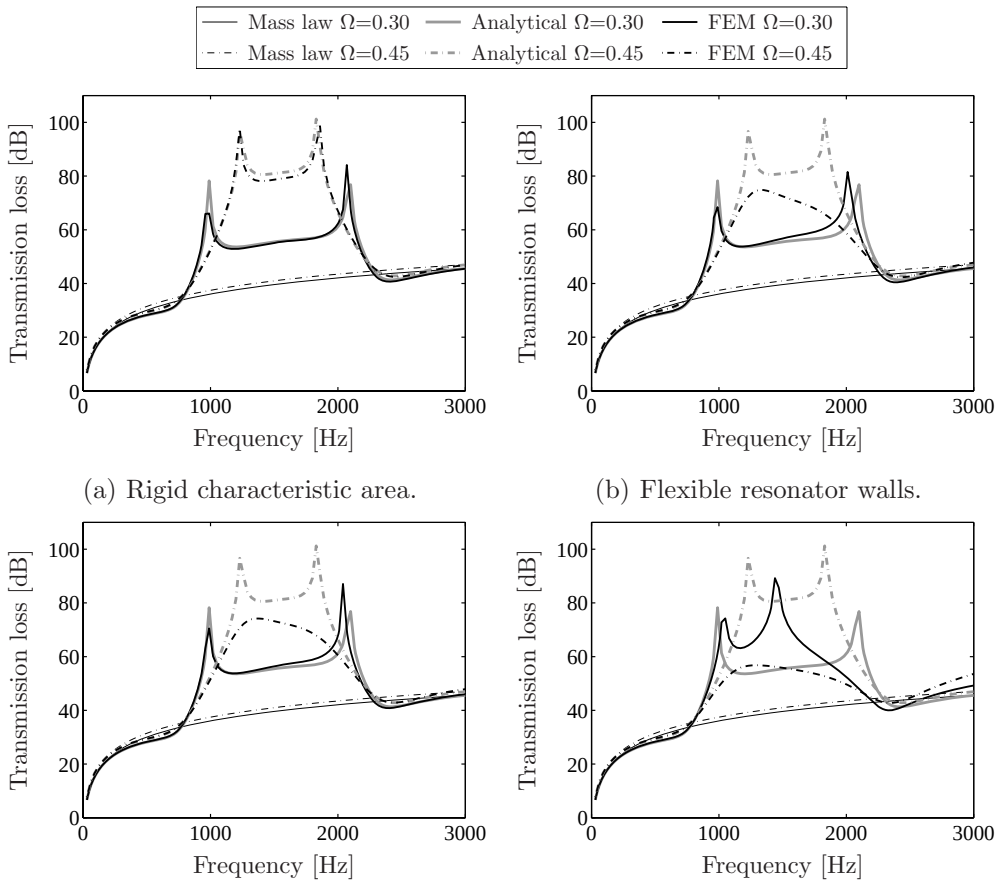


(a) Rigid characteristic area.

(b) Flexible resonator walls.

(c) Flexible resonator end.

(d) Flexible characteristic area.

**Figure 4.27**: Transmission loss for characteristic areas with different flexible and rigid parts and different porosities.

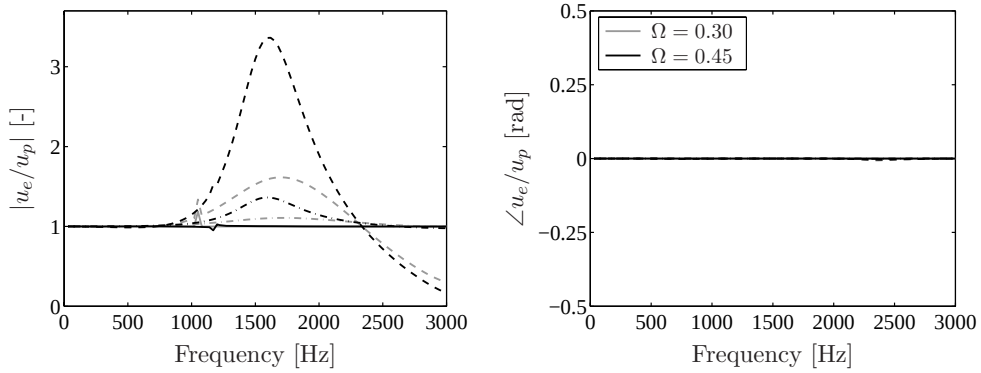


(a) Magnitude. (b) Phase.

**Figure 4.28**: Ratio $u_e/u_p$ of the axial structural velocities of the centre of the resonator end and one of the corners of the plate - rigid characteristic area (solid lines), flexible resonator walls (dash-dotted lines), and flexible resonator end (dashed lines).

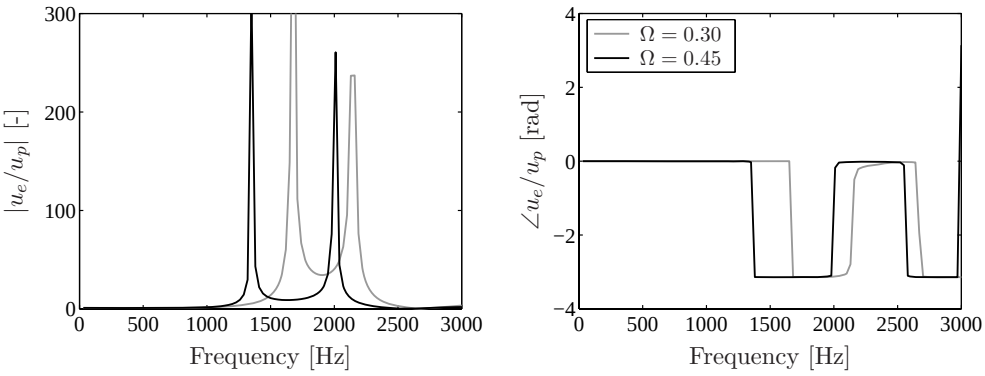


(a) Magnitude. (b) Phase.

**Figure 4.29**: Ratio $u_e/u_p$ of the axial structural velocities at the centre of the resonator end and at one of the corners of the plate - flexible characteristic area.

## 4.5 Concluding remarks

In this chapter, three different numerical models were presented, which include the boundedness and flexibility of panels with resonators. These methods can be used to model more realistic setups and to investigate the limitations of the (semi-)analytical models as presented in the previous chapters.

Using the Rayleigh integral method, free-field sound radiation of a baffled panel with resonators was considered. A comparison was made with an infinitely large panel with resonators, modelled as presented in Chapter 2. In the case of a rigid panel, the radiated sound power is only influenced by the boundaries of the panel if the acoustic wavelength is large compared to the dimensions of the panel. At higher frequencies, the influence of the boundaries is negligible.

Another model, based on the FEM, was presented to predict the transmission of sound through panels with resonators with more complex geometries and different boundary conditions. Because a fully coupled model of the structure and the air inside and around the resonators is computationally expensive, a reduced model was developed. A new type of interface element was formulated, which not only enables coupling between the structural part of the model and the air behind and in front of the panel, but also includes the acoustic behaviour of the resonators. Normal incidence transmission loss calculations for a specific resonator panel configuration showed similar trends as the results obtained with the one-dimensional analytical model presented in Chapter 2. The dynamic behaviour of the panel has a large influence on the sound transmission loss. Structural resonances cause a decrease in sound transmission loss, while, on the other hand, anti-resonances cause an increase.

In the formulation of the acousto-elastic interaction for the previous presented models, it was assumed that the tube resonators are rigid. No interaction between the deformation of the tubes and the air inside and around the resonators was taken into account. However, a fully coupled FEM model of one characteristic area, placed in a square impedance tube, showed that local deformations of the plate and the resonator can have a large influence on the radiated sound power or sound transmission loss. For relatively large deformations, the flexibility of the structure can thus not be neglected.

# Chapter 5

# Experimental validation

## 5.1 Introduction

In the previous chapters, different models were presented to predict the transmission of sound through panels with resonators. To reduce computation time and make them into fast analysis tools for optimisation and design, some assumptions and simplifications were made. To verify whether these assumptions and simplifications are valid, sound transmission loss measurements were performed on two resonator panels of different configurations: a panel with tubes and a sandwich panel. The last configuration can be manufactured easily by perforating one of the skin panels of a common honeycomb sandwich panel (see Figure 5.1). The sound transmission loss was measured using the sound intensity method.

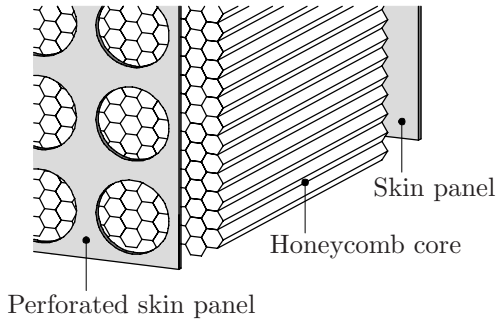


**Figure 5.1**: Honeycomb sandwich panel with resonators.

In Section 5.2, the experimental setup and the experimental method are presented. Next, in Section 5.3, the experimental results are discussed. First,

the effect of the tube resonators is analysed by comparing the measured sound transmission with the mass law. Subsequently, a comparison is made between the experimental results and the results obtained with the numerical and (semi-)analytical models presented in the previous chapters.

## 5.2 Experimental procedure

The traditional method for measuring the sound transmission loss of a panel is the two-room method [14, 26]. For this method, two reverberation rooms are used, which are separated by the panel under investigation. In the sending room a diffuse sound field is generated by a sound source and the spatially averaged sound pressure levels in both rooms are determined by two moving microphones. Besides the sound pressure levels, the reverberation time of the receiving room also has to be measured.

Instead of a reverberation room, a less reverberant (preferably anechoic) room can also be used at the receiving side [14, 26]. In that case, the radiated sound power in the receiving room is measured directly with a sound intensity probe. An advantage of this so-called sound intensity method is that it makes it possible to evaluate the relative, local contributions of different parts of a panel to the total sound transmission.

The sound transmission loss of the panels presented in this work were measured by means of the sound intensity method.

### 5.2.1 Experimental setup

The experiments were performed in a laboratory setup at the National Aerospace Laboratory NLR [29, 52, 53]. A schematic overview of the setup is depicted in Figure 5.2. The panel was mounted between the reverberation room and a semi-anechoic receiving room by bolting it between two wooden frames with rubber strings (see Figure 5.3(a) and Appendix E). Because of the large thickness of the sandwich panels, flanking noise had to be suppressed by covering the sides of these panels with lead (see Figure 5.3(b)).

In the reverberation room, four speakers placed near the corners were fed with white noise to generate sound in the frequency range of 500-5600 Hz. Another speaker, a so-called dodecahedron, was used to generate sound below 500 Hz. During the measurements, this sound source was located at position 3, as marked in Figure 5.2. The sound pressure level in the reverberation room was measured with a microphone on two rotating booms, scanning the surface of a sphere. The intensity level of the sound that was transmitted through the panel via a niche into the semi-anechoic room was measured with

a sound intensity probe. The sound intensity was measured over the 1.00 × 1.00 m cross-section of the niche at a distance of about 0.74 m from the panel. The niche has an average depth of 0.87 m and the volume of the semi-anechoic room is about 205 $m^3$. Additional information on the dimensions of the reverberation room, the niche, and the possible positions of the low frequency sound source can be found in Appendix E. A detailed list of the measurement equipment is also included.

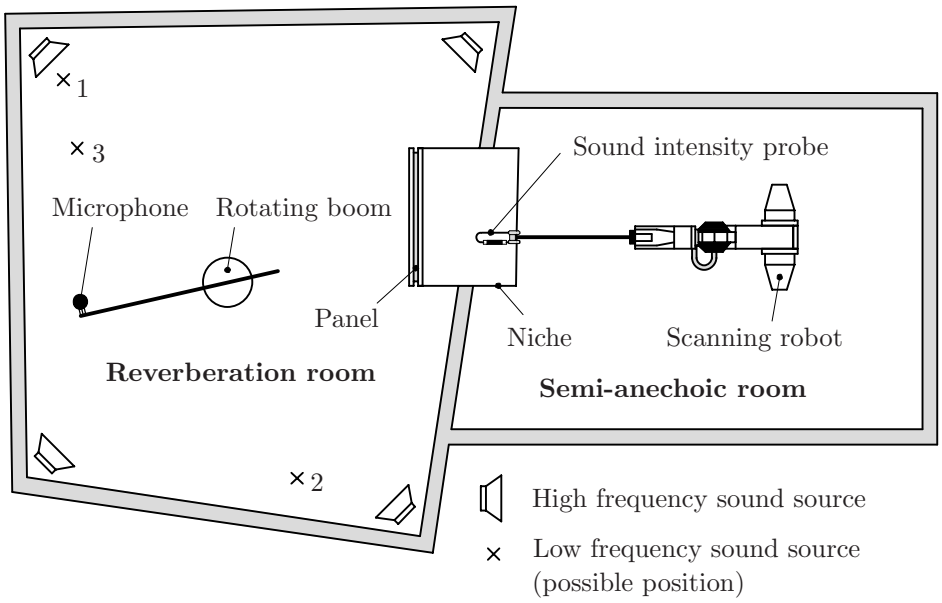


**Figure 5.2**: Experimental setup for sound transmission loss measurements.

To determine the radiated sound power in the semi-anechoic room, the sound intensity measured normally to the panel surface can be spatially averaged using two standardised procedures: the discrete point method (ISO 9614-1) or the scanning method (ISO 9614-2). For the experiments presented in this thesis, the scanning method was used. For each panel, the sound transmission loss was determined by taking the average of a vertical scan and a horizontal scan (see Figure 5.4). Part of the measurements was performed by a (silent) robot and part of the measurements was performed manually. The scanning speed was approximately 75 mm/s. Measurements were also performed using the discrete point method, but the differences were shown to be relatively small.

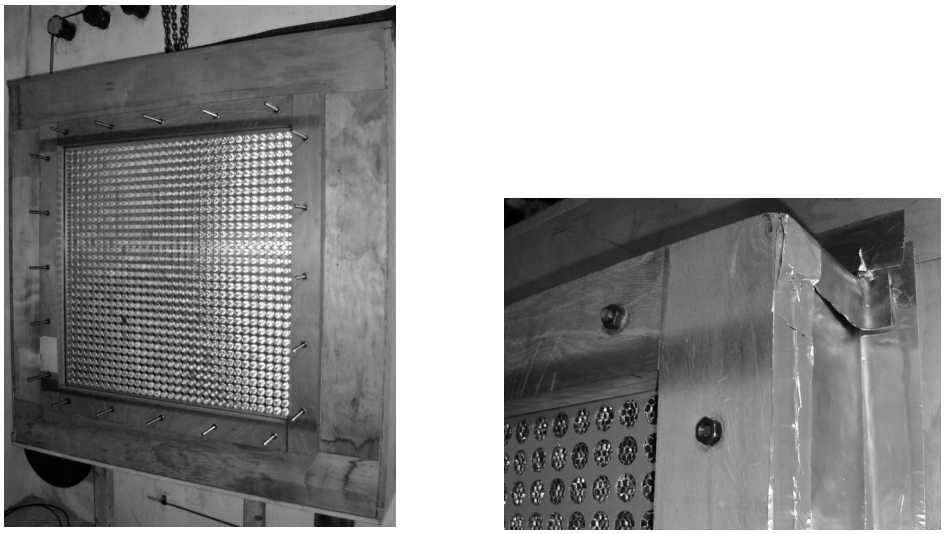

(a) Panel in the experimental setup. (b) Flanking noise suppression.

**Figure 5.3**: Panel in the experimental setup (incident side) and lead strips for flanking noise suppression of the sandwich panels.

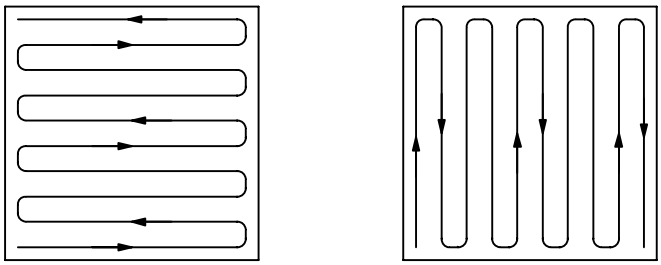


**Figure 5.4**: Scanning patterns for sound power measurement by the scanning method.

### 5.2.2 Sound intensity method

As far as possible and appropriate, the sound transmission loss was measured according to the sound intensity method specified in ISO 15186-1. The measurements were performed in a frequency range of one-third octave bands (1/3OBs) with centre frequencies ranging from 100 to 5000 Hz. In this section, the principles of the sound intensity method are further explained.

### Sound transmission loss

As mentioned before, the sound transmission loss is defined as the ratio of the incident sound power $\bar{W}_i$ and the transmitted sound power $\bar{W}_t$, in logarithmic form:

$$TL = 10 \log_{10} \left( \frac{\bar{W}_i}{\bar{W}_t} \right) \tag{5.1}$$

From a sound intensity measurement, the sound power $\bar{W}$ is obtained by:

$$\bar{W} = (\bar{I}_n)_{\text{avg}} \, S \tag{5.2}$$

where $S$ is the scanned surface area and $(\bar{I}_n)_{\text{avg}}$ is the spatially averaged sound intensity in the direction $n$ normal to that surface area. Using this definition, the sound transmission loss can also be written as:

$$TL = 10 \log_{10} \left[ \frac{(\bar{I}_i)_{\text{avg}}}{(\bar{I}_t)_{\text{avg}}} \right] \tag{5.3}$$

where $(\bar{I}_i)_{\text{avg}}$ and $(\bar{I}_t)_{\text{avg}}$ are the spatially averaged incident and transmitted sound intensities normal to the surface area $S$, respectively. In terms of sound intensity levels, the sound transmission loss can also be written as:

$$TL = (L_I)_{\text{avg } i} - (L_I)_{\text{avg } t} \tag{5.4}$$

where $(L_I)_{\text{avg } i}$ is the spatially averaged incident sound intensity in the reverberation room and $(L_I)_{\text{avg } t}$ is the sound intensity level normal to and averaged over the measuring surface $S$ in the receiving room. The general definition of the sound intensity level $L_I$ is:

$$L_I = 10 \log_{10} \left( \frac{\bar{I}_r}{\bar{I}_{\text{ref}}} \right) \tag{5.5}$$

where $\bar{I}_r$ is the sound intensity in an arbitrary direction $r$ and $\bar{I}_{\text{ref}}$ is the reference sound intensity:

$$\bar{I}_{\text{ref}} = \frac{p_{\text{ref}}^2}{\rho_0 c_0} = 10^{-12} \text{ Wm}^{-2} \tag{5.6}$$

$p_{\text{ref}} = 2 \cdot 10^{-5}$ Pa is the reference pressure of a plane wave propagating in a free field.[1] As was also seen in the previous chapters, the incident sound

[1] For plane and spherically propagating waves, the sound intensity and the root mean squared pressure are related by $\bar{I}_r = p_{\text{rms}}^2 / \rho_0 c_0$.

intensity cannot be measured directly. However, for a diffuse sound field, which approximates the sound field in the reverberation room, the intensity of the sound incident on the panel can be determined by measuring sound pressure. In a diffuse sound field, sound is reflected so many times that it travels in all directions with equal magnitude and probability [9]. Consequently, the sound intensity $\bar{\mathbf{I}}$ at any point in the field is zero. However, in theory, a so-called one-sided sound intensity $\bar{I}_r$ in an arbitrary direction $r$ can be defined. The one-sided sound intensity is the intensity of the sound passing through a plane of unit area from one side (i.e. the sound intensity in one direction, ignoring the equal and opposite component). For a diffuse sound field, the relation between the root mean squared pressure $p_{\text{rms}}$ and the one-sided sound intensity is as follows [6]:

$$\bar{I}_r = \frac{p_{\text{rms}}^2}{4\rho_0 c_0} \tag{5.7}$$

By substituting this expression into equation (5.5) and using equation (5.6), the incident sound intensity level in the reverberation room can be written as:

$$(L_I)_{\text{avg } i} = (L_p)_{\text{avg } i} - 6 \text{ dB} \tag{5.8}$$

where $(L_p)_{\text{avg } i}$ is the spatially averaged sound pressure level in the reverberation room. The sound pressure level $L_p$ is defined as:

$$L_p = 10 \log_{10} \left( \frac{p_{\text{rms}}^2}{p_{\text{ref}}^2} \right) \tag{5.9}$$

Substituting equation (5.8) into equation (5.4), finally gives the following expression for the sound transmission loss:

$$TL = (L_p)_{\text{avg } i} - (L_I)_{\text{avg } t} - 6 \text{ dB} \tag{5.10}$$

The spatially averaged sound pressure level $(L_p)_{\text{avg } i}$ in the reverberation room is measured with the microphone on the two rotating booms, and the spatially averaged sound intensity level $(L_I)_{\text{avg } t}$ in the receiving room is measured with the sound intensity probe.

**Sound intensity probe**

The sound intensity probe that is used here consists of two closely spaced microphones, mounted face-to-face and separated by a solid spacer (see Figure 5.5). By means of the two-microphone method, an estimate of the sound intensity is found at the centre of the spacer [21].

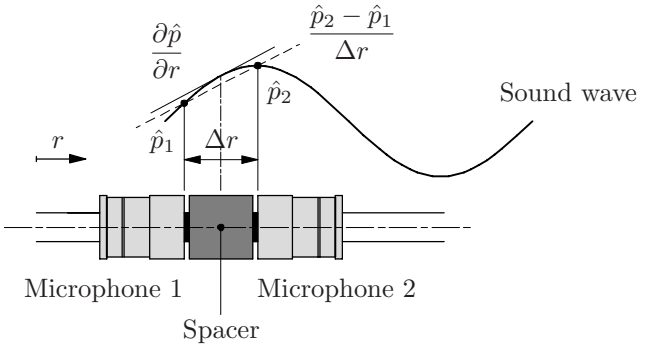


**Figure 5.5**: Approximation of the pressure gradient by a sound intensity probe.

According to equation (2.51) the sound intensity is the time-averaged product of the pressure and the fluid velocity. The fluid velocity perturbation $\hat{v}_r(t)$ in direction $r$ is related to the pressure gradient by the linearised Euler equation:

$$\rho_0 \frac{\partial \hat{v}_r(t)}{\partial t} = -\frac{\partial \hat{p}(t)}{\partial r} \tag{5.11}$$

In the present method, the fluid velocity is estimated by using a finite difference approximation of the pressure gradient (see Figure 5.5). Furthermore, the pressure at the centre of the spacer is approximated by the average pressure of the two microphones. These two approximations can be written as:

$$\frac{\partial \hat{p}}{\partial r} \approx \frac{\hat{p}_2 - \hat{p}_1}{\Delta r} \qquad\qquad \hat{p} \approx \frac{\hat{p}_1 + \hat{p}_2}{2} \tag{5.12}$$

where $\Delta r$ is the spacer length, and $\hat{p}_1$ and $\hat{p}_2$ are the pressures measured by the two microphones [10, 19]. In practice, the time domain signals are usually transformed to the frequency domain using a fast Fourier transform (FFT). Using equation (5.11), the estimation for the fluid velocity then becomes:

$$v_r \approx \frac{\mathrm{i}}{\omega \rho_0} \frac{p_2 - p_1}{\Delta r} \tag{5.13}$$

So with equation (2.51), the sound intensity in direction $r$ can be written as:

$$\bar{I}_r \approx -\frac{\mathrm{Im}(G_{12})}{\omega \rho_0 \Delta r} \tag{5.14}$$

where $G_{12} = p_1 p_2^*/2$ is the one-sided cross-spectrum between the two pressure signals.

The high frequency limit of the sound intensity probe is determined by the finite difference approximation error. The approximation of the pressure

gradient is only accurate if the acoustic wavelength is large compared to the spacer length. As a rule of thumb, the acoustic wavelength must be larger than six times the spacer length for the accuracy to be within 1 dB [9]. For the spacer lengths of $\Delta r = 50$ mm and $\Delta r = 12$ mm, which were used in the present work, the high frequency limits are approximately 1143 Hz and 4764 Hz, respectively.

A small time delay between the two microphone channels introduces a small phase change, which is called a phase mismatch error. This phase mismatch error imposes a low frequency limit on the sound intensity probe. The phase mismatch is quantified by the so-called pressure-residual intensity index, which is the difference between the sound pressure level and the sound intensity level when the microphones are exposed to the diffuse sound field of an intensity calibrator. Ideally, the measured sound intensity should then be zero.

Another important indicator for the accuracy of measurements by the sound intensity probe is the pressure-intensity index $\delta_{pI}$. This quantity is defined as the difference between the sound pressure level and sound intensity level normal to the measuring surface, at the same point. The pressure-intensity index is a function of the form of the sound field, the position and orientation of the probe in that sound field, and the phase mismatch. For a sound reflecting test specimen, the pressure-intensity index should be $\delta_{pI} < 10$ dB and for a test specimen with a sound absorbing surface in the receiving room, it should be $\delta_{pI} < 6$ dB.

More details about possible errors inherent to the sound intensity method can, for example, be found in the work of Fahy [21] and Jacobsen [33].

### 5.2.3 Diffusivity

The volume of the reverberation room is approximately 33 $m^3$, resulting in a diffuse sound field for frequencies of about 500 Hz and higher [53]. To determine the measurement error due to insufficient diffusivity of the sound field below 500 Hz, sound transmission loss measurements were performed for three different positions of the low frequency sound source (see Figure 5.2 and Appendix E). Figure 5.6 shows the results of an arbitrary panel. The sound transmission loss is presented in one-third octave bands. Below the 160 Hz 1/3OB the accuracy is poor. From the 160 Hz 1/3OB to the 315 Hz 1/3OB the differences are within 2.8 dB and above the 315 Hz 1/3OB the discrepancies are within 1.6 dB. Since the main focus for the test panels is on the frequency range of 500 Hz and higher, this accuracy is considered to be sufficient. The other measurements presented in this section were performed with the low frequency sound source located at position 3 (see Figure 5.2) and a sound

intensity probe with a microphone spacing of $\Delta r = 12$ mm.

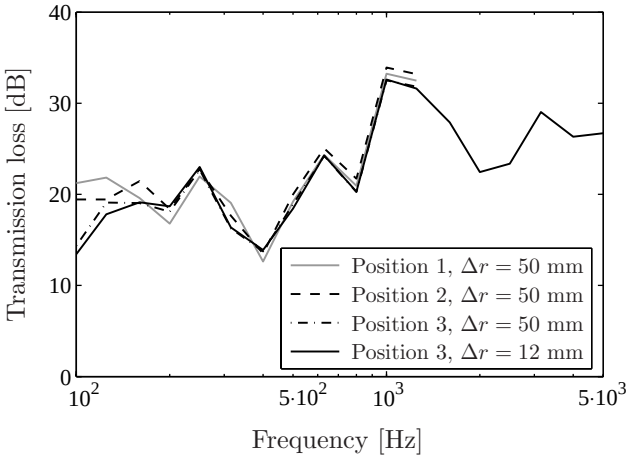


**Figure 5.6**: Measured sound transmission loss of an arbitrary panel for different positions of the low frequency sound source and different spacer lengths.

### 5.2.4 Test panels

In the experimental setup, two resonator panels of different configurations were tested: a panel with tubes and a sandwich panel [27]. The panel with tubes consists of a 2.0 mm thick, perforated aluminium plate with aluminium tubes attached to it. The second panel is an aluminium honeycomb sandwich panel with one of the skin panels perforated (see Figure 5.1). Photos of both panels are shown in Figures 5.7 and 5.8. The resonators of the two panels were tuned to achieve a large increase in transmission loss in the frequency range of 1000-2000 Hz. In Table 5.1 the dimensions and the mass of the characteristic areas are shown. Since the sandwich panel is relatively stiff, its first eigenfrequency is relatively high and the coincidence frequency is relatively low. Therefore, the sound transmission characteristics may differ from those of a thin flat plate. To verify whether the results can still be compared with the mass law, an unperforated honeycomb sandwich panel, here referred to as sandwich reference panel, was also tested. Both sandwich panels consist of a 109 mm thick 2.3-1/4-10 (5052)[2] Hexweb® aluminium honeycomb core and two 0.56 mm thick aluminium skin panels. The dimensions of all panels are $1.08 \times 1.08$ m. The size of the apertures in the wooden frames for the suspension (see Appendix E), i.e. the size of the measuring surface, is $1.00 \times 1.00$ m.

[2]Density [lb/ft$^3$] - cell size (two times the inradius) [inches] - nominal foil thickness [$10^{-4}$ inches] (alloy type).

| | $L$ [m] | $R$ [m] | $b$ [m] | $\Omega$ [-] | $\bar{m}$ [kg/m$^2$] |
|---|---|---|---|---|---|
| Panel with tubes | 0.109 | 0.0122 | 0.0305 | 0.50 | 9.74 |
| Sandwich panel | 0.110 | 0.0125 | 0.0315 | 0.49 | 6.88 |
| Sandwich reference panel | - | - | - | - | 8.13 |

**Table 5.1**: Dimensions and mass of the characteristic areas.

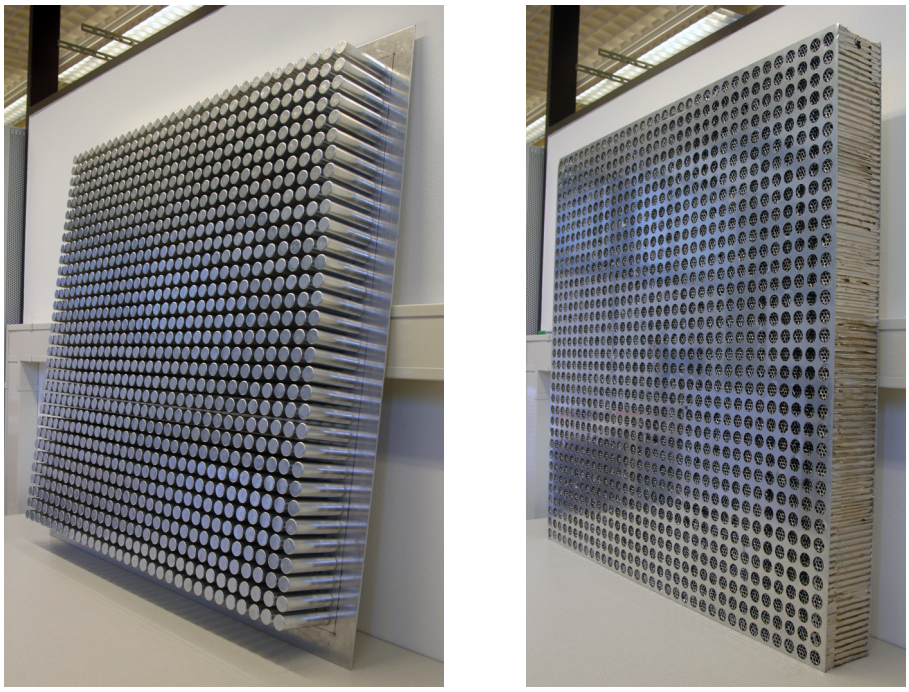

(a) Panel with tubes.

(b) Sandwich panel.

**Figure 5.7**: Photos of test panels with resonators.

## 5.3 Experimental results

In this section, the results of the sound transmission loss measurements are presented. To demonstrate the effect of the resonators, the results are first compared with the mass law, i.e. the sound transmission loss of a flat panel with the same mass, but without resonators. Subsequently, a comparison is made between the experimental results and the results obtained with the models presented in the previous chapters.

(a) Panel with tubes. (b) Sandwich panel.

**Figure 5.8**: Details of test panels with resonators.

### 5.3.1 Comparison with mass law

Previously, normal incidence sound transmission through an infinitely large, isotropic panel without resonators was described by equation (2.58). For a panel of finite dimensions, the normal incidence mass law is corrected as follows [3, 41]:

$$TL = 10\log_{10}\left[1+\left(\frac{\bar{m}\omega}{2\rho_0 c_0}\right)^2\right] - 10\log_{10}(2\sigma_d) \tag{5.15}$$

where $\sigma_d$ is the radiation efficiency. Generally, the radiation efficiency is defined as the ratio between the average acoustic power radiated per unit area of a vibrating surface and the average acoustic power radiated per unit area of a piston that is vibrating with the same average mean square velocity at a frequency for which $kR \gg 1$ (where R is the effective radius of the piston) [20]. In the case of sound transmission through a panel, the radiation efficiency is dependent on the size of the panel and on the angle of incidence. For a flat, square plate, surrounded by an infinite rigid baffle, excited by a diffuse sound field, the radiation efficiency can be approximated by [41]:

$$\sigma_d = \frac{1}{2}\left[0.2 + \ln\left(k\sqrt{S}\right)\right] \tag{5.16}$$

where $S$ is the area of the radiating surface of the test panel.

In Figures 5.9, 5.10 and 5.11 the measured sound transmission loss of the test panels is compared with the mass law. The panel with tubes was measured with the resonator openings at the receiving side and the sandwich panel was measured with the resonator openings at the incident side. Later, it will be shown that the orientation of the panel does not have a very large influence.

Figure 5.9 shows that between the 400 Hz 1/3OB and the 1600 Hz 1/3OB, the sound transmission loss of the panel with tubes is larger than the mass law. Maximum increases of 7.1 dB in the 800 Hz 1/3OB and 3.9 dB in the 1600 Hz 1/3 OB are obtained. However, from the 2000 Hz 1/3OB, the transmission loss is smaller than the mass law. A maximum decrease of 15 dB is observed in the 5000 Hz 1/3OB.

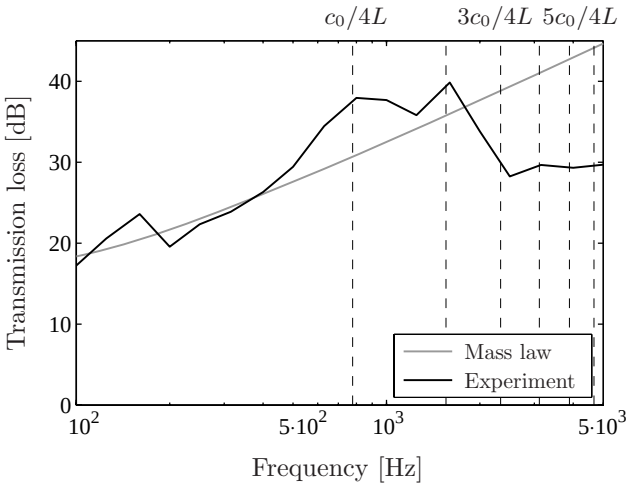


**Figure 5.9**: Measured sound transmission loss of panel with tubes compared with the mass law.

The measured sound transmission loss of the sandwich reference panel is shown in Figure 5.10. The first eigenfrequency of the mounted sandwich reference panel is 395 Hz. Below this frequency the mass law does not apply. This is also seen in the measurements. However, from the 400 Hz 1/3OB, the differences between the measured transmission loss and the mass law are less than 3.0 dB. In the frequency range for which the resonators of the sandwich panel were tuned, the differences are even smaller. Therefore, it can be concluded that from the 400 Hz 1/3OB, the transmission loss of the sandwich panel can be compared with the mass law.

The measured sound transmission loss of the sandwich panel is shown in Figure 5.11. The first eigenfrequency of the mounted sandwich panel is 375 Hz. Below this frequency, the mass law does not apply. In the entire frequency range above, the sound transmission loss of the sandwich panel is larger than the mass law, and thus also larger than the sound transmission loss of the sandwich reference panel. This means that perforating one of the skin panels of a honeycomb sandwich panel is beneficial for the reduction of sound transmission. From the 400 Hz 1/3 OB, maximum increases are obtained of

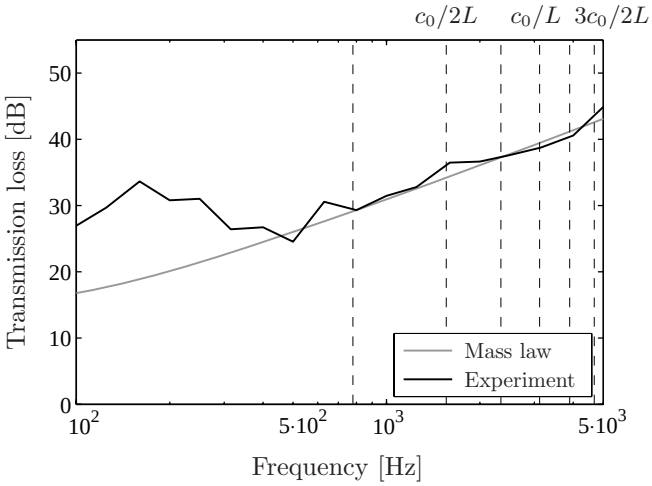


**Figure 5.10**: Measured sound transmission loss of sandwich reference panel compared with the mass law.

6.2 dB in the 630 Hz 1/3OB, 7.2 dB in the 1250 Hz 1/3OB, and 9.2 dB in the 4000 Hz 1/3OB, compared with the mass law.

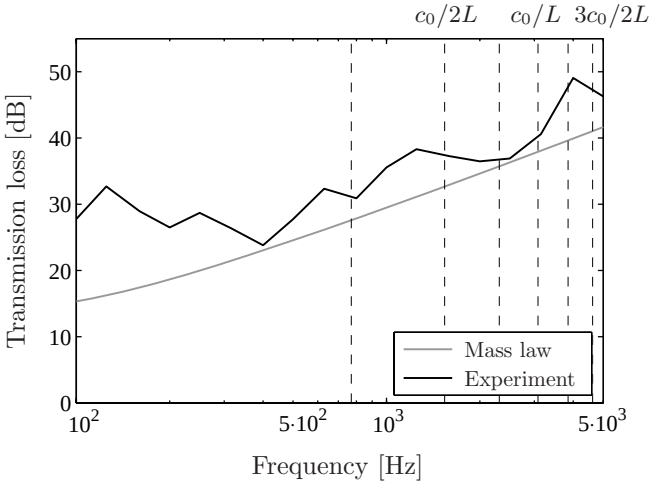


**Figure 5.11**: Measured sound transmission loss of sandwich panel compared with the mass law.

### Orientation of the panel

To investigate the influence of the orientation of the panel, the sandwich panel was tested both mounted with the resonator openings at the receiving side and

mounted with the resonator openings at the incident side. A comparison of the results is shown in Figure 5.12. From the 400 Hz 1/3OB, the differences are less than 2.5 dB. Since these discrepancies are also partially related to the repeatability of the measurements, it can be concluded that the orientation of the panel does not have a very large influence on the measured sound transmission loss.

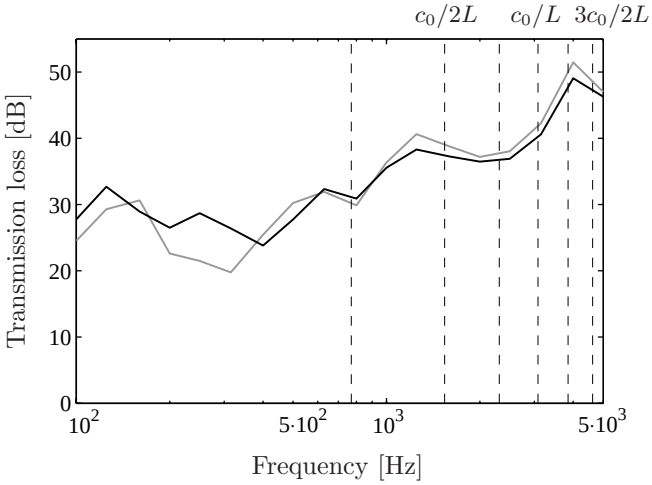


**Figure 5.12**: Measured sound transmission loss of sandwich panel with resonator openings at the incident side (grey) and with resonator openings at the receiving side (black).

### 5.3.2 Comparison with models

In this section, the measured sound transmission loss of the two panels with resonators is compared with the results of the models presented in the previous chapters. Comparisons are made with the one-dimensional analytical models as described in Section 2.3.2, the reduced FEM model presented in Section 4.3, and the full FEM models of one characteristic area as described in Section 4.4.2. First, the models of the test panels are presented. Then, a comparison is made between the calculated and the measured results. Finally, the validity of the models is discussed.

#### One-dimensional analytical model

The one-dimensional analytical models of the two panels were composed as described in Section 2.3.2. The dimensions and mass of the resonator configurations are shown in Table 5.1.

The resonators of the panel with tubes are relatively wide, which means that the shear wave numbers of the air inside and around the resonators are large, so viscothermal effects are negligible. The resonators of the sandwich panel, however, consist of several narrower honeycomb cells (see Figure 5.1). Consequently, the shear wave numbers of the air inside the honeycomb structure are much smaller and viscothermal effects play a more important role. To calculate the propagation coefficient $\Gamma$ and the polytropic coefficient $n$, an equivalent resonator radius $R_{\text{eq}}$ was chosen such that the shear wave number of the resonator equals the shear wave number of one honeycomb cell. According to equation (2.27) this implies that $R_{\text{eq}} = R_h$, where $R_h$ is the inradius of a hexagonal honeycomb cell[3]. With the porosity as given in Table 5.1, an equivalent width $b_{\text{eq}}$ of the characteristic area was calculated by $b_{\text{eq}} = R_{\text{eq}}\sqrt{\pi/\Omega}$. It should be noted that these two equivalent dimensions were only used to calculate the propagation coefficient and the polytropic coefficient.

In Section 2.5 it was mentioned that, due to inlet effects, the effective length of the resonator $L = L_{\text{phy}} + \delta$ is larger than the physical length of the resonator. For a perforated plate with a rectangular pattern, the end correction $\delta$ is given by [37]:

$$\delta = 0.79R\left[1 - 1.47\sqrt{\frac{\pi R^2}{b^2}} + 0.47\left(\frac{\pi R^2}{b^2}\right)^{3/2}\right] \tag{5.17}$$

For the panel with tubes, this end correction was used at both sides of the panel ($\delta = 1.2 \cdot 10^{-3}$ m). In the literature, no expression was found for the side of the panel where the tubes are closed. For the sandwich panel, the end correction was only used for air inside the resonators ($\delta = 1.3 \cdot 10^{-3}$ m).

### Reduced finite element model

The reduced FEM model of the panel with tubes was composed as described in Section 4.3.3[4]. The parameters that were used are listed in Tables 5.1 and 5.2. The pressure excitation was the same as in Section 4.3.3 and the room at the receiving side had a depth of $L_x = 0.244$ m (see also Figure 4.16).

[3]The area of a hexagon is $S = 2\sqrt{3}R_h^2$ and the perimeter of a hexagon is $P = 4\sqrt{3}R_h$.

[4]Only a reduced FEM model of the panel with tubes is considered. For the sandwich panel, the interface elements as presented in Section 4.3.2 have to be adjusted to include also the effect of the air around the resonators. This is not included in the present work.

| Dimensions | | |
|---|---|---|
| $t_p$ | 0.002 | m |
| $t_w$ | 0.00028 | m |
| $t_e$ | 0.0006 | m |
| $L_y$ | 0.976 | m |
| $L_z$ | 0.976 | m |

| Material | | |
|---|---|---|
| $\rho$ | 2563 | $kg/m^3$ |
| $E$ | $70{\cdot}10^9$ | $N/m^2$ |
| $\nu$ | 0.3 | - |

**Table 5.2**: Dimensions and material properties of panel with tubes.

### Full finite element model

The full FEM models of one characteristic area of the two panels with resonators were composed as described in Section 4.4. The dimensions and material properties that were used, are listed in Tables 5.1, 5.2 and 5.3. The dimensions of the impedance tube are the same as in Section 4.4.2.

To model the entire honeycomb structure, the air inside the honeycomb cells, and the interaction between the air and the structure is computationally expensive. For the characteristic area of the sandwich panel, therefore, a simplified model was used as shown in Figure 5.13. The mass of the honeycomb structure was included in the mass of the resonator walls by tuning the density $\rho_w$ such that the mass per unit area of the structural model and that of the panel which was tested are the same. In a honeycomb sandwich panel, the honeycomb structure supports the two skin panels over the full surface. This makes the structure rather stiff. In the setup depicted in Figure 5.13, the two plates are only supported at the location of the resonator tube, so the corners of the plate are more flexible. To model the additional stiffness due to the support of the honeycomb structure, the Young's modulus $E_p$ of the plates was chosen somewhat higher than the regular Young's modulus of aluminium. The same holds for the Young's modulus $E_w$ of the resonator walls. Because the radius of the resonator is much larger than the inradius of the honeycomb cells, the walls are more flexible, so the Young's modulus was chosen higher to increase the stiffness. It should be noted that the parameters in this model are not optimised to represent the test panels as well as possible. The main aim is to show the influence of the flexibility of the structure.

To enable a better comparison between models and measurements, the results of all models presented in this section were corrected with the same frequency dependent factor $\sigma_d$ as the mass law given by equation (5.15).

| Dimensions | | |
|---|---|---|
| $t_p$ | $5.6{\cdot}10^{-4}$ | m |
| $t_w$ | $2.54{\cdot}10^{-5}$ | m |

| Material | | |
|---|---|---|
| $\rho_p$ | 2710 | kg/m$^3$ |
| $\rho_w$ | 20800 | kg/m$^3$ |
| $E_p$ | $600{\cdot}10^9$ | N/m$^2$ |
| $E_w$ | $600{\cdot}10^9$ | N/m$^2$ |
| $\nu$ | 0.3 | - |

**Table 5.3**: Dimensions and material properties of sandwich panel.

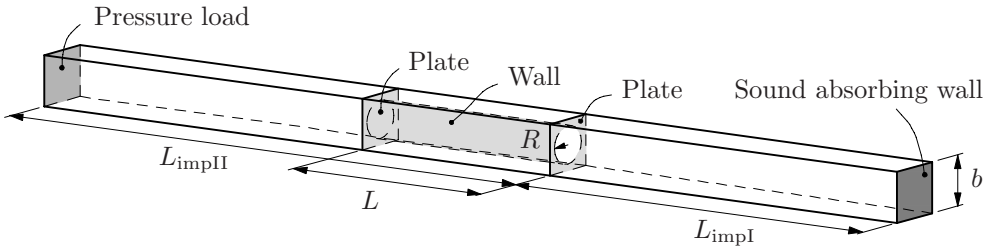


**Figure 5.13**: Setup for sound transmission through a characteristic area of a sandwich panel.

### Experiments versus models

Figures 5.14 and 5.15 show the calculated and measured sound transmission loss of the two panels with resonators in the frequency ranges of 500-3000 Hz and 500-5000 Hz, respectively. To show more detail, the results are presented in narrow bands.

For both panels, the measured sound transmission loss is much smaller than predicted by the one-dimensional analytical model. For the panel with tubes, the centre frequency of the range in which the transmitted sound is reduced is predicted fairly well (see Figure 5.14). However, the extra increase in transmission loss in the frequency range of 500-1200 Hz was not predicted analytically. This increase is even higher than measured in the frequency range for which the resonators were tuned. Also, the decrease in transmission loss for frequencies above 2000 Hz was not predicted analytically. The results obtained with the full FEM model of one characteristic area show that the flexibility of the structure is very important to get a better prediction of the magnitude of the sound transmission loss.

For the sandwich panel, the trends of the measured and analytically calculated transmission loss curves are fairly similar (see Figure 5.15). Around 1541 Hz, where half of the acoustic wavelength equals the thickness of the panel, both transmission loss curves show a small dip caused by internal res-

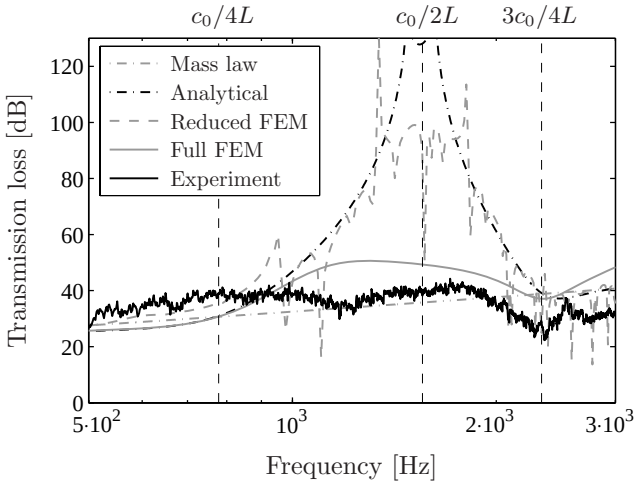


**Figure 5.14**: Calculated and measured transmission loss of panel with tubes.

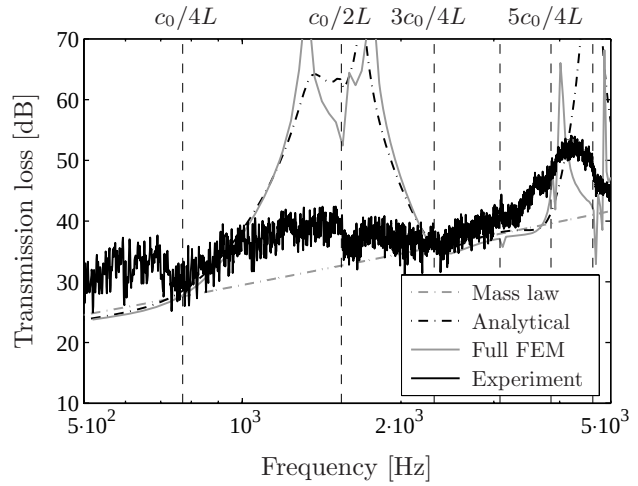


**Figure 5.15**: Calculated and measured transmission loss of sandwich panel.

onances in the cavities of the honeycomb structure. In addition, the higher harmonic in the frequency range of 3000-5000 Hz is observed in both results. However, the frequency belonging to the peak of the measured transmission loss curve is a little lower than predicted analytically. For the sandwich panel too, an extra increase in transmission loss is observed in the lower frequency range, which is not predicted analytically. In the one-dimensional analytical model, the viscothermal effects have a large influence on the height of the peaks in the transmission loss curve (see Figure 5.16). In the full FEM model,

these effects are not included. This leads to an overestimation of the transmission loss, particularly at the frequencies where maximum sound reduction is obtained. This, however, cannot completely explain the large discrepancies between models and measurement. Other possible reasons are discussed below.

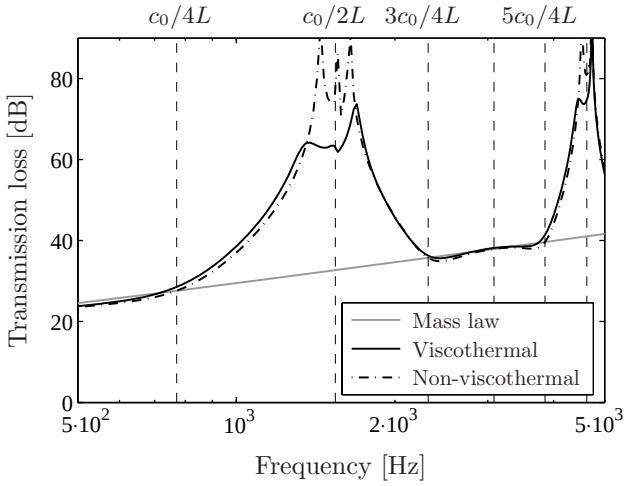


**Figure 5.16**: Sound transmission loss of sandwich panel, calculated with the one-dimensional analytical model, with and without viscothermal effects.

### 5.3.3 Discussion

For both panels, the agreement between measurements and models is bad. This is mainly caused by the fact that there are different factors which play an important role in the transmission of sound through panels with resonators, but none of the models includes *all* these factors. The influences of these phenomena on the different configurations are briefly discussed below.

- *Flexibility of the structure.* The fully coupled FEM model of one characteristic area showed that the flexibility of the structure and the interaction with the surrounding air are very important. Because the structure of the sandwich panel is much stiffer than the panel with tubes, the one-dimensional analytical model predicts the trends better for the sandwich panel.

  In Section 4.4.2, it was seen that for a porosity of about $\Omega = 0.5$, the sound transmission loss decreases with increasing flexibility. For a high transmission loss, a stiff structure is thus desired. Especially the stiffness

of the resonators is important. However, stiffer panels (of similar weight) tend to have a lower critical frequency (see below), which can again be disadvantageous for the sound transmission loss.

The honeycomb structure of the sandwich panel is not modelled in detail. Local effects caused by deformations of the honeycomb cells and the interaction with the air inside the cells are not included, but can possibly influence the sound transmission loss. Because the walls of the honeycomb cells are very thin, transmission of sound in transverse direction could also be possible. This effect is also not included in the models.

- *Viscothermal effects.* The resonators of the panel with tubes are relatively wide, so viscothermal effects hardly play a role. However, in the structure of the sandwich panel, the honeycomb cells are much narrower. Viscothermal effects that are present here, considerably reduce the height of the peaks in the transmission loss curve because of the damping that is added. In the FEM models these effects were not included, so the transmission loss of the sandwich panel is overestimated at some frequencies.

- *Incident sound field.* During the measurements, the panel was excited by a diffuse sound field, i.e. sound incident from all directions. In the one-dimensional analytical model and the FEM models presented in Chapter 4, only normal incident sound was considered. One of the effects that may be caused by obliquely incident sound is coincidence (see below).

- *Panel boundaries.* In Section 4.2.2, it was seen that for a rigid panel, placed in an infinite baffle, the boundaries of the panel hardly influence the radiated sound power if the acoustic wavelength is smaller than the panel dimensions. However, in the experimental setup the panel is not baffled, so different boundary effects could play a role. To investigate this, a more detailed model of the experimental setup is required.

Two other phenomena which can possibly affect the transmission of sound through a panel with resonators are: acoustic coupling between the resonators and coincidence. These influences were neither included in the models used in this section nor thoroughly studied in the present work. However, a brief discussion follows below.

- *Acoustic coupling between the resonators.* In the models presented in this thesis, the acoustic response of the resonators was mostly considered

separately. However, when multiple resonators are placed close to each other, acoustic interaction may exist between adjacent resonators and influence the radiation or transmission of sound. Further research is required to investigate this effect.

- *Coincidence.* The coincidence effect is a combination of the effects of the flexibility of the structure and the incident sound field. Coincidence occurs if the bending wavelength in the panel is equal to the projected wavelength of the incident sound wave, the so-called trace wavelength $\lambda_{\mathrm{tr}}$ (see Figure 5.17). In this case, there is a very good coupling of energy from the incident wave to the bending wave, which makes the panel radiate sound efficiently to the other side [34]. The panel acts as if it is transparent to incident sound waves and the sound waves are freely transmitted [5]. This causes a dip in the transmission loss curve. The depth of the coincidence dip depends on the damping of the panel.

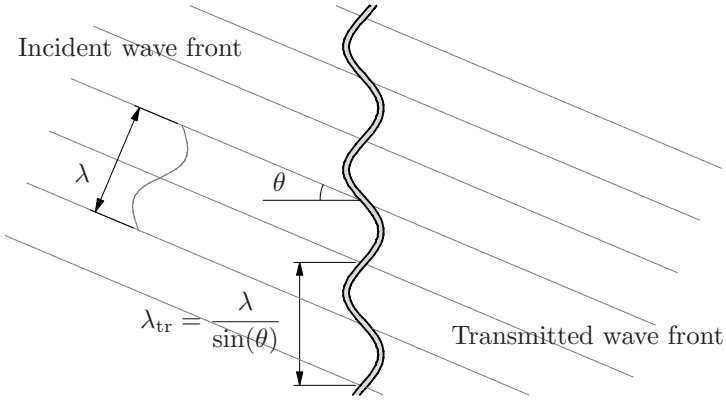


**Figure 5.17**: Coincidence effect for a panel without resonators.

The trace wave number of a sound wave incident at an angle $\theta$ is $k_{\mathrm{tr}} = k\sin(\theta)$. In a thin isotropic plate, the free bending wave number is $k_b = \sqrt[4]{\omega^2 \bar{m}/D}$. For coincidence to occur, both wave numbers have to be equal, which leads to the following expression for the coincidence frequency:

$$f_{\mathrm{co}} = \frac{1}{2\pi}\left[\frac{c_0}{\sin(\theta)}\right]^2 \sqrt{\frac{\bar{m}}{D}} \tag{5.18}$$

where $D$ is the bending stiffness of the panel. Hence, for a given angle of incidence, there is a unique coincidence frequency and vice versa [20]. The coincidence frequency decreases with the angle of incidence. The

fact that $\sin(\theta)$ cannot exceed unity imposes a lower frequency limit on the coincidence phenomenon, the so-called critical frequency:

$$f_c = \frac{c_0^2}{2\pi}\sqrt{\frac{\bar{m}}{D}} \tag{5.19}$$

Equation (5.18) also implies that coincidence cannot occur for normal incident sound. This is also the reason why this phenomenon is not observed in the results obtained with the models for normal incidence sound transmission. Nevertheless, the coincidence effect may be a possible explanation for the decrease in transmission loss of the panel with tubes that is measured at frequencies above 2000 Hz.

In thick panels, like honeycomb sandwich panels, transverse shear flexibility also plays a role. Renji derived expressions, including this effect, for the critical and the coincidence frequencies of thick isotropic plates based on the Mindlin plate theory [40]. In the measured transmission loss of the sandwich panel, no effects of coincidence are observed. Because the stiffness of the sandwich panel is very high, the critical frequency is far below the frequency range that is considered here.

## 5.4 Concluding remarks

To validate the models presented in the previous chapters, sound transmission loss measurements were performed on resonator panels of two different configurations: a panel with tubes and a sandwich panel. The transmission of sound through a measuring surface of 1.00 × 1.00 m was measured by means of the sound intensity method.

The measurements demonstrated that by applying tube resonators, sound transmission can be reduced. Compared with the mass law, a maximum increase in transmission loss of 9.2 dB was obtained for the sandwich panel and of 7.1 dB for the panel with tubes. In the entire frequency range above the 400 Hz 1/3 OB, the transmission loss of the sandwich panel was both larger than the mass law and larger than the transmission loss of a sandwich panel without resonators.

However, for both panels with resonators, the increases were not as large as predicted by the models. The panel with tubes even showed decreases in transmission loss in the higher frequency range. The predictions for the sandwich panel were slightly better because of the higher stiffness of the panel.

To achieve a better prediction of the transmission of sound through panels with resonators, more detailed, large-scale models are required. It was shown

that the flexibility of the structure and the interaction with the surrounding air are very important. In particular, the flexibility of the resonators can decrease the transmission loss considerably. For narrow tube resonators, viscothermal effects play a role as well. They mainly decrease the peaks in the transmission loss curve. Possible influences of the incident sound field, the boundaries of the panel and acoustic coupling between adjacent resonators should be further investigated.

# Chapter 6

# Conclusions and recommendations

## 6.1 Conclusions

In the present work, a new patented concept, as shown in Figure 1.5(b), was presented for the reduction of sound radiation and sound transmission [55]. It was shown that the sound radiated by and transmitted through panels can be reduced considerably by the application of tube resonators. In this thesis, different models and experiments were presented to explore the possibilities of these resonators. The conclusions that can be drawn from the analyses are the following:

- Small-scale models of rigid, infinitely large panels predict that by applying tube resonators, large increases in insertion loss and normal incidence sound transmission loss can be obtained over a broad frequency range. Experiments on sound radiation in an impedance tube show a good agreement between the predictions by the models and the measurements.
- Three important parameters that determine the sound insulating properties of panels with tube resonators are: the length of the resonators, the porosity of the panel, and (in the case of sound transmission) the mass of the panel. The centre frequency of the frequency range in which the sound is reduced is the frequency for which a half, or odd multiples of a half, of the acoustic wavelength is equal to the resonator length.
- For further investigation on the phenomena that play a role in the radiation of sound by and the transmission of sound through panels with

tube resonators, different numerical tools were developed. Besides the aforementioned parameters, other aspects that influence the performance of these panels are: the flexibility of the plate and the resonators, viscothermal effects, and (in the case of sound transmission) the incident sound field. Especially the flexibility of the structure has a large effect on the sound transmission loss. In most cases, the sound transmission loss decreases with increasing flexibility.

- Sound transmission loss measurements on two panels of different configurations demonstrate that by the application of tube resonators, sound transmission can be reduced. However, the increases in sound transmission loss are not as large as predicted by the models. None of the models include *all* aspects that are important for the respective configurations. To improve the predictions of sound transmission through panels with resonators, more detailed, large-scale models are required.

- Sound transmission loss measurements show that the positive effect of tube resonators on the sound transmission loss is larger for a sandwich panel than for a single plate. The main reason for this is the higher stiffness of the sandwich panel.

- Sound transmission loss measurements show that by perforating one of the skin panels of a common honeycomb sandwich panel, the sound insulating properties of such a panel can be improved.

## 6.2 Recommendations

The work presented in this thesis forms the basis for a study on the possible application of tube resonators for sound insulation. To advance this work, further research could be carried out on the following topics:

- Two aspects that were not studied in this thesis are the possible influences of acoustic coupling between the resonators and coincidence (see also Chapter 5). Further research on these effects may be desirable. Another aspect that could be investigated is the influence of damping, both structural and acoustic.

- To enhance the prediction of sound transmission through honeycomb sandwich panels, more detailed models (including viscothermal effects) are needed on the interaction between the honeycomb structure and the air inside the honeycomb cells.

- In the present work, different models were presented based on different assumptions and simplifications. However, none of the models contain *all* aspects that play a role in the transmission of sound through the panels that were tested. Based on the insights gained in this thesis, different models, or aspects of different models, can be combined to get more efficient and/or accurate results.

- The performance of the resonators can be tuned for a specified frequency range by varying the dimensions of the resonators. Once an accurate model is obtained, an optimisation algorithm could be developed to find the optimal configuration.

- In the present work, the performance of panels with tube resonators was assessed by a comparison with the sound insulating properties of panels of the same mass without resonators. To make a further assessment, a comparison could also be made with conventional methods of sound insulation. Examples are porous materials such as glass wool or foam, different types of resonators such as Helmholtz resonators, thin air layers, and viscoelastic damping material.

- The application of tube resonators for reducing sound at lower frequencies requires large resonator lengths. Further research could be carried out to reduce the thickness of the panel, for example, by changing the geometry of the resonators or by folding them (see also Chapter 2). This is especially important for environments like aircraft cabins, where space is limited.

- For the application of tube resonators in practice, further research is needed for suitable materials and efficient production methods. The most important properties for the selection of materials are mass and stiffness.

# Nomenclature

### Roman

| | | |
|---|---|---|
| $A, B, C, D$ | Amplitudes of plane sound wave | [Pa] |
| $a$ | Resonator diameter | [m] |
| $b$ | Width of characteristic area | [m] |
| $C_p$ | Specific heat at constant pressure | [J/(kg K)] |
| $C_v$ | Specific heat at constant volume | [J/(kg K)] |
| $c_0$ | Undisturbed speed of sound | [m/s] |
| $c_{\text{eff}}$ | Effective speed of sound | [m/s] |
| $D$ | Bending stiffness | [Nm] |
| $E$ | Young's modulus | [N/m$^2$] |
| $E_e$ | Young's modulus of resonator end | [N/m$^2$] |
| $E_p$ | Young's modulus of plate | [N/m$^2$] |
| $E_w$ | Young's modulus of resonator wall | [N/m$^2$] |
| $\mathbf{f}$ | Force vector | [N] |
| $f$ | Frequency | [Hz] |
| $f_c$ | Critical frequency | [Hz] |
| $f_e$ | Eigenfrequency | [Hz] |
| $f_{\text{co}}$ | Coincidence frequency | [Hz] |
| $G(\mathbf{r}, \mathbf{r}_0)$ | Green's function | [–] |
| $G_{12}$ | One-sided cross spectrum of two pressure signals | [Pa$^2$] |
| $H_{21}$ | Transfer function of two pressure signals | [–] |
| $I_n$ | Modified Bessel function of the first kind of order $n$ | [–] |
| $\bar{I}_i$ | Time-averaged incident sound intensity | [Wm$^{-2}$] |
| $\bar{I}_r$ | Time-averaged sound intensity in direction $r$ | [Wm$^{-2}$] |
| $\bar{I}_{\text{ref}}$ | Time-averaged reference sound intensity | [Wm$^{-2}$] |
| $\mathrm{i} = \sqrt{-1}$ | Imaginary number | [–] |
| $J_n$ | Bessel function of the first kind of order $n$ | [–] |
| $\mathbf{K}$ | Stiffness matrix | [N/m] |

| | | |
|---|---|---|
| $K_n$ | Modified Bessel function of the second kind of order $n$ | [–] |
| $k$ | Wave number | [$\mathrm{m}^{-1}$] |
| $k_{\mathrm{tr}}$ | Trace wave number | [$\mathrm{m}^{-1}$] |
| $L$ | Resonator length | [m] |
| $L_{\mathrm{I}}$ | Distance to pressure transducer I | [m] |
| $L_{\mathrm{II}}$ | Distance to pressure transducer II | [m] |
| $L_{\mathrm{imp}}$ | Length of impedance tube | [m] |
| $L_p$ | Sound pressure level | [dB] |
| $L_I$ | Sound intensity level | [dB] |
| $L_W$ | Sound power level | [dB] |
| $L_y, L_z$ | Width and height of panel | [m] |
| $l$ | Characteristic length scale | [m] |
| $\mathbf{M}$ | Mass matrix | [kg] |
| $m$ | Mass | [kg] |
| $\bar{m}$ | Mass per unit area | [$\mathrm{kg/m}^2$] |
| $n$ | Polytropic coefficient | [–] |
| $P$ | Perimeter | [m] |
| $\mathbf{p}$ | Pressure vector | [Pa] |
| $\mathbf{p}_{\mathrm{surf}}$ | Pressure vector evaluated close to surface | [Pa] |
| $p$ | Pressure | [Pa] |
| $\tilde{p}$ | Pressure amplitude | [Pa] |
| $\check{p}$ | Dimensionless pressure amplitude | [–] |
| $p_0$ | Mean pressure | [Pa] |
| $p_{\mathrm{I}}$ | Pressure measured with pressure transducer I | [Pa] |
| $p_{\mathrm{II}}$ | Pressure measured with pressure transducer II | [Pa] |
| $p_{\mathrm{ref}}$ | Reference pressure | [Pa] |
| $p_{\mathrm{rms}}$ | Root mean squared pressure | [Pa] |
| $q$ | Distributed load | [$\mathrm{N/m}^2$] |
| $q$ | Volume velocity | [$\mathrm{m}^4/\mathrm{s}$] |
| $\mathbf{r}$ | Location vector | [m] |
| $\mathbf{r}_0$ | Location vector of a point on a surface $S$ | [m] |
| $r$ | Coordinate in radial direction | [m] |
| $R$ | Resonator radius | [m] |
| $R_0$ | Gas constant | [$\mathrm{J/(mol\,K)}$] |
| $R_i$ | Inner radius of cylindrical layer | [m] |
| $R_o$ | Outer radius of cylindrical layer | [m] |
| $R_{\mathrm{imp}}$ | Radius of impedance tube | [m] |
| $S$ | Characteristic area | [$\mathrm{m}^2$] |
| $S$ | Panel area | [$\mathrm{m}^2$] |

| | | |
|---|---|---|
| $S_e$ | Area of elemental radiator | [m$^2$] |
| $S_r$ | Cross-sectional area of resonator | [m$^2$] |
| $s$ | Shear wave number | [–] |
| $T$ | Temperature | [K] |
| $\tilde{T}$ | Temperature amplitude | [K] |
| $\check{T}$ | Dimensionless temperature amplitude | [–] |
| $T_0$ | Mean temperature | [K] |
| $t$ | Time | [s] |
| $t_e$ | Thickness of resonator end | [m] |
| $t_p$ | Thickness of plate | [m] |
| $t_w$ | Thickness of resonator wall | [m] |
| $\mathbf{v}$ | Fluid velocity | [m/s] |
| $v$ | Fluid velocity | [m/s] |
| $\tilde{v}$ | Fluid velocity amplitude | [m/s] |
| $\check{v}$ | Dimensionless fluid velocity amplitude | [–] |
| $v_s$ | Normal structural velocity | [m/s] |
| $\bar{W}$ | Time-averaged sound power | [W] |
| $\bar{W}_i$ | Time-averaged incident sound power | [W] |
| $\bar{W}_{\mathrm{ref}}$ | Time-averaged reference sound power | [W] |
| $\bar{W}_t$ | Time-averaged transmitted sound power | [W] |
| $\check{w}$ | Dimensionless fluid velocity amplitude | [–] |
| $x, y, z$ | Coordinates | [m] |
| $\mathbf{Z}$ | Impedance matrix | [Pa s/m] |
| $\mathbf{Z}_{\mathrm{surf}}$ | Impedance matrix evaluated close to surface | [Pa s/m] |
| $Z$ | Impedance | [Pa s/m] |

**Greek**

| | | |
|---|---|---|
| $\alpha$ | Free space angle in Helmholtz integral equation | [–] |
| $\Gamma$ | Propagation coefficient | [–] |
| $\Gamma_{fs}$ | Interface area | [m$^2$] |
| $\gamma$ | Ratio of specific heats | [–] |
| $\delta$ | End correction | [m] |
| $\eta$ | Dimensionless radius | [–] |
| $\eta_i$ | Dimensionless inner radius of cylindrical layer | [–] |
| $\eta_o$ | Dimensionless outer radius of cylindrical layer | [–] |
| $\theta$ | Angle of incident sound | [rad] |
| $\kappa$ | Reduced frequency | [–] |

| | | |
|---|---|---|
| $\lambda$ | Acoustic wavelength | [m] |
| $\lambda_T$ | Thermal conductivity | [J/msK] |
| $\lambda_{\mathrm{tr}}$ | Acoustic trace wavelength | [m] |
| $\mu$ | Dynamic viscosity | [Pa s] |
| $\mu_b$ | Bulk viscosity | [Pa s] |
| $\nu$ | Poisson's ratio | [–] |
| $\xi$ | Dimensionless coordinate | [–] |
| $\rho$ | Density | [kg/m$^3$] |
| $\tilde{\rho}$ | Density amplitude | [kg/m$^3$] |
| $\check{\rho}$ | Dimensionless density amplitude | [–] |
| $\rho_0$ | Mean density | [kg/m$^3$] |
| $\sigma$ | Square root of Prandtl number | [–] |
| $\sigma_d$ | Radiation efficiency | [–] |
| $\tau$ | Transmission coefficient | [–] |
| $\Omega$ | Porosity | [–] |
| $\omega$ | Angular frequency | [rad/s] |

**Abbreviations**

| | |
|---|---|
| CV | Control volume |
| CMS | Component mode synthesis |
| DOF | Degree(s) of freedom |
| FEM | Finite element method |
| FFT | Fast Fourier transform |
| GMRES | Generalised minimal residual |
| IL | Insertion loss |
| TL | Transmission loss |
| 1/3OB | One-third octave band |

**Miscellaneous**

| | |
|---|---|
| $\nabla$ | Gradient operator |
| $\Delta$ | Laplace operator |
| Re( ) | Real part |
| Im( ) | Imaginary part |
| $x^*$ | Complex conjugate of $x$ |
| $\mathbf{x}^T$ | Transpose of $\mathbf{x}$ |

| | |
|---|---|
| $\mathbf{x}^H$ | Hermitian of $\mathbf{x}$ (complex conjugate transposed) |

# Appendix A

# Low reduced frequency solutions

In this appendix, various low reduced frequency solutions for prismatic tubes and layers are considered and derived. In Section A.1, viscothermal wave propagation in a square tube is compared with viscothermal wave propagation in a cylindrical tube. In Sections A.2 and A.3, solutions for the acoustic variables are derived for cylindrical layers with different boundary conditions at the inner and outer boundaries. The solutions presented in the last section are validated by experiments in an impedance tube.

## A.1 Square versus cylindrical tube

In this section, viscothermal wave propagation in a square tube is compared with viscothermal wave propagation in a cylindrical tube (see Figure A.1).

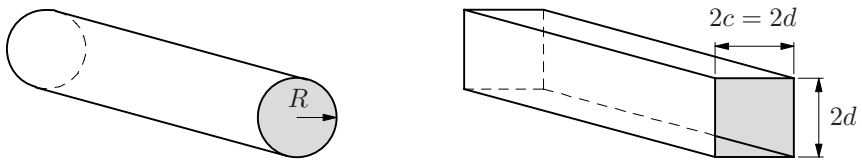


(a) Cylindrical tube. (b) Square tube.

**Figure A.1**: Cylindrical tube and square tube.

For a uniform tube of arbitrary cross-sectional shape, the pressure and the

fluid velocity, averaged over the cross-section, can be written as:

$$p(\xi) = Ae^{\Gamma\xi} + Be^{-\Gamma\xi} \tag{A.1}$$

$$v(\xi) = \frac{G}{\rho_0 c_0}\left(Ae^{\Gamma\xi} - Be^{-\Gamma\xi}\right) \tag{A.2}$$

The propagation coefficient $\Gamma$ and coefficient $G$ both depend on the cross-sectional shape and are defined as [48, 49]:

$$\Gamma = \mathrm{i}\sqrt{\frac{\gamma - (\gamma-1)F\left(\frac{\lambda_T}{\rho_0 C_p}\right)}{F\left(\frac{\mu}{\rho_0}\right)}} \tag{A.3}$$

$$G = \mathrm{i}\Gamma F\left(\frac{\mu}{\rho_0}\right) \tag{A.4}$$

For a cylindrical tube with radius $R$, the function $F(\phi)$ is given by:

$$F(\phi) = -\frac{\mathrm{J}_2(\mathrm{i}^{3/2}R\sqrt{\omega/\phi})}{\mathrm{J}_0(\mathrm{i}^{3/2}R\sqrt{\omega/\phi})} \tag{A.5}$$

For a rectangular tube with sides $2c$ and $2d$, the function $F(\phi)$ is given by:

$$F(\phi) = \frac{4\mathrm{i}\omega}{\phi c^2 d^2}\sum_{i=0}^{\infty}\sum_{j=0}^{\infty}\left[\alpha_i^2\beta_j^2\left(\alpha_i^2 + \beta_j^2 + \frac{\mathrm{i}\omega}{\phi}\right)\right]^{-1} \tag{A.6}$$

with:

$$\alpha_i = \left(i + \frac{1}{2}\right)\frac{\pi}{c} \qquad \beta_j = \left(j + \frac{1}{2}\right)\frac{\pi}{d} \qquad i, j = 0, 1, 2, \ldots \tag{A.7}$$

The definition of the shear wave number is given by equation (2.15). For a tube of arbitrary cross-sectional shape, the characteristic length scale $l$ in this expression can be defined by equation (2.27). If the dimensions of both cross-sections are chosen such that the shear wave numbers are the same, the same amount of viscothermal effects is present. For tubes with a circular and a square cross-section, this happens if $R = d$. In Figures A.2 and A.3 the propagation coefficient $\Gamma$ and the coefficient $G$ of a cylindrical and a square tube are plotted for different values of the characteristic length scale. If the shear wave numbers are the same and within a physically relevant range, the cross-sectional shape of the tubes hardly influences the viscothermal wave propagation. It is also seen that for high frequencies (i.e. large values of the shear wave number) the solutions converge to the standard acoustic solutions, i.e. $\Gamma = \mathrm{i}$ and $G = -1$.

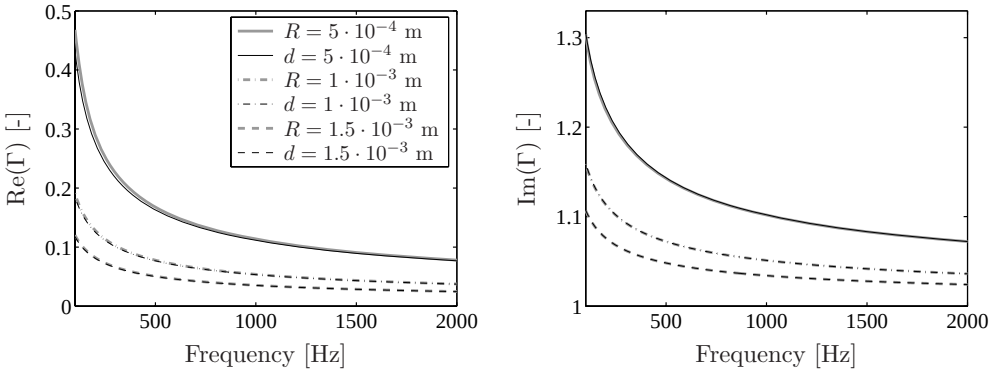


(a) Real part. (b) Imaginary part.

**Figure A.2**: Real and imaginary part of propagation coefficient $\Gamma$ for a cylindrical tube with radius $R$ and a square tube with sides $2d$ for different cross-sectional dimensions.

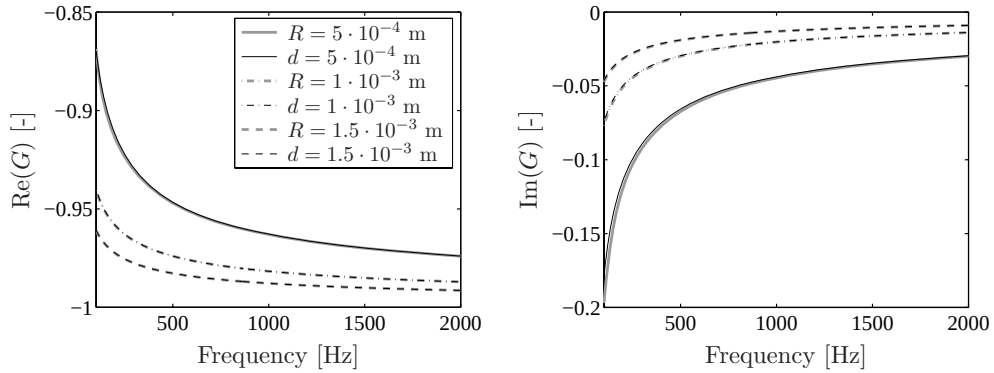


(a) Real part. (b) Imaginary part.

**Figure A.3**: Real and imaginary part of coefficient $G$ for a cylindrical tube with radius $R$ and a square tube with sides $2d$ for different cross-sectional dimensions.

## A.2 Cylindrical layer with axially vibrating inner wall and symmetry conditions at outer boundaries

In this section, the low reduced frequency solution is derived for a cylindrical layer with an acoustically hard, axially vibrating inner wall and symmetry conditions at the outer boundaries. A schematic representation of this configuration is shown in Figure A.4.

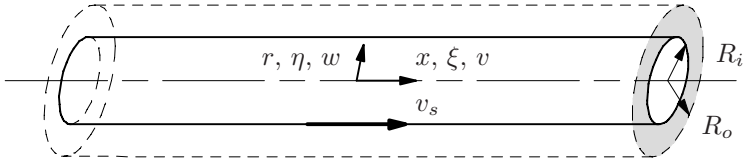


**Figure A.4**: Cylindrical layer with axially vibrating inner wall and symmetry conditions at the outer boundaries.

The corresponding boundary conditions are described by equations (2.30) and (2.31):

$$\check{v} = \check{v}_s\,, \qquad \check{w} = 0\,, \qquad \check{T} = 0 \qquad \text{at} \quad \eta = \eta_i \tag{A.8}$$

$$\frac{\partial \check{v}}{\partial \eta} = 0\,, \qquad \check{w} = 0\,, \qquad \frac{\partial \check{T}}{\partial \eta} = 0 \qquad \text{at} \quad \eta = \eta_o \tag{A.9}$$

With these boundary conditions, equations (2.10) to (2.14) are solved in a similar way as presented by Tijdeman [50]. The latter equations are given by:

$$\mathrm{i}\check{v} = -\frac{1}{\gamma}\frac{\partial \check{p}}{\partial \xi} + \frac{1}{s^2}\left[\frac{\partial^2 \check{v}}{\partial \eta^2} + \frac{1}{\eta}\frac{\partial \check{v}}{\partial \eta}\right] \tag{A.10}$$

$$0 = -\frac{1}{\gamma}\frac{\partial \check{p}}{\partial \eta} \tag{A.11}$$

$$\mathrm{i}\kappa\check{\rho} = -\left[\kappa\frac{\partial \check{v}}{\partial \xi} + \frac{\partial \check{v}}{\partial \eta} + \frac{\check{v}}{\eta}\right] \tag{A.12}$$

$$\check{p} = \check{\rho} + \check{T} \tag{A.13}$$

$$\mathrm{i}\check{T} = \mathrm{i}\frac{\gamma - 1}{\gamma}\check{p} + \frac{1}{\sigma^2 s^2}\left[\frac{\partial^2 \check{T}}{\partial \eta^2} + \frac{1}{\eta}\frac{\partial \check{T}}{\partial \eta}\right] \tag{A.14}$$

**Low reduced frequency solution**

Upon putting $\check{v} = f(\xi)h(z)$ with $z = \sqrt{\mathrm{i}}s\eta$, equation (A.10) can be rewritten as:

$$\frac{\partial^2 h}{\partial z^2} + \frac{1}{z}\frac{\partial h}{\partial z} + h = \frac{\mathrm{i}}{\gamma f(\eta)}\frac{\mathrm{d}\check{p}}{\mathrm{d}\xi} \tag{A.15}$$

with the solution:

$$h(z) = C_1\mathrm{I}_0(-\mathrm{i}z) + C_2\mathrm{K}_0(-\mathrm{i}z) + \frac{\mathrm{i}}{\gamma f(\eta)}\frac{\mathrm{d}\check{p}}{\mathrm{d}\xi} \tag{A.16}$$

The expressions for the integration constants $C_1$ and $C_2$ are found by applying the boundary conditions for $\check{v}$ as described by equations (A.8) and (A.9). This

yields:

$$\check{v}(\xi,\eta) = \frac{\mathrm{i}}{\gamma}\frac{\mathrm{d}\check{p}}{\mathrm{d}\xi}D(s,\eta) + \check{v}_s\left[D_1(s)\mathrm{I}_0(\sqrt{\mathrm{i}}s\eta) + D_2(s)\mathrm{K}_0(\sqrt{\mathrm{i}}s\eta)\right] \tag{A.17}$$

with:

$$D(\phi,\eta) = 1 - D_1(\phi)\mathrm{I}_0(\sqrt{\mathrm{i}}\phi\eta) - D_2(\phi)\mathrm{K}_0(\sqrt{\mathrm{i}}\phi\eta) \tag{A.18}$$

and:

$$D_1(\phi) = \frac{\mathrm{K}_1(\sqrt{\mathrm{i}}\phi\eta_o)}{\mathrm{I}_0(\sqrt{\mathrm{i}}\phi\eta_i)\mathrm{K}_1(\sqrt{\mathrm{i}}\phi\eta_o) + \mathrm{K}_0(\sqrt{\mathrm{i}}\phi\eta_i)\mathrm{I}_1(\sqrt{\mathrm{i}}\phi\eta_o)} \tag{A.19a}$$

$$D_2(\phi) = \frac{\mathrm{I}_1(\sqrt{\mathrm{i}}\phi\eta_o)}{\mathrm{I}_0(\sqrt{\mathrm{i}}\phi\eta_i)\mathrm{K}_1(\sqrt{\mathrm{i}}\phi\eta_o) + \mathrm{K}_0(\sqrt{\mathrm{i}}\phi\eta_i)\mathrm{I}_1(\sqrt{\mathrm{i}}\phi\eta_o)} \tag{A.19b}$$

Equation (A.14) can be solved in a similar way. Application of the boundary conditions for $\check{T}$ yields:

$$\check{T}(\xi,\eta) = \frac{\gamma-1}{\gamma}\check{p}\,D(s\sigma,\eta) \tag{A.20}$$

Substitution of this expression into the equation of state (A.13) gives:

$$\check{\rho}(\xi,\eta) = \check{p}\left[1 - \frac{\gamma-1}{\gamma}D(s\sigma,\eta)\right] \tag{A.21}$$

Subsequently, the pressure and the fluid velocity in radial direction are solved by substitution of equations (A.17) and (A.21) into the equation of continuity (A.12) and integration with respect to $\eta$. With the boundary condition for $\check{w}$ described by equation (A.9), this leads to:

$$\check{w}(\xi,\eta) = \frac{\mathrm{i}k}{\eta}\frac{\eta_o^2-\eta^2}{2}\left\{\check{p}\left[1 + \frac{\gamma-1}{\gamma}M(s\sigma)\right] - \frac{\mathrm{d}^2\check{p}}{\mathrm{d}\xi^2}\frac{1}{\gamma}M(s)\right\} \tag{A.22}$$

with:

$$M(\phi) = -1 + \frac{2}{\eta_o^2-\eta^2}\frac{1}{\sqrt{\mathrm{i}}\phi}\left\{D_1(\phi)\left[\eta_o\mathrm{I}_1(\sqrt{\mathrm{i}}\phi\eta_o) - \eta_i\mathrm{I}_1(\sqrt{\mathrm{i}}\phi\eta)\right] + \right.$$
$$\left. - D_2(\phi)\left[\eta_o\mathrm{K}_1(\sqrt{\mathrm{i}}\phi\eta_o) - \eta\mathrm{K}_1(\sqrt{\mathrm{i}}\phi\eta)\right]\right\} \tag{A.23}$$

With boundary condition for $\check{w}$ described by equation (A.8), the solution for the pressure becomes:

$$\check{p}(\xi) = \check{A}e^{\Gamma\xi} + \check{B}e^{-\Gamma\xi} \tag{A.24}$$

with the propagation coefficient defined as:

$$\Gamma = \sqrt{\frac{1}{N(s)}\frac{\gamma}{n}} \tag{A.25}$$

with:

$$N(\phi) = -1 + \frac{2}{\eta_o^2 - \eta_i^2}\frac{1}{\sqrt{\mathrm{i}}\phi}\left\{D_1(\phi)\left[\eta_o \mathrm{I}_1(\sqrt{\mathrm{i}}\phi\eta_o) - \eta_i \mathrm{I}_1(\sqrt{\mathrm{i}}\phi\eta_i)\right] + \right.$$
$$\left. - D_2(\phi)\left[\eta_o \mathrm{K}_1(\sqrt{\mathrm{i}}\phi\eta_o) - \eta_i \mathrm{K}_1(\sqrt{\mathrm{i}}\phi\eta_i)\right]\right\} \tag{A.26}$$

and the polytropic coefficient given by:

$$n = \left[1 + \frac{\gamma - 1}{\gamma}N(s\sigma)\right]^{-1} \tag{A.27}$$

By using $p_0 = \rho_0 c_0^2/\gamma$, the solutions for the acoustic variables can be written in dimensional form as:

$$p(\xi) = Ae^{\Gamma\xi} + Be^{-\Gamma\xi} \tag{A.28}$$

$$v(\xi,\eta) = \frac{\mathrm{i}\Gamma}{\rho_0 c_0}D(s,\eta)\left[Ae^{\Gamma\xi} - Be^{-\Gamma\xi}\right] +$$
$$+ v_s\left[D_1(s)\mathrm{I}_0(\sqrt{\mathrm{i}}s\eta) + D_2(s)\mathrm{K}_0(\sqrt{\mathrm{i}}s\eta)\right] \tag{A.29}$$

$$w(\xi,\eta) = \frac{\gamma}{\rho_0 c_0}\frac{\mathrm{i}k}{\eta}\frac{\eta_o^2 - \eta^2}{2}\left[1 + \frac{\gamma-1}{\gamma}M(s\sigma) - \frac{\Gamma^2}{\gamma}M(s)\right]\left[Ae^{\Gamma\xi} + Be^{-\Gamma\xi}\right] \tag{A.30}$$

$$\rho(\xi,\eta) = \frac{\gamma}{c_0^2}\left[1 - \frac{\gamma-1}{\gamma}D(s\sigma,\eta)\right]\left[Ae^{\Gamma\xi} + Be^{-\Gamma\xi}\right] \tag{A.31}$$

$$T(\xi,\eta) = T_0\frac{\gamma-1}{\rho_0 c_0^2}D(s\sigma,\eta)\left[Ae^{\Gamma\xi} + Be^{-\Gamma\xi}\right] \tag{A.32}$$

**Polytropic coefficient**

The coefficient $n$ can be interpreted as a polytropic coefficient, which relates the pressure to the density according to:

$$\frac{\tilde{p}_{\mathrm{int}}}{(\tilde{\rho}_{\mathrm{int}})^n} = C \tag{A.33}$$

where $C$ is a constant and $\tilde{p}_{\text{int}}$ and $\tilde{\rho}_{\text{int}}$ are integrated over the cross-section. The polytropic coefficient $n$ is a function of the product $s\sigma$. Since this product does not depend on the viscosity $\mu$, only thermal effects are involved. By means of a Taylor expansion, the pressure and the density can be linearised as follows:

$$\tilde{p}_{\text{int}} = p_0 \left(1 + \check{p}_{\text{int}} e^{\mathrm{i}\omega t}\right) \quad \rightarrow \quad \tilde{p}_{\text{int}} = p_0(1 + \check{p}_{\text{int}}) \tag{A.34}$$

$$\tilde{\rho}_{\text{int}} = \rho_0 \left(1 + \check{\rho}_{\text{int}} e^{\mathrm{i}\omega t}\right) \quad \rightarrow \quad (\tilde{\rho}_{\text{int}})^n = \rho_0^n(1 + n\check{\rho}_{\text{int}}) \tag{A.35}$$

Substitution of these linearised quantities into the polytropic relation (A.33) yields:

$$\frac{p_0(1 + \check{p}_{\text{int}})}{\rho_0^n(1 + n\check{\rho}_{\text{int}})} = C \tag{A.36}$$

By taking the constant $C = p_0/\rho_0^n$, the polytropic coefficient can be written as:

$$n = \frac{\check{p}_{\text{int}}}{\check{\rho}_{\text{int}}} \tag{A.37}$$

Integrating equation (A.21) and substituting this into equation (A.37) gives the expression for $n$ as described by equation (A.27). In Figure A.5 the polytropic coefficient is shown for different values of $R_i/R_o$. For small values of $s\sigma$ the polytropic coefficient approaches one, i.e. isothermal conditions. For large values of $s\sigma$ the polytropic coefficient approaches $\gamma$, i.e. adiabatic conditions.

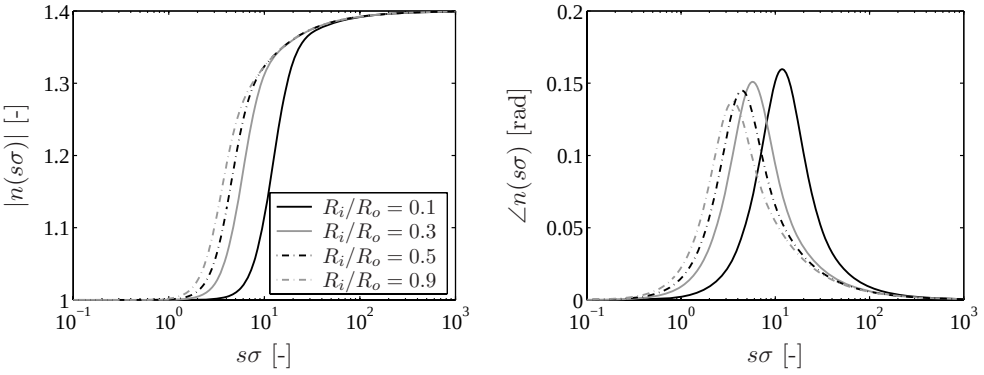


(a) Magnitude. (b) Phase.

**Figure A.5**: Magnitude and phase of the polytropic coefficient.

## A.3 Cylindrical layer with axially vibrating walls

In this section, the low reduced frequency solution is derived for a cylindrical layer with acoustically hard, axially vibrating walls. A schematic representation of this configuration is shown in Figure A.6. The dimensionless velocity of the harmonically vibrating walls is $\check{v}_s = v_s/c_0$. The characteristic length scale is equal to $l = R_o - R_i$.

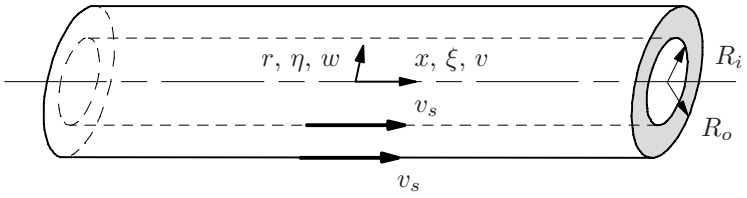


**Figure A.6**: Cylindrical layer with axially vibrating walls.

### Low reduced frequency solution

With $\eta_o = R_o/l$ and $\eta_i = R_i/l$ defined as the dimensionless inner and outer radius, respectively, the boundary conditions can be formulated as follows:

$$\check{v} = \check{v}_s\,, \qquad \check{w} = 0\,, \qquad \check{T} = 0 \qquad \text{at} \quad \eta = \eta_i \tag{A.38}$$

$$\check{v} = \check{v}_s\,, \qquad \check{w} = 0\,, \qquad \check{T} = 0 \qquad \text{at} \quad \eta = \eta_o \tag{A.39}$$

The only difference with the cylindrical layer considered in Section A.2 is that now also the outer wall is acoustically hard and axially vibrating. By applying the boundary conditions to equations (A.10) to (A.14), the acoustic variables can be solved in a similar way. The resulting solutions are the same as presented in Section A.2. Only $D_1(\phi)$ and $D_2(\phi)$ are defined differently now:

$$D_1(\phi) = \frac{\mathrm{K}_0(\sqrt{\mathrm{i}}\phi\eta_i) - \mathrm{K}_0(\sqrt{\mathrm{i}}\phi\eta_o)}{\mathrm{I}_0(\sqrt{\mathrm{i}}\phi\eta_o)\mathrm{K}_0(\sqrt{\mathrm{i}}\phi\eta_i) - \mathrm{K}_0(\sqrt{\mathrm{i}}\phi\eta_o)\mathrm{I}_0(\sqrt{\mathrm{i}}\phi\eta_i)} \tag{A.40a}$$

$$D_2(\phi) = \frac{-\mathrm{I}_0(\sqrt{\mathrm{i}}\phi\eta_i) + \mathrm{I}_0(\sqrt{\mathrm{i}}\phi\eta_o)}{\mathrm{I}_0(\sqrt{\mathrm{i}}\phi\eta_o)\mathrm{K}_0(\sqrt{\mathrm{i}}\phi\eta_i) - \mathrm{K}_0(\sqrt{\mathrm{i}}\phi\eta_o)\mathrm{I}_0(\sqrt{\mathrm{i}}\phi\eta_i)} \tag{A.40b}$$

### Velocity profile

Figure A.7 shows the influence of the shear wave number on the two terms of equation (A.29) determining the shape of the velocity profile. The magnitude

of the expressions is plotted as a function of the dimensionless radius $\eta$. The influence of the shear wave number on the velocity distribution is similar to that for an axially vibrating cylindrical tube. For large values of the shear wave number, the solutions of the acoustic variables converge to the solutions for standard acoustic wave propagation.

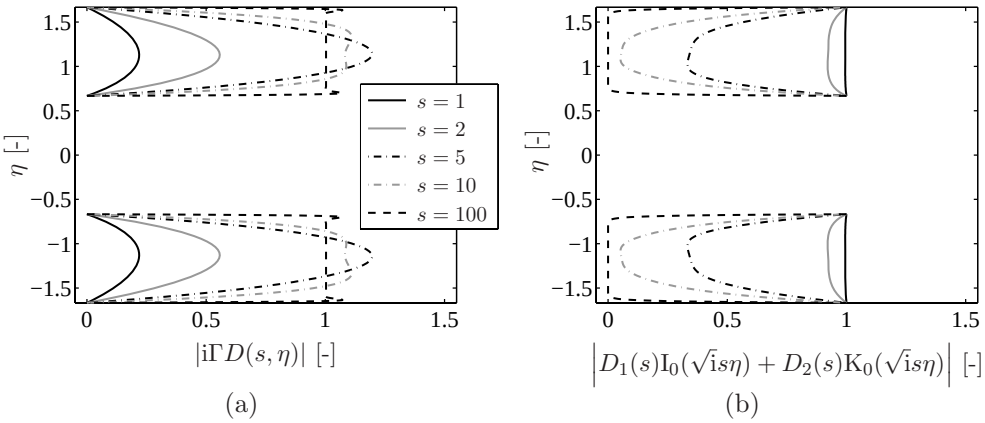


**Figure A.7**: Magnitude of the two terms of equation (A.29) determining the shape of velocity profile, plotted for different values of the shear wave number ($R_i/R_o = 0.4$).

### Experimental validation

The low reduced frequency solution as presented above was validated by means of the experiments in an impedance tube. The procedure used was the same as described in Section 2.5. Figure A.8 shows the two samples that were tested: a thin cylindrical air layer and a thicker cylindrical air layer. On the reverse side of the samples, the layers are closed. The dimensions of the layers, as well as the distances from the fronts of the samples to the end of the impedance tube, are listed in Table A.1.

The model of the experimental setup is also the same as described in Section 2.5. For the pressure and the axial velocity inside the resonator, equations (A.28) and (A.29) with equation (A.40) are used. Since, in the literature, no expression was found for the end correction of a cylindrical layer in a cylindrical tube, the effective resonator length $L$ was determined empirically. The values of the effective resonator lengths that are used in the model are also listed in Table A.1.

Figures A.9 and A.10 show the calculated transfer functions $p_\mathrm{I}/v_s$ for both samples, including and excluding viscothermal effects. In the first case, the low

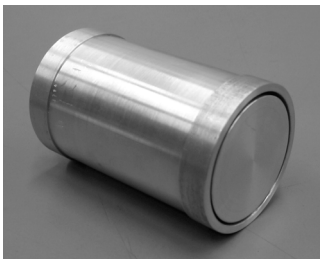

(a) Sample 1 (thin layer).

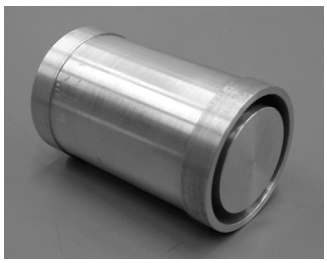

(b) Sample 2 (thick layer).

**Figure A.8**: Photos of the samples for experimental validation.

| | $L_{\text{phy}}$ [m] | $L$ [m] | $R_o$ [m] | $R_i$ [m] | $\Omega$ [-] | $L_{\text{imp}}$ [m] |
|---|---|---|---|---|---|---|
| Sample 1 | 0.0700 | 0.0712 | 0.0220 | 0.0210 | 0.07 | 0.644 |
| Sample 2 | 0.0700 | 0.0720 | 0.0220 | 0.0180 | 0.26 | 0.644 |

**Table A.1**: Dimensions of the samples and experimental setup for validation.

reduced frequency solutions are used; in the latter case, the standard acoustic solutions are used. It can be seen that for both samples the viscothermal effects have a large, damping influence on the amplitudes of the peaks of the transfer functions. Since the differences are clearly visible, it can be concluded that the present experimental setup is suitable for validating the model developed in this section. For the thin cylindrical layer, more viscothermal effects are present than for the thick layer. The largest differences are found around the frequency for which the acoustic wavelength equals a quarter of the length of the cylindrical layer.

In Figures A.11 and A.12 the calculated and measured transfer functions are shown for the two samples. Generally, it can be concluded that there is a good agreement between model and measurement. The amplitudes of the peaks of the transfer functions, which are mainly determined by the amount of viscothermal effects, are well predicted. For sample 1, there is only some discrepancy at the peak around 645 Hz. For sample 2, small discrepancies are observed above 1370 Hz. The latter ones are mainly caused by the fact that the sound pressures are so small here that they approximate the noise floor of the pressure transducers. This makes the measurements less accurate at these frequencies.

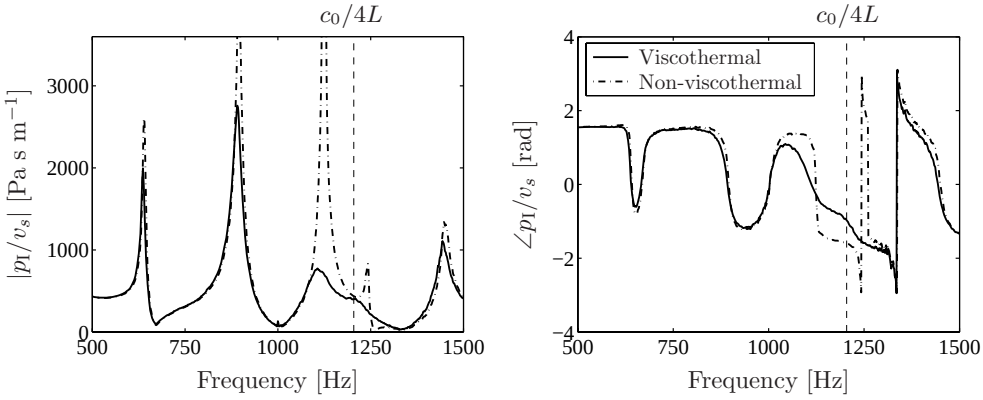


(a) Magnitude. (b) Phase.

**Figure A.9**: Magnitude and phase of calculated transfer functions $p_\mathrm{I}/v_s$ for sample 1, including and excluding viscothermal effects.

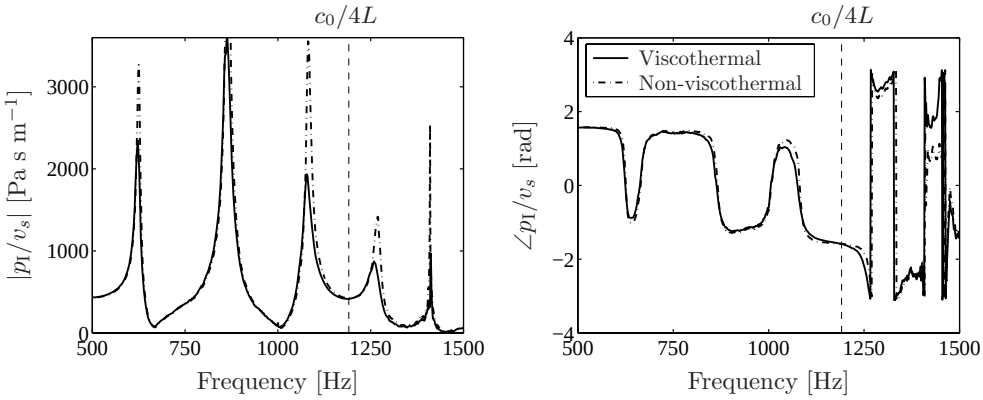


(a) Magnitude. (b) Phase.

**Figure A.10**: Magnitude and phase of calculated transfer functions $p_\mathrm{I}/v_s$ for sample 2, including and excluding viscothermal effects.

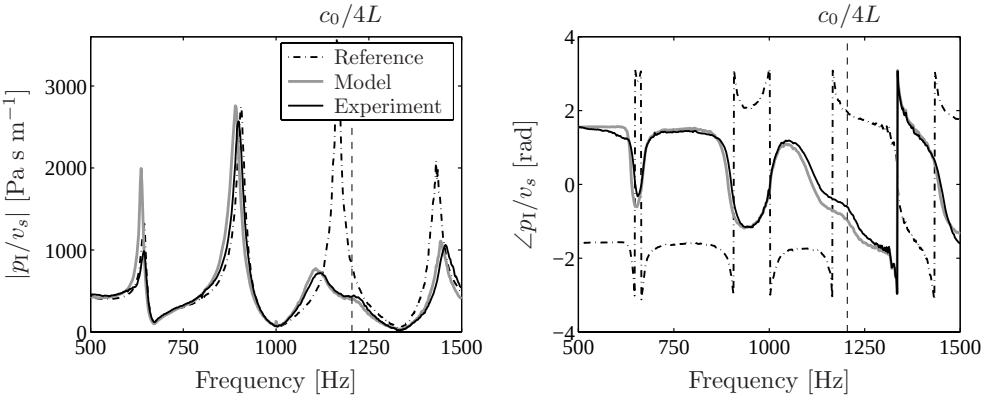


(a) Magnitude. (b) Phase.

**Figure A.11**: Magnitude and phase of calculated and measured transfer functions $p_\mathrm{I}/v_s$ for sample 1.

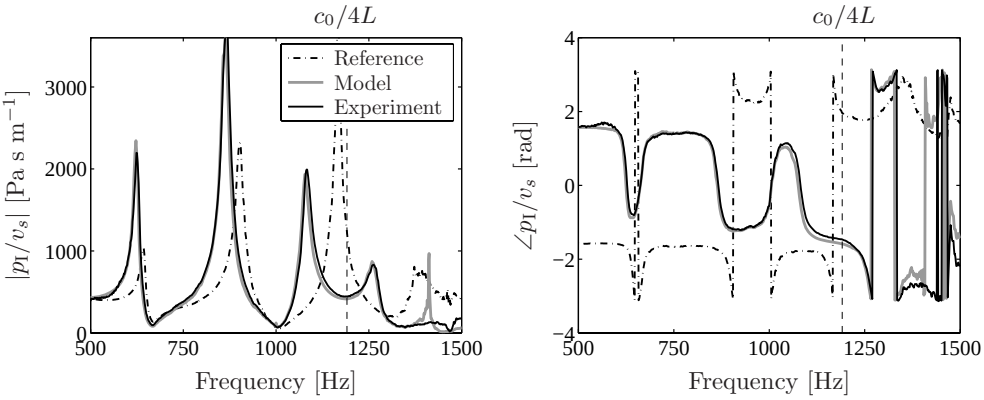


(a) Magnitude. (b) Phase.

**Figure A.12**: Magnitude and phase of calculated and measured transfer functions $p_\mathrm{I}/v_s$ for sample 2.

# Appendix B

# Acoustic reciprocity and symmetry

In this appendix, it is investigated whether the models for sound transmission as presented in Section 2.3.2 satisfy the principles of acoustic reciprocity and symmetry.

## B.1 Acoustic reciprocity

A system is called acoustic reciprocal if the acoustic response remains the same when source and receiver are interchanged. In the present case, this means that, if the conditions at both sides of the panel are the same, the orientation of the panel does not influence the amount of sound which is transmitted through the panel, i.e. it does not matter whether the resonator openings are located at the incident side or at the receiving side. To demonstrate this, the system is represented as an acoustic two-port or four-pole system, as shown in Figure B.1 [17, 39, 45, 58]. At each terminal two variables are defined: the pressures $p$ and the volume velocities $q$. The time-averaged product of these variables represents the acoustic power fed into the system via those terminals.

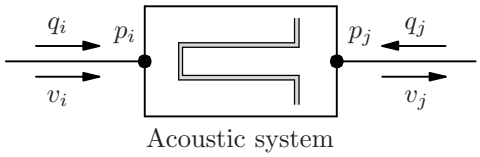


**Figure B.1**: Two-port representation of an acoustic system.

Since a linear passive system is considered, the acoustic two-port can be described by the following equations:

$$p_i = \tilde{Z}_{ii} q_i + \tilde{Z}_{ij} q_j \tag{B.1a}$$

$$p_j = \tilde{Z}_{ji} q_i + \tilde{Z}_{jj} q_j \tag{B.1b}$$

where the $\tilde{Z}$ components are frequency dependent quantities which relate the pressures to the volume velocities. Together they form the so-called impedance matrix, representing the acoustic properties of the system. The components are determined by:

$$\tilde{Z}_{ii} = \left.\frac{p_i}{q_i}\right|_{q_j=0} \qquad \tilde{Z}_{ij} = \left.\frac{p_i}{q_j}\right|_{q_i=0} \tag{B.2a}$$

$$\tilde{Z}_{ji} = \left.\frac{p_j}{q_i}\right|_{q_j=0} \qquad \tilde{Z}_{jj} = \left.\frac{p_j}{q_j}\right|_{q_i=0} \tag{B.2b}$$

where the subscripts $q_i = 0$ and $q_j = 0$ indicate that the respective volume velocities are blocked. According to the principle of reciprocity, the transfer impedance between two terminal pairs should be independent of which terminal pair is taken as the input or output terminal [45]. Therefore, it is required that:

$$\left.\frac{p_i}{q_j}\right|_{q_i=0} = \left.\frac{p_j}{q_i}\right|_{q_j=0} \qquad \text{or} \qquad \tilde{Z}_{ij} = \tilde{Z}_{ji} \tag{B.3}$$

In other words, the system is reciprocal if the impedance matrix is symmetric. For the models presented in Section 2.3.2, the pressures at the two ports are given by (see Figures 2.10 and 2.11):

$$p_i = p_4|_{x_{\mathrm{I}}=0} \qquad p_j = p_2|_{x_{\mathrm{II}}=0} \tag{B.4}$$

and the volume velocities are defined as:

$$q_i = v_4|_{x_{\mathrm{I}}=0}\, S \qquad q_j = -\, v_2|_{x_{\mathrm{II}}=0}\, S \tag{B.5}$$

By substituting equations (B.4) and (B.5) into equations (2.38) to (2.44), the system can be written in terms of the two-port variables $p_i$, $p_j$, $q_i$ and $q_j$. To determine the components of the impedance matrix, $p_i$ and $p_j$ are solved as a function of $q_i$ and $q_j$. If no viscothermal effects are present, the impedance matrix is symmetric and the system is reciprocal. However, if viscothermal effects are present, the system is not reciprocal anymore (see also Beranek and Vér [3]). The same can be proven for the sandwich panel configuration using equations (2.38) to (2.40) and (2.45) to (2.47).

## B.2 Acoustic symmetry

A special case of acoustic reciprocity is acoustic symmetry[1]. If a system is symmetric, it does not matter which terminal is the input terminal and which is the output terminal [17]. For this, it is required that:

$$\tilde{Z}_{ii} = \tilde{Z}_{jj} \qquad \text{and} \qquad \tilde{Z}_{ij} = \tilde{Z}_{ji} \tag{B.6}$$

As was seen in the previous section, the latter condition is only satisfied if no viscothermal effects are present. Using equations (B.2), (B.4), (B.5), and (2.38) to (2.44), it can be shown that the first condition is only satisfied if the panel with tubes has a porosity of $\Omega = 0.5$ and no viscothermal effects are present. For a sandwich panel configuration, acoustic symmetry does not apply under any condition.

[1] At least, this is true in the case of a linear passive two-port system with two variables per terminal.

# Appendix C

# Folded resonators

In Section 2.3.1, a one-dimensional analytical model was presented to calculate the radiation of sound by a panel with tube resonators. It was seen that the frequency range in which the resonators reduce the radiated sound is determined by their length. In order to reduce sound at low frequencies, relatively long resonator lengths are required. For some practical applications, this may be inconvenient because of limited space. One of the possibilities to reduce the length of the resonators is by folding them [35]. In this appendix, one-dimensional analytical models of two types of folded resonators are presented. Schematic representations of these two configurations are shown in Figure 2.19. The resonator type depicted in Figure 2.19(a) is referred to as a tube-in-tube resonator. The configuration depicted in Figure 2.19(b) is referred to as a bent resonator. In the present work, only the effect of these resonators on sound radiation is considered. In Section C.1, the models of both configurations are presented. In Section C.2, one of the models is validated by means of experiments in an impedance tube.

## C.1 One-dimensional analytical models

The models that are presented in this section are based on the same assumptions as described in Section 2.1. The panel is assumed to be rigid and infinitely large, vibrating with a certain uniform harmonic velocity $v_s e^{\mathrm{i}\omega t}$ in normal direction. The dimensions of the characteristic areas are assumed to be small compared to the acoustic wavelength. Each time, one characteristic area is considered.

### Tube-in-tube resonator

Figure C.1 shows the model of a characteristic area of a panel with tube-in-tube resonators. The model consists of three parts: the cylindrical layer, the cylindrical tube and the radiated sound field in front of the panel. By coupling the one-dimensional analytical models of the different parts, the radiated sound can be calculated. The influence of the bend is not taken into account here.

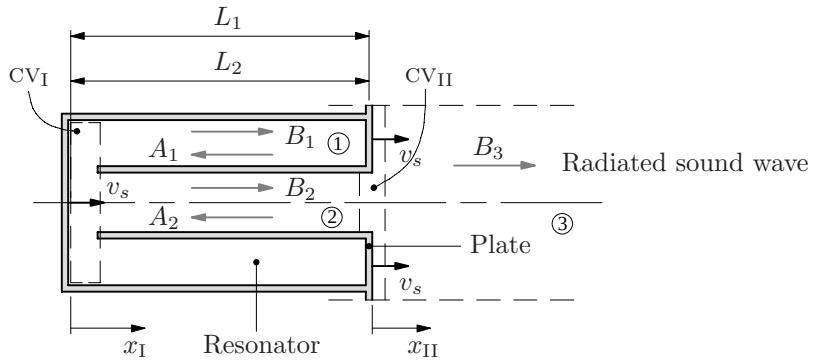


**Figure C.1**: Model of sound radiation by a rigid characteristic area with a tube-in-tube resonator.

The pressure $p_1$ and the axial velocity $v_1$ inside the cylindrical layer are described by equation (A.28) and equations (A.29) and (A.40), averaged over the cross-section, respectively. Inside the cylindrical tube, the pressure $p_2$ and the axial velocity $v_2$ are described by equations (2.21) and (2.26). For the pressure $p_3$ and the axial velocity $v_3$ of the radiated sound field, the standard acoustic solutions are used. The sound fields in both resonator parts are defined with respect to the axial coordinate $x_{\mathrm{I}}$ and the radiated sound field is defined with reference to coordinate $x_{\mathrm{II}}$ (see Figure C.1). The unknown pressure amplitudes $A_1$, $B_1$, $A_2$, $B_2$, and $B_3$ are determined by the boundary conditions of the system. Since the sound is radiated to the far field, no reflection is assumed to take place and the pressure amplitude $A_3$ equals zero.

Assuming that the plate and the resonator vibrate harmonically with the same normal velocity $v_s$, five boundary conditions can be formulated. The first boundary condition states that the fluid velocity at the end of the cylindrical layer is equal to the velocity of the structure. At the transition of the cylindrical layer to the cylindrical tube, the pressure is assumed to be continuous. Moreover, conservation of mass is applied for the control volume CV$_{\mathrm{I}}$, indicated by the dashed lines in Figure C.1. Also, at the entrance of the res-

onator, the pressure is assumed to be continuous and conservation of mass is applied for the control volume $\mathrm{CV_{II}}$. All together, these boundary conditions can be written as:

$$v_1|_{x_\mathrm{I}=L_1} = v_s \tag{C.1}$$

$$p_1|_{x_\mathrm{I}=0} = p_2|_{x_\mathrm{I}=0} \tag{C.2}$$

$$v_1|_{x_\mathrm{I}=0}\, S_1 + v_2|_{x_\mathrm{I}=0}\, S_2 = v_s\,(S_1 + S_2) \tag{C.3}$$

$$p_2|_{x_\mathrm{I}=L_2} = p_3|_{x_\mathrm{II}=0} \tag{C.4}$$

$$v_2|_{x_\mathrm{I}=L_2}\, S_2 + v_s\,(S - S_2) = v_3|_{x_\mathrm{II}=0}\, S \tag{C.5}$$

where $L_1$, $L_2$, $S_1$ and $S_2$ are the effective lengths and the cross-sectional areas of the cylindrical layer and the cylindrical tube, respectively, and $S$ is the characteristic area. By applying the boundary conditions to equations (A.28), (A.29), (2.21) and (2.26), the unknown pressure amplitudes $A_1$, $B_1$, $A_2$, $B_2$ and $B_3$ can be solved for a given structural velocity $v_s$. Subsequently, the radiated sound power can be determined with equations (2.50) and (2.51).

### Bent resonator

Figure C.2 shows the model of a characteristic area of a panel with bent resonators. The model consists of three parts: two cylindrical tubes and the radiated sound field in front of the panel. By coupling the one-dimensional analytical models of the different parts, the radiated sound can be calculated. The sound fields in both tubes are defined with respect to the axial coordinate $x_\mathrm{I}$ and the radiated sound field is defined with reference to coordinate $x_\mathrm{II}$ (see Figure C.2). Again, the influence of the bends is not taken into account here.

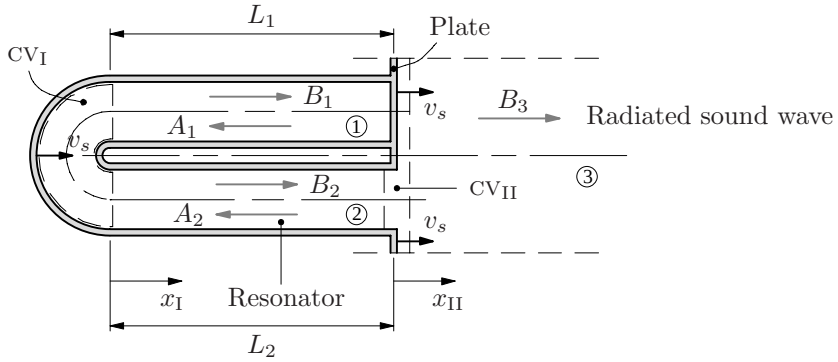


**Figure C.2**: Model of sound radiation by a rigid characteristic area with a bent tube resonator.

The only difference between the present model and the model of a characteristic area of a panel with tube-in-tube resonators is the sound field in the tube indicated by ①. The pressure $p_1$ and the axial velocity $v_1$ are now described by equations (2.21) and (2.26). The unknown pressure amplitudes $A_1$, $B_1$, $A_2$, $B_2$ and $B_3$ are solved by applying the same set of boundary conditions as for the tube-in-tube resonator.

## C.2 Experimental validation

The model for sound radiation by a characteristic area with a tube-in-tube resonator, as presented in the previous section, was validated by means of experiments in an impedance tube. Both the procedure and the model of the experimental setup that were used are the same as described in Section 2.5. Figure C.3 shows the two samples with folded resonators that were tested. The dimensions of the resonators, as well as the distances from the fronts of the samples to the end of the impedance tube, are listed in Table C.1. $R_i$ and $R_o$ are the inner and outer radius of the cylindrical layer, respectively, and $R$ is the radius of the tube part of the resonator. The effective length $L_2$ of the tube part of the resonator is determined by adding an end correction $\delta$, calculated with equation (2.61), to the physical length $L_{\text{phy}2}$. For both samples, the length of the transition between the tube part of the resonator and the cylindrical layer is 5 mm.

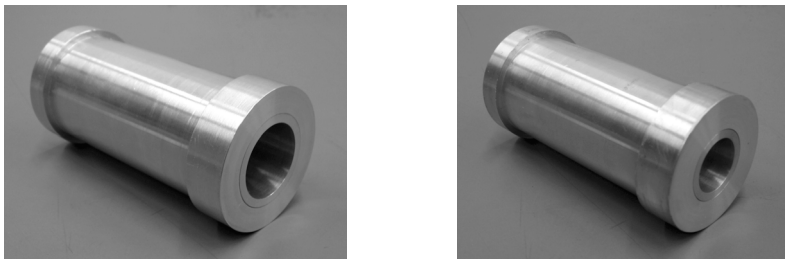

(a) Sample 1. (b) Sample 2.

**Figure C.3**: Photos of the samples for experimental validation.

Figures C.4 and C.5 show the results of the measurements on the two samples, compared with the analytical results. It can be seen that there is an excellent agreement between model and measurement.

| | $L_{\text{phy1}}$ [m] | $R_o$ [m] | $R_i$ [m] | $L_{\text{phy2}}$ [m] | $R$ [m] | $\Omega$ [-] | $L_{\text{imp}}$ [m] |
|---|---|---|---|---|---|---|---|
| Sample 1 | 0.0800 | 0.0190 | 0.0160 | 0.0900 | 0.013 | 0.27 | 0.620 |
| Sample 2 | 0.0800 | 0.0190 | 0.0130 | 0.0900 | 0.010 | 0.16 | 0.620 |

**Table C.1**: Dimensions of the samples and experimental setup for validation.

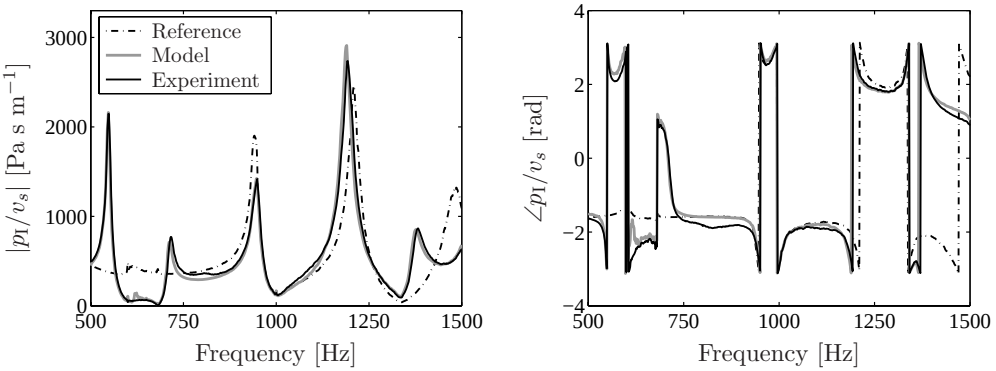


(a) Magnitude. (b) Phase.

**Figure C.4**: Magnitude and phase of calculated and measured transfer functions $p_{\text{I}}/v_s$ for sample 1.

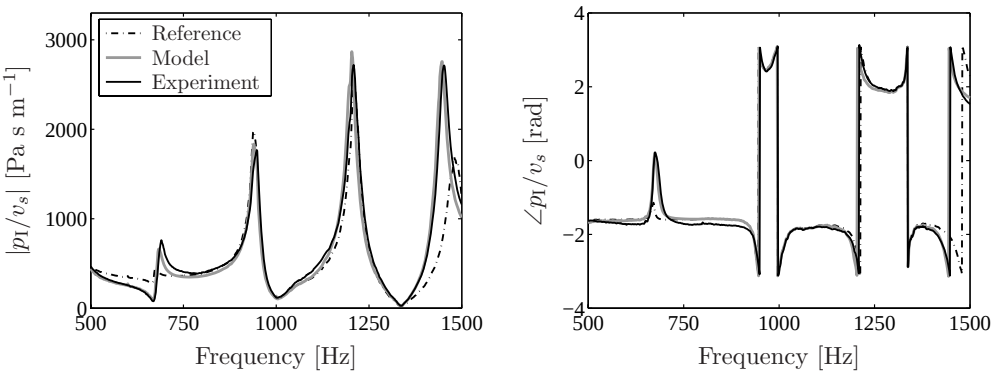


(a) Magnitude. (b) Phase.

**Figure C.5**: Magnitude and phase of calculated and measured transfer functions $p_{\text{I}}/v_s$ for sample 2.

# Appendix D

# Finite element formulation of interface element

In this appendix, the mass and stiffness matrices of the acoustic interface element are derived, which is presented in Section 4.3.2. The interface element describes both the acousto-elastic interaction and the acoustic behaviour of the resonators. The general purpose of the interface element is to relate the pressures in air to the structural displacements of the panel.

A schematic overview of the parameters that are used for the FEM formulation are shown in Figure 4.15. In Section 4.3.2, it was mentioned that for both sides of the panel the same interface elements can be used. In this appendix, therefore, only the interface element at the left-hand side of the panel is considered (see Figure 4.15).

Under the assumptions presented in Section 4.3.2, the distributed load of the air on the structure and the fluid acceleration can be written according to equations (4.34) and (4.35):

$$q_l = p_l[1 - \Omega_l + \Omega_l \sec(kL)] + \rho_0 c_0 u_s \omega \Omega_l \tan(kL) \tag{D.1}$$

$$\rho_0 c_0 a_l = \rho_0 c_0 a_s[1 - \Omega_l + \Omega_l \sec(kL)] - p_l \omega \Omega_l \tan(kL) \tag{D.2}$$

For discretisation, the pressures $p$ and the *normal* structural displacements $u_s$ are written in terms of vectors with nodal pressures $\mathbf{p}$ and nodal structural displacements $\mathbf{u}$, and vectors with interpolation functions $\mathbf{N}_f$ and $\mathbf{N}_s$:

$$p_l = (\mathbf{N}_f)^{\mathrm{T}} \mathbf{p}, \quad u_s = (\mathbf{N}_s)^{\mathrm{T}} \mathbf{u} \tag{D.3}$$

The element matrices for the acoustic part of the interface element are obtained by discretising the wave equation using the Galerkin method. Multiplying the

equation by a virtual pressure perturbation $\delta p$ and integrating over the volume of the domain yields the variation of a functional[1] [59]. The mass coupling matrices follow from the contribution $\delta\Pi_f$ of the pressure on the boundary of the domain to this variation:

$$\delta\Pi_f = \int_{\Gamma_{fs}} \rho_0 \, \delta p_l \, a_l \, \mathrm{d}\Gamma \tag{D.4}$$

where $a_l$ is the outward (out of the air domain) normal component of the fluid acceleration, and $\Gamma_{fs}$ is the interface area. Substitution of equations (D.2) and (D.3) into equation (D.4) gives for the characteristic area:

$$\delta\Pi_f = -\omega^2 [\delta\mathbf{p}]^{\mathrm{T}} \mathbf{M}_{fs}^{pu}(\omega)\, \mathbf{u} - \omega^2 [\delta\mathbf{p}]^{\mathrm{T}} \mathbf{M}_{fs}^{pp}(\omega)\, \mathbf{p} \tag{D.5}$$

with the mass coupling matrices formulated as:

$$\mathbf{M}_{fs}^{pu}(\omega) = \int_{\Gamma_{fs}} \rho_0 \left[1 - \Omega + \Omega \sec(kL)\right] \mathbf{N}_f \left[\mathbf{N}_s\right]^{\mathrm{T}} \mathrm{d}\Gamma \tag{D.6}$$

$$\mathbf{M}_{fs}^{pp}(\omega) = \int_{\Gamma_{fs}} \frac{\Omega \tan(kL)}{\omega c_0} \mathbf{N}_f \left[\mathbf{N}_f\right]^{\mathrm{T}} \mathrm{d}\Gamma \tag{D.7}$$

The stiffness coupling matrices follow similarly from the formulation of the structural part of the standard acousto-elastic interaction problem. By using equations (D.1) and (D.3), the contribution $\delta\Pi_s$ of the pressure on the interface to the variation of the functional can be written as:

$$\delta\Pi_s = -\int_{\Gamma_{fs}} \delta u_s q_l \, \mathrm{d}\Gamma = -\omega^2 [\delta\mathbf{u}]^{\mathrm{T}} \mathbf{K}_{fs}^{up}(\omega)\, \mathbf{p} - \omega^2 [\delta\mathbf{u}]^{\mathrm{T}} \mathbf{K}_{fs}^{uu}(\omega)\, \mathbf{u} \tag{D.8}$$

with the stiffness coupling matrices formulated as:

$$\mathbf{K}_{fs}^{up}(\omega) = -\int_{\Gamma_{fs}} \left[1 - \Omega + \Omega \sec(kL)\right] \mathbf{N}_s \left[\mathbf{N}_f\right]^{\mathrm{T}} \mathrm{d}\Gamma \tag{D.9}$$

$$\mathbf{K}_{fs}^{uu}(\omega) = -\int_{\Gamma_{fs}} \rho_0 c_0 \omega \Omega \tan(kL)\, \mathbf{N}_s \left[\mathbf{N}_s\right]^{\mathrm{T}} \mathrm{d}\Gamma \tag{D.10}$$

In this case, the different contributions to the interface element are divided into a mass part and a stiffness part. However, other divisions are also possible.

[1] A functional is an integral expression that implicitly contains the governing differential equations for a particular problem. Such an integral expression is also called the weak form [13].

# Appendix E

# Data of experimental setup

In Chapter 5, sound transmission loss measurements are described that were performed on two panels with resonators. In this appendix, some data are presented of the experimental setup that was used for this. In Section E.1, an overview is given of the measurement equipment with which the experiments were performed. In Section E.2, the dimensions are given of the reverberation room and the niche, as well as of the wooden frames for the suspension. Finally, in Section E.3, a drawing is shown of the aluminium tubes that were used to construct the panel with tubes (see Section 5.2.4).

## E.1 Measurement equipment

Table E.1 shows an overview of the measurement equipment that was used for the sound transmission loss measurements as presented in Chapter 5.

| Description | Type | Remarks |
|---|---|---|
| Signal generator | B&K 1405 | White noise 20 kHz |
| Band pass filters | LMS-DIFA-SCADAS II | Between signal generator and Daub amplifiers |
| Power amplifiers | Daub 500B | For Altec drivers |
| Band pass filters | Monocor DNB1255 | Between Daub amplifiers and Altec drivers |
| High frequency sound sources | Altec 290K (3×), 290L (1×) | Speakers in the corners |
| Band pass filter | LMS-DIFA-SCADAS II | Between signal generator and B&K amplifier |
| Power amplifier | B&K 2716 | For low frequency sound source |
| Low frequency sound source | B&K 4296 | |
| Rotating booms (2×) | B&K 3923 | |
| Microphone 1/2″, pre-amplifier | Linear X, type M51 | In reverberation room |
| Sound intensity probe | B&K 3519 | |
| Microphones 1/2″ | B&K 4181 | |
| Microphone pre-amplifier | B&K 2633 | |
| Scanning robot and controller | CRS-plus, type A460 | |
| Front-end plus data storage | GBM, Viper | |
| Personal computer | | |

**Table E.1**: Measurement equipment for sound transmission loss measurements.

## E.2 Dimensions of the experimental setup

A schematic representation of the experimental setup is shown in Figure 5.2. The reverberation room and the niche are also depicted in Figure E.1. Tables E.2 and E.3 show the coordinates of the corner points of these two units. The coordinates of the possible positions of the low frequency sound source are listed in Table E.4 (see also Figure 5.2).

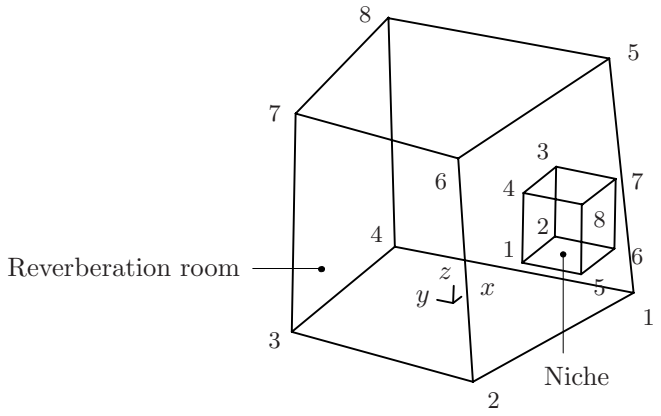


**Figure E.1**: Reverberation room with niche.

| Point | $x$ [m] | $y$ [m] | $z$ [m] |
|---|---|---|---|
| 1 | 1.417 | -1.966 | 0 |
| 2 | -2.320 | -1.395 | 0 |
| 3 | -1.892 | 1.465 | 0 |
| 4 | 1.370 | 1.515 | 0 |
| 5 | 1.162 | -1.675 | 3.405 |
| 6 | -2.280 | -1.110 | 3.135 |
| 7 | -1.892 | 1.465 | 3.135 |
| 8 | 1.060 | 1.515 | 3.405 |

**Table E.2**: Coordinates of the corner points of the reverberation room.

| Point | $x$ [m] | $y$ [m] | $z$ [m] |
|---|---|---|---|
| 1 | -0.500 | -1.230 | 1.005 |
| 2 | 0.500 | -1.230 | 1.005 |
| 3 | 0.500 | -1.230 | 2.005 |
| 4 | -0.500 | -1.230 | 2.005 |
| 5 | -0.500 | -2.090 | 1.005 |
| 6 | 0.500 | -2.103 | 1.005 |
| 7 | 0.500 | -2.110 | 2.005 |
| 8 | -0.500 | -2.093 | 2.005 |

**Table E.3**: Coordinates of the corner points of the niche.

| Position | $x$ [m] | $y$ [m] | $z$ [m] |
|---|---|---|---|
| 1 | 1.00 | 1.20 | 2.00 |
| 2 | -1.90 | -0.50 | 1.25 |
| 3 | 0.50 | 1.10 | 0.27 |

**Table E.4**: Possible positions of low frequency sound source.

Figure E.2 shows the dimensions of the square wooden frames with rubber strings for the suspension of the panels.

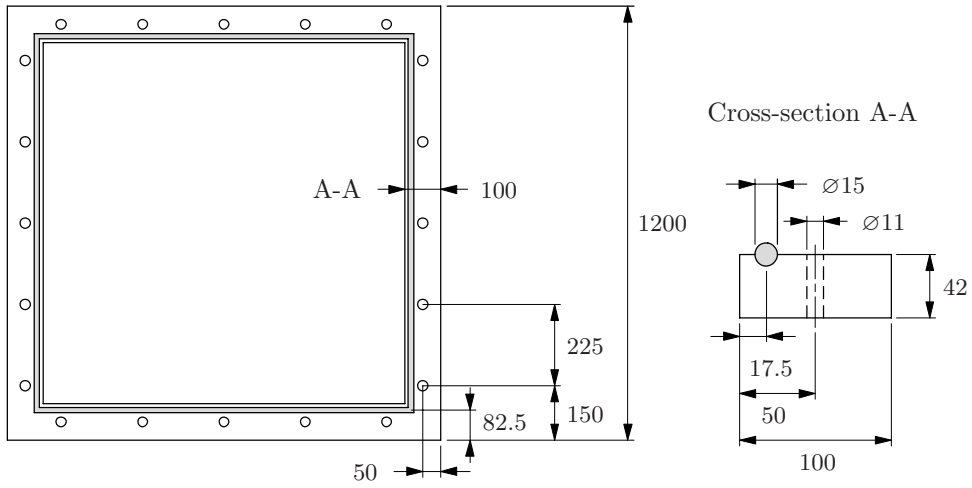


**Figure E.2**: Dimensions of square wooden frame with rubber string for mounting the panel [mm].

## E.3 Tube dimensions

Figure E.3 shows the dimensions of the aluminium tubes that were used to construct the panel with tubes (see Section 5.2.4).

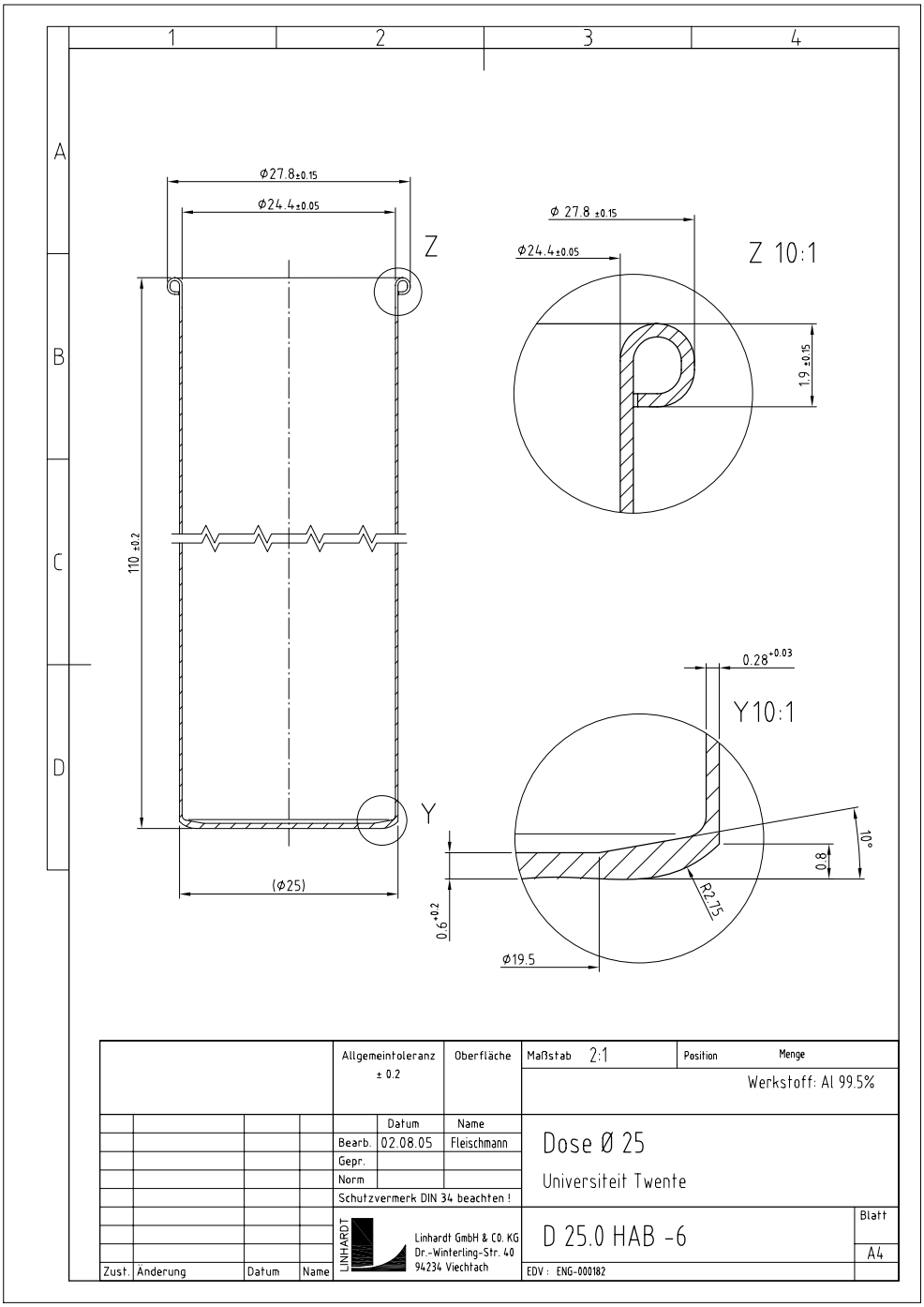


**Figure E.3**: Dimensions of aluminium tubes.

# Bibliography


[1] T.G.H. Basten. *Noise reduction by viscothermal acousto-elastic interaction in double wall panels*. PhD thesis, University of Twente, The Netherlands, 2001.

[2] W.M. Beltman. *Viscothermal wave propagation including acousto-elastic interaction*. PhD thesis, University of Twente, The Netherlands, 1998.

[3] L.L. Beranek and I.L. Vér. *Noise and vibration control engineering; principles and applications*. John Wiley & Sons, Inc., 1992.

[4] W.V. Bhat and J.F. Wilby. Interior noise radiated by an airplane fuselage subjected to turbulent boundary layer excitation and evaluation of noise reduction treatments. *Journal of Sound and Vibration*, 18(4):449–464, 1971.

[5] M.C. Bhattacharya, R.W. Guy, and M.J. Crocker. Coincidence effect with sound waves in a finite plate. *Journal of Sound and Vibration*, 18(2):157–169, 1971.

[6] D.A. Bies and C.H. Hansen. *Engineering noise control; theory and practise*. E&FN SPON, 1996.

[7] D.T. Blackstock. *Fundamentals of physical acoustics*. John Wiley & Sons, Inc., 2000.

[8] R.H. Bolt, S. Labate, and U. Ingård. The acoustic reactance of small circular orifices. *Journal of the Acoustical Society of America*, 21(2):94–97, 1949.

[9] Brüel & Kjær, 2850 Nærum, Denmark. *Sound intensity*, 1993.

[10] J.Y. Chung. Cross-spectral method of measuring acoustic intensity without error caused by instrument phase mismatch. *Journal of the Acoustical Society of America*, 64(6):1613–1616, 1978.

[11] J.Y. Chung and D.A. Blaser. Transfer function method of measuring in-duct acoustic properties. I. Theory. *Journal of the Acoustical Society of America*, 68(3):907–913, 1980.

[12] J.Y. Chung and D.A. Blaser. Transfer function method of measuring in-duct acoustic properties. II. Experiment. *Journal of the Acoustical Society of America*, 68(3):914–921, 1980.

[13] R.D. Cook, D.S. Malkus, M.E. Plesha, and R.J. Witt. *Concepts and applications of finite element analysis*. John Wiley & Sons, Inc., 4th edition, 2002.

[14] A. Cops and M. Minten. Comparative study between the sound intensity method and the conventional two-room method to calculate the sound transmission loss of wall constructions. *Noise Control Engineering Journal*, 22(3):104–111, 1984.

[15] T.J. Cox and P. D'Antonio. *Acoustic absorbers and diffusers; theory, design and application*. Spon Press, 2004.

[16] R.R. Craig Jr. and M.C.C. Bampton. Coupling of substructures for dynamic analysis. *AIAA Journal*, 6(7):1313–1319, 1968.

[17] V. Easwaran, V.H. Gupta, and M.L. Munjal. Relationship between the impedance matrix and the transfer matrix with specific reference to symmetrical, reciprocal and conservative systems. *Journal of Sound and Vibration*, 161(3):515–525, 1993.

[18] F.J.M. van der Eerden. *Noise reduction with coupled prismatic tubes*. PhD thesis, University of Twente, The Netherlands, 2000.

[19] F.J. Fahy. Measurement of acoustic intensity using the cross-spectral density of two microphone signals. *Journal of the Acoustical Society of America*, 62(4):1057–1059, 1977.

[20] F.J. Fahy. *Sound and structural vibration*. Academic Press, 1985.

[21] F.J. Fahy. *Sound intensity*. E & FN SPON, 1995.

[22] F.J. Fahy. *Foundations of engineering acoustics*. Academic Press, 2001.

[23] C.D. Field and F.R. Fricke. Theory and application of quarter-wave resonators: a prelude to their use for attenuating noise entering buildings through ventilation openings. *Applied Acoustics*, 53(1-3):117–132, 1998.

[24] W.R. Graham. Boundary layer induced noise in aircraft, part I: the flat plate model. *Journal of Sound and Vibration*, 192(1):101–120, 1996.

[25] R.J. Guyan. Reduction of stiffness and mass matrices. *AIAA Journal*, 3(2):380, 1965.

[26] R.E. Halliwell and A.C.C. Warnock. Sound transmission loss: comparison of conventional techniques with sound intensity techniques. *Journal of the Acoustical Society of America*, 77(6):2094–2103, 1985.

[27] M.H.C. Hannink. Improvement of the sound transmission loss of panels by means of acoustically tuned resonators. In *Proceedings of ICAS*, Hamburg, Germany, 2006.

[28] M.H.C. Hannink, R.M.E.J. Spiering, Y.H. Wijnant, and A. de Boer. A finite element approach to the prediction of sound transmission through panels with acoustic resonators. In *Proceedings of ICSV13*, Vienna, Austria, 2006.

[29] M.H.C. Hannink and H. van der Wal. Design and testing of a 1 m × 1 m optimised trim panel. Technical Report FACE/TWE/5.1/TR-0003, Univeristy of Twente, The Netherlands, 2005.

[30] M.H.C. Hannink, J.P. Vlasma, Y.H. Wijnant, and A. de Boer. Application of acoustically tuned resonators for the improvement of sound insulation in aircraft. In *Proceedings of Internoise*, Rio de Janeiro, Brazil, 2005.

[31] M.H.C. Hannink, Y.H. Wijnant, and A. de Boer. Optimised sound absorbing trim panels for the reduction of aircraft cabin noise. In *Proceedings of ICSV11*, pages 1855–1862, St. Petersburg, Russia, 2004.

[32] H.H. Hubbard. *Aeroacoustics of flight vehicles; theory and practise*, volume 2. Acoustical Society of America, 1995.

[33] F. Jacobsen. A note on finite difference estimation of acoustic particle velocity. *Journal of Sound and Vibration*, 256(5):849–859, 2002.

[34] L.E. Kinsler, A.R. Frey, A.B. Coppens, and J.V. Sanders. *Fundamentals of acoustics*. John Wiley & Sons, 1982.

[35] M.J. Kippers. Compact resonators; on the design of folded acoustic resonators applied in thin vibrating panels to reduce radiated noise. Master's thesis, University of Twente, The Netherlands, 2005.

[36] F.P. Mechel. Sound fields at periodic absorbers. *Journal of Sound and Vibration*, 136(3):379–412, 1990.

[37] F.P. Mechel. *Schallabsorber*, volume II. S. Hirzel Verlag, 1995.

[38] K. Naghshineh and V.B. Mason. Reduction of sound radiated from vibrating structures via active control of local volume velocity. *Applied Acoustics*, 47:27–46, 1996.

[39] A.D. Pierce. *Acoustics; an introduction to its physical principles and applications*. Acoustical Society of America, 1994.

[40] K. Renji, P.S. Nair, and S. Narayanan. Critical and coincidence frequencies of flat plates. *Journal of Sound and Vibration*, 205(1):19–32, 1997.

[41] J.H. Rindel. Sound transmission through single layer walls. In *Proceedings of Noise-93*, St. Petersburg, Russia, 1993.

[42] H.-S. Roh, W.P. Arnott, J.M. Sabatier, and R. Raspet. Measurement and calculation of acoustic propagation constants in arrays of small air-filled rectangular tubes. *Journal of the Acoustical Society of America*, 89(6):2617–2624, 1991.

[43] B.W. Ross and R.A. Burdisso. Low frequency passive noise control of a piston structure with a weak radiating cell. *Journal of the Acoustical Society of America*, 106(1):226–232, 1999.

[44] Y. Saad and M.H. Schultz. GMRES: a generalized minimal residual algorithm for solving nonsymmetric linear systems. *SIAM Journal on Scientific and Statistical Computing*, 7(3):856–869, 1986.

[45] J.C. Snowdon. Mechanical four-pole parameters and their application. *Journal of Sound and Vibration*, 15(3):307–323, 1971.

[46] B.H. Song and J.S. Bolton. A transfer-matrix approach for estimating the characteristic impedance and wave numbers of limp and rigid porous materials. *Journal of the Acoustical Society of America*, 107(3):1131–1152, 2000.

[47] G.H. Koopmann St. Pierre Jr., R.L. and W. Chen. Volume velocity control of sound transmission through composite panels. *Journal of Sound and Vibration*, 210(4):441–460, 1998.

[48] M.R. Stinson. The propagation of plane sound waves in narrow and wide circular tubes, and generalization to uniform tubes of arbitrary cross-sectional shape. *Journal of the Acoustical Society of America*, 89(2):550–558, 1991.

[49] M.R. Stinson and Y. Champoux. Propagation of sound and the assignment of shape factors in model porous materials having simple pore geometries. *Journal of the Acoustical Society of America*, 91(2):685–695, 1992.

[50] H. Tijdeman. On the propagation of sound waves in cylindrical tubes. *Journal of Sound and Vibration*, 39(1):1–33, 1975.

[51] J.P. Vlasma. Noiseless vibrating surfaces; on the reduction of noise, generated by vibrating structures by means of acoustic resonators. Master's thesis, University of Twente, The Netherlands, 2004.

[52] H. van der Wal and E. Geurts. Transmission loss measurements and modal testing on 2m x 1.6m curved panels; test set-up and experimental results. Technical Report FACE/NLR/6.1/TR-0016, NLR, The Netherlands, 2004.

[53] H.M.M. van der Wal and A.C. Nilsson. Sound-transmission measurements on composite and metal fuselage panels for different boundary conditions. In *Proceedings of 11th AIAA/CEAS Aeroacoustics Conference*, Monterey, California, USA, 2005.

[54] Y.H Wijnant, M.H.C. Hannink, and A. de Boer. Application of viscothermal wave propagation theory for reduction of boundary layer induced noise. In *Proceedings of Euronoise*, Naples, Italy, 2003.

[55] Y.H Wijnant, M.H.C. Hannink, and J.P. Vlasma. Broadband sound reduction with acoustic resonators. Patent, International Publication Number: WO 2006/118443 A1, Applicant: University of Twente, 2006.

[56] J.F. Wilby. Aircraft interior noise. *Journal of Sound and Vibration*, 190(3):545–564, 1996.

[57] J.W. Wind, Y.H. Wijnant, and A. de Boer. Fast evaluation of the Rayleigh integral and applications to inverse acoustics. In *Proceedings of ICSV13*, Vienna, Austria, 2006.

[58] T. ten Wolde. On the validity and application of reciprocity in acoustical, mechano-acoustical and other dynamical systems. *Acustica*, 28:23–32, 1973.

[59] O.C. Zienkiewicz and R.L. Taylor. *The finite element method, volume 1: the basis*. Butterworth-Heinemann, $5^{\text{th}}$ edition, 2000.

[60] C. Zwikker and C. Kosten. *Sound absorbing materials*. Elsevier, 1949.

# Nawoord

Het zit erop. Iets meer dan vier jaar voorbij gevlogen. De tijd vliegt; als het leuk is zelfs wat sneller. De afgelopen jaren heb ik het voorrecht gehad heel wat bijzondere mensen te leren kennen. En zonder veel van deze mensen zou dit boekje er waarschijnlijk nooit zijn geweest. Natuurlijk zijn deze paar regels dan ook veel te kort om iedereen daarvoor genoeg te bedanken, maar ik zal een kleine poging wagen.

Allereerst wil ik André de Boer graag bedanken; niet alleen voor het feit dat hij me heeft weten te overtuigen nog een paar jaartjes langer in het mooie Twente te blijven, maar ook zeker voor zijn steun en vertrouwen, en zijn altijd pragmatische kijk op de zaak. Daarnaast wil ik Ysbrand Wijnant en Ruud Spiering graag bedanken voor hun bijzonder enthousiaste begeleiding (Ruud zelfs tijdens zijn pensioen!) en de geweldige bijdrage die zij hebben geleverd aan dit onderzoek. Verder wil ik Bert Wolbert bedanken voor alle hulp bij het experimentele deel van dit werk. Ook dynamica-mannen Peter van der Hoogt en Henk Tijdeman bedankt voor de prettige samenwerking.

Debbie Vrieze, meer dan een geweldige secretaresse. Naast alle administratieve steun, heb ik ook mogen genieten van een hoop morele en culinaire support. Debbie, hartstikke bedankt voor alle goede zorgen! Ook Tanja van Scherpenzeel hartelijk dank voor alle hulp en interesse.

Overige (ex-)collega's van dynamica: Marco Oude Nijhuis, René Visser, Clemens Beijers, Rob Huls, Ekke Oosterhuis, Marten Nijhof, Peter Sloetjes, Jelmer Wind, Ronald Kampinga, Didem Akçay Perdahcıoğlu en Emre Dikmen, het was erg goed toeven met jullie. Niet alleen bedankt voor jullie inhoudelijke bijdrage, maar ook voor de fantastische sfeer in de groep en de gezellige tijd buiten het werk. Een grote bijdrage aan dat laatste hebben ook zeker de collega's van de DiekA-groep geleverd: Marianna Avetisyan, Martijn Bonte, Igor Burchitz, Bert Koopman, Paweł Owczarek, Loes van Haaren, Semih Perdahcıoğlu en Maarten van Riel. Allemaal geweldig bedankt voor de gezelligheid tijdens alle bioscoopbezoeken, barbecues, feestjes, etentjes, hardloop-, schaats- en basketbaltrainingen, buisjes-lijmsessies, lijm-

uit-honingraatstructuur-verwijdersessies en alle andere sociale activiteiten. Ik heb me erg goed vermaakt.

Verder natuurlijk ook alle andere collega's van de vakgroep Technische Mechanica bedankt voor het prima sociale klimaat tijdens de koffiepauzes en daarbuiten.

Hardloop-die-hards Jaap van Kampen, Richard Loendersloot en Genie Stoffels, jullie waren uitstekende hazen. Vooral de theekransjes en etentjes na het hardlopen werkten erg motiverend.

Dan nog even terug naar de inhoud. Herbert Boender, Jacob Vlasma, Mathijs Kippers, Maarten van Balveren en Rob Talma wil ik graag bedanken voor de waardevolle bijdrage die zij met hun afstudeerwerk hebben geleverd aan dit onderzoek. Ik vond het erg leuk met jullie samengewerkt te hebben.

Ook de samenwerking binnen het FACE-project heb ik als bijzonder positief ervaren. In het bijzonder wil ik graag Henk van der Wal van het NLR bedanken. Samen met Marko Beenders, Corné Boons en Onno Stallinga zijn de metingen mogelijk gemaakt die worden beschreven in Chapter 5 van dit proefschrift. Allen hartelijk dank hiervoor.

Tenslotte zijn er natuurlijk ook nog een heleboel mensen buiten de UT die, hoewel misschien wat minder direct, toch ook zeker een grote bijdrage hebben geleverd aan de goede afloop van dit avontuur. In particolare vorrei ringraziare Maurizio Meneguzzo e Renata Albano; molte grazie di tutto. Ci vediamo presto. En "last but not least" wil ik natuurlijk graag mijn ouders en Leontien bedanken. Bedankt voor alles, dat jullie er altijd zijn!

Iedereen super bedankt!

Marieke Hannink

Enschede, mei 2007